10-25-2017

Compact and Robust Ultrasound-guided Diffuse Optical Tomography for Breast Imaging: System and Algorithm Developments

Hamed Vavadi
University of Connecticut - Storrs, hamed.vavadi@uconn.edu

Compact and Robust Ultrasound-guided Diffuse Optical Tomography for Breast Imaging: System and Algorithm Developments

Hamed Vavadi, PhD

University of Connecticut, 2017

According to the World Health Organization, breast cancer is the most common cancer among women worldwide, claiming lives of hundreds of thousands of women each year. Mammography, ultrasound (US) and magnetic resonance imaging (MRI) are widely used to detect and diagnose breast lesions and each of them have some disadvantages which motivates researchers to find a new and high sensitive imaging method. Diffuse optical tomography (DOT) is a noninvasive functional imaging modality that utilizes near-infrared (NIR) light to probe tissue optical properties. Minimal light absorption in the NIR spectrum allows for several centimeters of light penetration in soft tissue. NIR is sensitive to hemoglobin which is directly related to tumor angiogenesis. If multiple wavelengths are used, it can probe tumor oxygen saturation. However, DOT has drawbacks on location uncertainty and low light quantification accuracy due to tissue scattering of NIR light. Ultrasound (US)-guided Diffuse Optical Tomography has overcome these problems.

The overall objective of my research is to move US-guided DOT one step closer from a research imaging modality to a commercial prototype for future wide use in clinics. To achieve this goal, I have overcome several challenges in both imaging hardware and software. In this Dissertation, I will discuss the progress we have made on development of two generations of US-guided DOT systems along with the software improvements. The developed systems have been improved in terms of robustness, stability, clinical safety and standards and user friendliness. In terms of software and algorithm development, automated methods for data selection, outlier removal and reference and perturbation filtering are presented. These methods have improved the robustness of the technique and increased speed of image formation by eliminating the need for an expert to perform data preprocessing and data selection. Phantom and clinical experimental results will be demonstrated to evaluate the performance of the developed systems and algorithms.

Compact and Robust Ultrasound-guided Diffuse Optical Tomography for Breast Imaging: System and Algorithm Developments

Hamed Vavadi

B.S., University of Mazandaran, 2007

M.S., Iran University of Science and Technology, 2011

A Dissertation

Submitted in Partial Fulfillment of the

Requirements for the Degree of

Doctor of Philosophy

at the

University of Connecticut

2017

APPROVAL PAGE

Doctor of Philosophy Dissertation

Compact and Robust Ultrasound-guided Diffuse Optical Tomography for Breast Imaging: System and Algorithm Developments

Presented by

Hamed Vavadi, B.S., M.S.

Major Advisor _____

Quing Zhu

Major Co Advisor _____

Rajeev Bansal

Associate Advisor _____

Patrick Kumavor

Associate Advisor _____

Monty A. Escabi

Associate Advisor _____

Guoan Zheng

University of Connecticut
2017

Dedication

This Dissertation is dedicated to my loving and supportive wife Fateme, my mom, Fatemeh, and my dad Ali for their unconditional love and supports.

I spend most of the past four years in labs to do research and write this dissertation and I would never have been able to write these words without my family's love and support. Above all, I would like to thank my brilliant and outrageously loving and supportive wife, Fateme for her outstanding support and great patience during these years. We had a wonderful journey while we were both working toward our PhDs at the same time and without her outstanding support and understanding I was never able to write this dissertation. I would like to thank my parents who gave me their unconditional love and support during every step of my life and raised me to the person I am today. I want to also thank my siblings, Mehdi, Mohammad, and Ahmad for their support and understanding. I was lucky to grow up with them and I would like to thank them for their love and support.

Acknowledgement

My deepest gratitude goes to my advisor, Professor Quing Zhu for her excellent guidance, support and patience. I learned a lot from her and the words are not enough to express my gratitude toward her. Her enthusiasm about helping patients was an infinite source of motivation for me. Whenever I had an idea for research and development, the first question she was asking was about the benefit of the idea for patients in need. Her exceptional enthusiasm motivated me to work as hard as possible during the last four years and gave me the feeling of joy and satisfaction about the outcome of my research.

My appreciation extends to my Co-Major advisor, Professor Rajeev Bansal, whose mentoring, guidance, and support during the last four years were extremely valuable. Despite his busy schedule as the department head, he was always available and helpful with the best possible advises for me.

Also, I want to thank my committee members, Professor Monty Escabi, Professor Guoan, Zheng and Professor Patrick Kumavor, who their wise comments helped improved this dissertation.

I must acknowledge my friends and colleagues in Ultrasound and Optical Imaging Laboratory who provided me such a great atmosphere to do my research and many of them helped me directly and indirectly in multiple studies. I was lucky to work along such a brilliant group of colleagues, and I want to specifically thank Dr. Chen Xu and Atahar Mostafa which were most involved with me on development of the imaging systems.

Contents

Contents vi

List of figures xi

List of Tables xvi

1. Introduction to Breast Imaging 1

1.1. Introduction 2

1.2. History of Medical Imaging 4

1.3. Breast Cancer 6

1.4. Breast Cancer Diagnosis and Treatment Monitoring 8

References 10

2. Ultrasound-guided Diffuse Optical Tomography 11

2.1. Diffuse Optical Tomography 12

2.2. Ultrasound-guided DOT 14

2.3. DOT for Neoadjuvant Chemotherapy 16

References 18

3. Development of Third-gen US-guided DOT System 20

3.1. Abstract 21

3.2. Introduction 22

3.3. Previous Systems 24

3.4. Third-Gen of NIR-DOT system 26

3.5. Clinical Results 34

3.6. Summary 38

References 40

4. Development of Fourth-gen US-guided DOT system 42

4.1. Abstract 43

4.2. Introduction 44

4.3. Method 47

4.3.1. System Structure 47

4.3.2. Hardware Miniaturization 49

4.3.3. Light Delivery and Probe Design 52

4.3.4. Software Improvement 53

4.4. Phantom Experiments 54

4.5. Finite element calibration 60

4.6. Summary 65

References 67

5. Reference Smoothing 69

5.1. Abstract 70

5.2. Introduction 71

5.3. Method and Model 73

5.4. Results 77

5.5. Discussion 84

References 85

6. Automated Data Pre-Processing 87

6.1. Abstract 88

6.2. Introduction 89

6.3. Dataset and System 92

6.3.1. Patients 92

6.3.2. System 93

6.4. Methods 93

6.4.1. Outlier Rejection in Reference Measurements 95

6.4.2. Saturation and Noise Data Rejection 97

6.4.3. Iterative Reweighted Least Square Fitting 98

6.4.4. Compounded Reference 99

6.4.5. Perturbation filtering 100

6.5. Results 103

6.6. Discussion and Summary 109

References 112

7. Summary and Future Works 115

.7.1 Summary 116

7.2. Future Works 119

References 121

List of figures

Figure 1.1. Normal breast tissue (ref. National cancer institute, [5,6]) 7

Figure.3.1. First generation of Ultrasound guided DOT system along with custom made 64 channels ultrasound system..... 25

Figure.3.2. Second generation of Ultrasound guided DOT system along with a commercial ultrasound system..... 26

Figure.3.3. Block diagram of data acquisition board..... 27

Figure 3.4. Final manufactured FPGA based data acquisition board 28

Figure 3.5. The layout of the optimized third gen DOT system 29

Figure 3.6. (a) The improved hybrid probe design; (b) Probe cover and probe. 30

Figure 3.7. Intralipid phantom experiment data from the improved NIR system. (a) log(r2*I(r)) vs. source-detector distance; (b) Phase vs. source-detector distance..... 31

Figure. 3.8. Block diagram of the third generation of the ultrasound guided DOT system. 32

Figure 3.9. The upgraded NIR system currently used at the UCONN Health Center. The commercial ultrasound transducer is readily plugged into the combined probe which houses all source and detector fibers for light delivery and collection. The co-registered ultrasound images are captured by a video capture card and are used to guide the light illumination and optical imaging reconstruction..... 33

Figure 3.10. Patient with an invasive mammary carcinoma located at 2 o'clock position of her left breast. Baseline or pre-treatment MRI image (a), ultrasound image (b) and total hemoglobin map (c). Total hemoglobin map revealed periphery distribution which is often seen in aggressive carcinomas. Post-treatment MRI image (d), ultrasound image (e), and total hemoglobin map (f). MRI indicated no residual tumor and total hemoglobin map showed no vascular contrast. The total hemoglobin map is obtained in 7 slices from left to right and top to bottom corresponding to depths of 0.5 cm to 3.5 cm from skin surface to chest wall. Each slide is given in x-y spatial dimensions of 9 x 9 cm. 36

Figure 3.12. Quantitative total hemoglobin level calculated from average maximum tHb levels with the average taken from several tHb images at the tumor site at each time point. 38

Figure 4.1. Block diagram of miniaturized diffuse optical tomography system 49

Figure 4.2. Thermal block laser diodes and it's cooling system for forth-Gen DOT 51

Figure 4.3. Combined diffuse optical tomography and ultrasound probe 53

Figure 4.4. Maximum reconstructed absorption for small high contrast phantom at depth of 2cm on different dates. The reconstructed values at 730,785, 808 and 830nm are presented. The green dashed line represents the actual absorption of the phantom. 56

Figure 4.5. (a) Glass ball (0.9 cm radius) filled with HbO2 solution and connected to holding fibers. (b) Sketch of the testing experimental setup 57

Figure 4.6. Oxygenated and deoxygenated hemoglobin spectrum; a) reconstructed absorption based on 4 wavelength data with the DOT system. b) measured with spectrometer. 58

..... 60

Figure 4.7. Oxygenated and deoxygenated hemoglobin calibrated with spectrometer and measured with DOT system..... 60

Figure 4.8. Finite element based cylindrical model of breast using COMSOL..... 61

Figure 4.9. Maximum reconstruction accuracy (%) for different phantoms before and after finite element calibration..... 65

Figure 5.1. Finite element based cylindrical model of breast using COMSOL..... 74

Figure 5.2. Real and imaginary part of normalized perturbation a) & b) homogeneous reference breast model, c) &d) heterogeneous reference breast model in second scenario, e) &f) heterogeneous reference breast model in third scenario. 78

Figure 5. 3. Effect of heterogeneity in the reference breast in the reconstructed image. a) Completely homogeneous reference, b) Low absorption heterogeneity inside the reference, c) High absorption heterogeneity inside the reference..... 79

Figure 5.4. Reconstructed image based on a) Completely homogeneous reference, b) Heterogeneous reference before correction, c) Heterogeneous reference after perturbation correction, d) Heterogeneous reference after reference smoothing. 80

Figure 5.5. Percentage of maximum reconstructed value with completely homogeneous reference (first column), heterogeneous reference (second column), heterogeneous reference after

perturbation correction (third column) and heterogeneous reference after reference smoothing (fourth column). 82

Figure 5.6. Reconstructed image of a malignant case before and after reference smoothing method. The left column represents the results of 740, 780, 808 and 830 nm before reference smoothing (a-d respectively) and right column represents the results of 740, 780, 808 and 830 nm after reference smoothing (e-h respectively) 83

Figure 6.1 Block diagram of the automated outlier removal and data selection method. In the block diagram MNR stands for maximum normed residual and IRLS stands for iterative reweighted least square. 94

Fig. 6.2. Log scaled amplitude and phase profiles of reference datasets before (first column) and after preprocessing (second column) as well as final compound reference (third column). Saturated source-detector pairs have been marked with red rectangle in the amplitude part of the first column. 100

Fig. 6.3. Reconstructed absorption maps of a benign breast lesion obtained at 740, 780, 808 and 830 nm with no preprocessing (1st row), with manual data selection (2nd row) and automated data selection (3rd row). Each slide is 9 cm by 9 cm reconstructed at the center depth of the lesion. Images from other depths were not shown. Vertical bars are absorption in cm^{-1} unit. 104

Fig. 6.4. Reconstructed absorption maps of a malignant breast lesion at 740, 780, 808 and 830 nm with no preprocessing (1st row), with manual data selection (2nd row) and automated data selection (3rd row). Each slide is 9 cm by 9 cm reconstructed at the center depth of the lesion. Images from other depths were not shown. Vertical bars are absorption in cm^{-1} unit. 105

Fig. 6.5. Ultrasound image (1st column) and total hemoglobin map calculated with no data selection (2nd column), with manual data selection (3rd column) and automatic data selection (4th column) of the benign (top row) and the malignant breast lesion (bottom row) reconstructed with automated data selection method. Each slide is 9 cm by 9 cm and vertical bars are hemoglobin concentrations in uM unit. 106

Fig. 6.6. Comparison of maximum total hemoglobin concentration reconstructed with both manual and automated data selection methods for 10 malignant and 10 benign cases. Vertical axis is the total hemoglobin concentration in μmol/Liter. 108

List of Tables

Table 4.1. Maximum reconstructed absorption map for high contrast and low contrast phantoms. 54

Table 4.2. Maximum reconstructed absorption map for high contrast and low contrast phantoms. 55

Table 4.4. Reconstructed oxygen saturation of 100% oxygenated oxyhemoglobin and 0% deoxygenated hemoglobin calculated with spectrometer as gold standard and DOT system for 5 different samples. 59

Table 4.5. Maximum reconstructed absorption for different lesions with absorption ranging from 0.08-0.24 cm-1 at different depths. 62

Table 4.6. Calculated calibration factor for different size and depth of the lesion 63

Table 7. maximum reconstructed absorption for different size of high contrast and low contrast phantoms at different depths after calibration with finite element model. 64

Table5.1. Maximum reconstructed absorption value with homogeneous, heterogeneous and heterogeneous after applying perturbation correction and reference smoothing methods 81

Table 6.1. Range of parameters used for analytical model and obtained maximum phase delay. 102

Table 6.2. Comparison of maximum reconstructed absorption coefficients of malignant and benign groups using manual and automated data selection method 107

Table 6.3. Comparison of maximum reconstructed absorption coefficients of malignant and benign groups using manual and automated data selection method 108

1. Introduction to Breast Imaging

1.1. Introduction

Medical imaging is a wide expanding field of development and research. Several methods and modalities for medical imaging have been developed during last century and they have found wide application in disease screening, diagnosis, and treatment monitoring. While each of the currently used conventional imaging has their strength and drawbacks, the urge to develop a new imaging technique, which could address current needs in medical application to improve human health, is

being felt more than ever. One of the promising ideas for next-generation medical imaging devices is optical imaging. While several methods of optical imaging with different wavelength sub-bands are currently under investigation, I am going to focus on the use of near infra-red light in optical imaging. The infrared light has several interesting characteristics such as good depth of penetration inside the tissue and sensitivity to hemoglobin. In this dissertation, I will specifically talk about near infra-red diffuse optical tomography method and the steps I took to move this modality one step closer to use widely in the clinical setting for breast cancer detection.

The dissertation is structured as below:

Chapter 1 gives a brief introduction to the background of the medical imaging and breast cancer.

Chapter 2 is discussing the principles of near infra-red diffuse optical tomography and its expansion to ultrasound-guided diffuse optical tomography.

Chapter 3 is focused on the development of the third generation of the ultrasound-guided diffuse optical tomography system and the results of clinical studies which have been done with that system.

Chapter 4 is along the path of chapter 3 and discuss the development of the fourth generation of Ultrasound-guided DOT system. In that chapter, we'll discuss the results of phantom experiments which have been done with this system.

In chapter 5 we'll study the effect of reference heterogeneity on the reconstructed DOT absorption map and introduce a smoothing method to reduce the effect of the reference heterogeneity in the reconstructed absorption map.

Chapter 6 is dedicated to the algorithm developments for improving the robustness of diffuse optical tomography technique for breast cancer detection. This algorithm specifically focuses on using multiple references and a perturbation filtering method to eliminate measurement outliers. This algorithm makes the process of data preprocessing automated by forming a robust reference measurement to eliminate the need for an expert user in data processing and improve the accuracy of US-guided DOT.

Finally, in chapter 7, we will summarize the first 6 chapters and make a conclusion about the progress we have made and provide ideas for the next step of system and algorithm development.

With this short introduction, we will continue to review the basic concepts which are going to be used in this Ph.D. Dissertation.

1.2. History of Medical Imaging

Wilhelm Röntgen, a physics professor discovered the x-rays in 1895 and it has been the start point of medical imaging. Different density of tissue results in different absorption of the X-ray passing through the tissue and results in a different number of x-ray photons reaching the film or camera detector on the other side of the tissue. This concept of utilizing different absorption of the X-Ray to map the density of the underlying tissue was a great breakthrough at the time and it

revolutionized the field of medical science and diagnosis [1]. Although the x-ray was a great breakthrough in the field of diagnostic sciences, scientists were not aware of the dangers of ionizing radiation of x-ray. Besides that, while x-ray has a great ability to differentiate soft tissue from the bones and hard objects, it lacked sensitivity to distinguish different soft tissues.

The second breakthrough in medical imaging happened in 1960's when the principles of ultrasonic beams have been utilized for medical imaging and the simple 2D ultrasound imaging devices were developed. Since then, this technology was expanded and several devices with multiple applications including, Sonographer, Echocardiography, Doppler blood flow measurements, and focused ultrasound have been developed. Besides all the improvements, the concept of ultrasound remained fixed. The ultrasound transducer transmits high-frequency ultrasound waves into a body and the pulses or waves penetrate the body and bounce back from the tissue. The bounced back ultrasound waves are detected by the transducer and convert to electrical signals. The time delay of each detected ultrasound pulse represents the path this pulse has traveled inside the tissue and the intensity of it represent the mechanical properties of the tissue it passed through and bounced back from. This information is used to form an image of the mechanical properties of the tissue. Since ultrasound had no known adverse effect on the patients, it is one of the safest and popular imaging technique [2].

Computed tomography was invented in 1970's. This technique uses computer-processed X-rays in different angles to form tomographic slices of the body. As it could provide tomographic slices, it improved the insight into the pathogenesis of the body and diagnosis. The early generation of X-ray imaging was slow due to the computational cost of this technique, but now a day, by developments in computer processing a CT scanner can reconstruct a tomographic image almost

instantly [3]. The two contributing inventors of this technology have received a Nobel Prize in medicine.

At the same time when the computed tomography was invented, Raymond Damadian discovered the difference of the nuclear magnetic relaxation times between the different tissues. As it was a promising discovery, several researchers all around the world worked around 20 years to develop this concept into Magnetic Resonance Imaging (MRI) technology. MRI sends strong magnetic waves through the body which causes the alignment of the protons. While these protons move back into their original positions, they radiate waves which are detected by the detector. These different radiations of particles inside the body are then used to form an image. Currently, MRI is widely used for diagnostic applications by providing very good differentiation between different soft tissues [4].

1.3. Breast Cancer

Breast, lung, and colorectum cancers are the three most commonly diagnosed cancers, representing one-half of all cancer cases among women. Breast cancer alone is expected to account for 29% all new cancer diagnoses in women in 2017. In average, one out of 8 American women will develop breast cancer over the course of their lifetime. Based on the statistics from American cancer society, right now there are around 2.8 million women with a history of breast cancer in the united states. This number includes women currently being treated and women who have completed receiving treatment. It has been estimated that in united states in 2017, 255,180 new cases of invasive breast cancer along with 63,410 new cases of non-invasive breast cancer will be detected.

Despite the decrease in death rates for breast cancer since 1989, it is estimated that unfortunately about 40,610 women will die from breast cancer in 2017 [12,13].

In breast cancer cells in the breast start to grow out of control and form a tumor. If the tumor cells have the potential to invade surrounding tissues or spread to distant areas of the body the tumor is called Malignant. Here we should note that most of the breast lesions do not invade surrounding tissue or spread to the other part of the body. These kinds of lesions are benign lesions.

Although benign lesions are abnormally grown inside the breast, unlike the malignant lesions they are not life-threatening for the patient as they are not invasive.

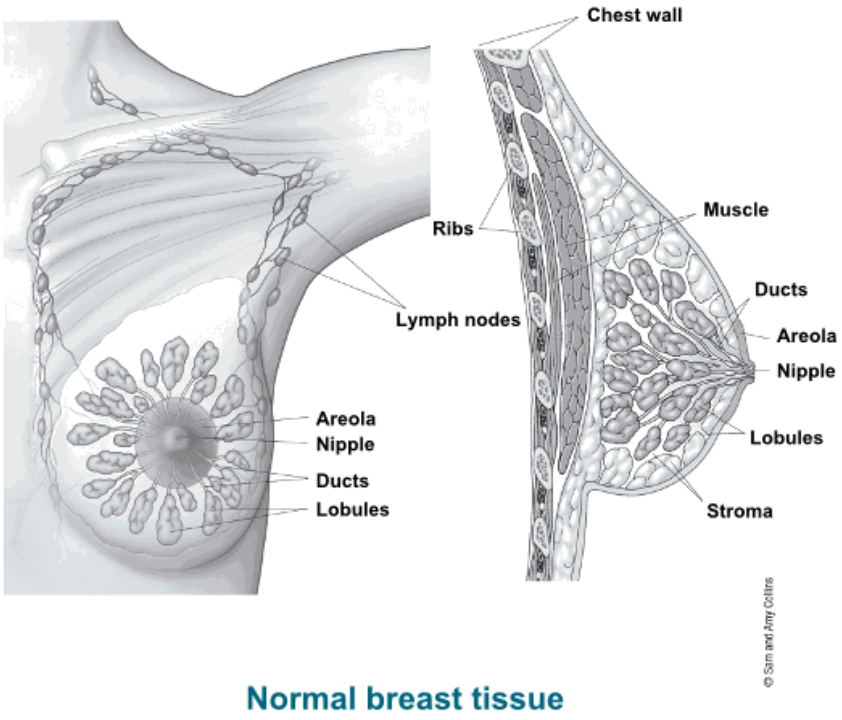

Figure 1.1. Normal breast tissue (ref. National cancer institute, [5,6])

1.4. Breast Cancer Diagnosis and Treatment Monitoring

Different imaging methods have been used for both detection and treatment monitoring phase of breast cancer. Conventional imaging methods such as mammography, ultrasound imaging (US), and magnetic resonance imaging (MRI), are the most commonly used methods to detect and diagnose breast cancer. Mammography as the most clinically used imaging modality for breast cancer diagnosis has relatively low sensitivity in early cancer diagnosis and weak sensitivity in women with dense breasts [14]. ultrasound demonstrates robust results in detecting breast cancer with comparable rate to mammography, but it still lacks sensitivity and specificity which results in several false positive cases [15]. MRI, on the other hand, shows a significantly higher sensitivity in breast cancer detection and diagnosis compared to US and mammogram, but the high costs of MRI and relatively low cancer detection rate in the general screening population limits its applicability as a screening and monitoring tool in several situations [14]. In the treatment phase of breast cancer, different modalities have been used to monitor the patient response to the neoadjuvant chemotherapy, while a method that can provide accurate results at early stages of treatment is yet to be found. On one hand, US and mammography, are two highly used methods to monitor the response of patients to neoadjuvant chemotherapy and they just show moderate sensitivity in the assessment of tumor response. On the other hand, dynamic contrast-enhanced MRI and 18F-fluorodeoxyglucose (18F-FDG) positron emission tomography/computed tomography (PET/CT) can predict the presence of residual tumor after completion of each NAC

which could decrease the patient additional exposure to ineffective and toxic treatments [15-17]. Although these methods have shown the ability in early identification of patients not responding to neoadjuvant chemotherapy, their equipment is bulky and expensive, and they require the injection of contrast agents which prevent them from being used repeatedly for monitoring patients during treatment.

Optical imaging using near infra-red light has shown promising results in detection and diagnosis of breast cancer and this technique will be discussed in chapter two with more details.

References

[1] Röntgen, Wilhelm Conrad. "On a new kind of rays." *Science* 3, no. 59 (1896): 227-231.

[2] Newman, Paul G., and Grace S. Rozycki. "The history of ultrasound." Surgical clinics of north America 78, no. 2 (1998): 179-195.

[3] Seeram, Euclid. Computed Tomography-E-Book: Physical Principles, Clinical Applications, and Quality Control. Elsevier Health Sciences, 2015.

[4] Lord, S. J., W. Lei, P. Craft, J. N. Cawson, I. Morris, S. Walleser, A. Griffiths, S. Parker, and N. Houssami. "A systematic review of the effectiveness of magnetic resonance imaging (MRI) as an addition to mammography and ultrasound in screening young women at high risk of breast cancer." European journal of cancer 43, no. 13 (2007): 1905-1917.

[5] American Cancer Society "Cancer Facts & Figures 2016," Cancer.org. (2016).

[6] Breast cancer organization "U.S. Breast Cancer Statistics 2017, " (http://www.breastcancer.org) (2017).

[7] Zheng, B., A. B. Hollingsworth, M. Y. Tan, R. G. Stough, and H. Liu. "Abstract P4-02-06: Improving efficacy of applying breast MRI to detect mammography-occult breast cancer." (2016): P4-02.

[8] Berg, Wendie A., Andriy I. Bandos, Ellen B. Mendelson, Daniel Lehrer, Roberta A. Jong, and Etta D. Pisano. "Ultrasound as the primary screening test for breast cancer: analysis from ACRIN 6666." *JNCI: Journal of the National Cancer Institute* 108, no. 4 (2016).

[9] Smith, Ian C., Steven D. Heys, Andrew W. Hutcheon, Iain D. Miller, Simon Payne, Fiona J. Gilbert, Antoinne K. Ah-See et al. "Neoadjuvant chemotherapy in breast cancer: significantly enhanced response with docetaxel." *Journal of Clinical Oncology* 20, no. 6 (2002): 1456-1466.

[10] Loo, Claudette E., Marieke E. Straver, Sjoerd Rodenhuis, Sara H. Muller, Jelle Wesseling, Marie-Jeanne TFD Vrancken Peeters, and Kenneth GA Gilhuijs. "Magnetic resonance imaging response monitoring of breast cancer during neoadjuvant chemotherapy: relevance of breast cancer subtype." *Journal of Clinical Oncology* 29, no. 6 (2011): 660-666.

2. Ultrasound-guided Diffuse Optical Tomography

2.1. Diffuse Optical Tomography

In last decades, the application of near infra-red (NIR) light for imaging has been under intense investigation. NIR diffuse optical tomography (DOT) is a noninvasive imaging technique that uses near infra-red light to assess optical properties of tissue. Because of the minimal light absorption of water at the near infra-red wavelength range (~700 to 900 nm), the light will penetrate sufficiently in tissue to acquire tomographic images [1-4]. Besides the low absorption of water at

near infra-red, this wavelength range is also sensitive to oxygenated and deoxygenated hemoglobin (HbO2 and Hb) [5,6]. Oxygenated and deoxygenated hemoglobin are two important chromophores found in the cancer lesions, and are related to tumor angiogenesis and cell activity. This sensitivity to oxy and deoxyhemoglobin results in several important applications for this technology such as brain activity monitoring and cancer detection. This sensitivity also resulted in promising results in assessing breast cancer. Besides that, DOT also has demonstrated great potential in the assessment of tumor vasculature response to neoadjuvant chemotherapy. DOT systems are portable, require no contrast agents, and have a low cost which makes them an ideal alternative for currently used modality for breast cancer diagnosis and monitoring in clinical settings. Besides aforementioned benefits, DOT can be used as a complimentary breast imaging method along with, ultrasound, X-ray mammography, and magnetic resonance imaging (MRI) in the diagnosis of breast cancer as well as treatment monitoring. Several research groups are investigating different techniques of diffuse optical tomography. In general, these researchers can be divided into 3 different groups, as time domain, frequency domain, and continuous wave DOT. Some groups, including our group, combine DOT imaging modality with another modality, such as ultrasound or MRI. We focused on frequency domain diffuse optical tomography systems and we combined it with ultrasound imaging method. We have studied the feasibility of using US-guided NIR imaging technique for detecting breast cancer as well as monitoring patients who were undergoing Neo-adjuvant chemotherapy [7].

2.2. Ultrasound-guided DOT

Ultrasound-guided diffuse optical tomography (US-guided DOT) uses ultrasound as a guidance to localize the lesion and improve the tissue illumination and reconstruction results. In our approach of US-guided DOT, we acquire 3 different measurements for each experiment. The very first measurements are from a known intralipid solution which will be used to calibrate the rest of the measurements from the patients. We then use ultrasound to localize the lesion and acquire multiple sets of measurements from the lesion site. Next, we move the probe to the contralateral breast to acquire multiple reference measurements. Then these measurements are used to reconstruct image as is described here.

First, the Intralipid datasets are loaded to calculate the system parameters for calibration, then the contralateral normal breast is measured, and data processed to estimate background tissue optical properties. These properties are used to compute a weight matrix for image reconstruction. The perturbation or scattered field is calculated as the difference between the reference data and the lesion data. Finally, by solving the inverse problem, the absorption distribution inside the medium can be estimated.

Born approximation is used to relate the scattered field (U_{sc}) measured at the probe surface to absorption variations in each volume element within the sample. In the Born approximation, the scattered field measured at source (s) and detector (d) is related to the weight W and the absorption change, $\Delta\mu_a$, inside the medium. By digitizing the imaging volume into N voxels, the matrix form of image reconstruction is given by

$$[U_{sd}]_{M\times 1} = [W]_{M\times N}[\Delta\mu_a]_{N\times 1} \quad (1)$$

where M is the total number of source-detector pairs, and W is the weight matrix, which describes the distribution of diffuse wave in the homogenous medium and characterizes the measurement sensitivity to different voxels inside the medium. To solve the unknown absorption distribution, the inverse problem is formulated as an optimization problem as: $min\|U_{sd} - W\Delta\mu_a\|^2$, where $\|.\|$ is the Euclidean norm. The conjugate gradient method is used to solve the inverse problem. Because the total number of source-detector pairs (M) on the probe is much smaller than the total number of voxels in the medium, the inverse problem is underdetermined and ill-posed. However, ultrasound is excellent in providing the information about the target depth and approximate size of target. We have integrated the target information from ultrasound and developed the dual-mesh imaging reconstruction algorithm. Briefly, the entire tissue volume is segmented based on initial co-registered ultrasound measurements into a lesion region *L* and a background region *B*. The image reconstruction matrix is given as:

$$[U_{sd}]_{M\times 1} = [W_L, W_B]_{M\times N}[M_L, M_B]^T{}_{N\times 1} \qquad (2)$$

where W_L and W_B are weight matrices for lesion and background regions, respectively, and $[M_L] = [\int_{1L} \Delta\mu_a(r')\, d^3 r', \ldots\ldots \int_{NL} \Delta\mu_a(r')\, d^3 r'$ and $[M_B] = [\int_{1B} \Delta\mu_a(r')\, d^3 r', \ldots\ldots \int_{NB} \Delta\mu_a(r')\, d^3 r')$ are total absorption distributions of lesion and background regions, respectively. The absorption distributions can be obtained by dividing the total absorption with the voxel sizes of lesion and background, respectively.

2.3. DOT for Neoadjuvant Chemotherapy

In the past decade, optical tomography and optical spectroscopy using near-infrared (NIR) diffused light has demonstrated great potential in the assessment of tumor vasculature and oxygen consumption responses to NAC [8-20]. The NIR technique utilizes intrinsic hemoglobin contrast, which is directly related to tumor angiogenesis, a key process required for tumor growth and metastasis. When multiple wavelengths are used, the optical absorptions at those wavelengths can be measured, and the proportions of oxygenated hemoglobin (oxyHb) and deoxygenated hemoglobin (deoxy-Hb) can be calculated, which are correlated with tumor oxygen metabolism and treatment resistance.

Optical systems are low cost and safe with no ionizing radiation and are ideally suited for repeated use at clinical settings. Recently, significant progress has been made on early prediction of NAC using Optical spectroscopy or tomography. In a study using NIR spectroscopy, 11 patients were monitored pretreatment and within one week of initial treatment [8]. DeoxyHb decreased within the first week in pathologically confirmed responders, whereas no significant change was found in non-responders. In addition, the measured total hemoglobin (tHb) decreased in all responders. Another study of 23 patients reported by the same group found a statistically significant increase, or flare, in oxyHb in responders on day 1, in contrast with a lack of flare or decrease in oxyHb noted on day 1 in non-responders [13]. An additional study reported by Ueda et al has shown that the pretreatment or baseline tumor oxygen saturation SO2 = oxyHb/tHb×100 correlates with the pathological complete response for patients undergoing NAC [16]. Recently, a

study reported by Jiang et al have shown that pretreatment tHb measured by Diffuse Optical Spectroscopic Tomographic imaging predicts breast tumor response to NAC [19].

We previously have developed a dual-modality approach by using the co-registered US to guide light illumination, reception and also image reconstruction [10,14, 20, 21]. This approach overcomes the problem of poor lesion localization of light due to optical scattering and improves reconstruction accuracy of lesions by using a priori lesion depth and size information obtained from US images. Recently, a multi-year study using US-guided Optical Tomography has completed. A total of 32 patients who were undergoing NAC were assessed pretreatment, at the end of every treatment cycle, and before surgery [15]. The significant findings from this group of patients are: 1) pretreatment tumor hemoglobin content (tHb, oxy- and deoxy-hemoglobin) predicts patient pathological response to NAC, 2) the percentage of tHb changes (%tHb) normalized to the pretreatment level can be used to further identify responders from non-responders at the early treatment cycles (2 to 3 weeks after the initiation of NAC), 3) combining widely used tumor pathologic variables and receptor status with hemoglobin functional parameters obtained before the initiation of NAC, substantially improved prediction can be achieved using a logistic prediction model [19].

To validate these results at multiple sites, we have developed third and fourth generation of US-guided NIR diffuse optical tomography (DOT) systems for clinical experiments. The new systems are compact, portable and robust in clinical operation. In the next two chapters, I focus on the development of the third and fourth generation of the US-guided NIR diffuse optical tomography (DOT) systems. The results of the clinical studies with the third generation of the system are presented in chapter three, and the phantom results of the fourth generation of the system are presented in chapter four.

References

[1] Boas, David A., Dana H. Brooks, Eric L. Miller, Charles A. DiMarzio, Misha Kilmer, Richard J. Gaudette, and Quan Zhang. "Imaging the body with diffuse optical tomography." *IEEE signal processing magazine* 18, no. 6 (2001): 57-75.

[2] Wu, Xue, Adam T. Eggebrecht, Silvina L. Ferradal, Joseph P. Culver, and Hamid Dehghani. "Fast and efficient image reconstruction for high density diffuse optical imaging of the human brain." *Biomedical optics express* 6, no. 11 (2015): 4567.

[3] Durduran, Turgut, Regine Choe, W. B. Baker, and Arjun G. Yodh. "Diffuse optics for tissue monitoring and tomography." *Reports on Progress in Physics* 73, no. 7 (2010): 076701.

[4] Larusson, Fridrik, Pamela G. Anderson, Elizabeth Rosenberg, Misha E. Kilmer, Angelo Sassaroli, Sergio Fantini, and Eric L. Miller. "Parametric estimation of 3D tubular structures for diffuse optical tomography." *Biomedical optics express* 4, no. 2 (2013): 271-286.

[5] Chance, Britton, Shoko Nioka, Jun Zhang, Emily F. Conant, Emily Hwang, Susanne Briest, Susan G. Orel, Mitchell D. Schnall, and Brian J. Czerniecki. "Breast cancer detection based on incremental biochemical and physiological properties of breast cancers: a six-year, two-site Study1." *Academic radiology* 12, no. 8 (2005): 925-933.

[6] Quarto, Giovanna, Lorenzo Spinelli, Antonio Pifferi, Alessandro Torricelli, Rinaldo Cubeddu, Francesca Abbate, Nicola Balestreri, Simona Menna, Enrico Cassano, and Paola Taroni. "Estimate of tissue composition in malignant and benign breast lesions by time-domain optical mammography." *Biomedical optics express* 5, no. 10 (2014): 3684-3698.

[7] Zhu, Quing, Andrew Ricci Jr, Poornima Hegde, Mark Kane, Edward Cronin, Alex Merkulov, Yan Xu, Behnoosh Tavakoli, and Susan Tannenbaum. "Assessment of functional differences in malignant and benign breast lesions and improvement of diagnostic accuracy by using US-guided diffuse optical tomography in conjunction with conventional US." *Radiology* 280, no. 2 (2016): 387-397.

[8] Cerussi, Albert, David Hsiang, Natasha Shah, Rita Mehta, Amanda Durkin, John Butler, and Bruce J. Tromberg. "Predicting response to breast cancer neoadjuvant chemotherapy using diffuse optical spectroscopy." *Proceedings of the National Academy of Sciences* 104, no. 10 (2007): 4014-4019.

[9] Choe, Regine, and Turgut Durduran. "Diffuse optical monitoring of the neoadjuvant breast cancer therapy." *IEEE Journal of selected topics in quantum electronics* 18, no. 4 (2012): 1367-1386.

[10] Zhu, Quing, Susan Tannenbaum, Poornima Hegde, Mark Kane, Chen Xu, and Scott H. Kurtzman. "Noninvasive monitoring of breast cancer during neoadjuvant chemotherapy using optical tomography with ultrasound localization." *Neoplasia* 10, no. 10 (2008): 1028-1040.

[11] Jiang, Shudong, Brian W. Pogue, Colin M. Carpenter, Steven P. Poplack, Wendy A. Wells, Christine A. Kogel, Jorge A. Forero et al. "Evaluation of breast tumor response to neoadjuvant chemotherapy with tomographic diffuse optical spectroscopy: case studies of tumor region-of-interest changes." *Radiology* 252, no. 2 (2009): 551-560.

[12] Soliman, Hany, Anoma Gunasekara, Mary Rycroft, Judit Zubovits, Rebecca Dent, Jacqueline Spayne, Martin J. Yaffe, and Gregory J. Czarnota. "Functional imaging using diffuse optical spectroscopy of neoadjuvant chemotherapy response in women with locally advanced breast cancer." *Clinical Cancer Research* 16, no. 9 (2010): 2605-2614.

[13] Roblyer, Darren, Shigeto Ueda, Albert Cerussi, Wendy Tanamai, Amanda Durkin, Rita Mehta, David Hsiang et al. "Optical imaging of breast cancer oxyhemoglobin flare correlates with

neoadjuvant chemotherapy response one day after starting treatment." *Proceedings of the National Academy of Sciences* 108, no. 35 (2011): 14626-14631.

[14] Zhu, Quing, Scott H. Kurtzman, Poornima Hegde, Susan Tannenbaum, Mark Kane, Minming Huang, Nan Guang Chen, Bipin Jagjivan, and Kristen Zarfos. "Utilizing optical tomography with ultrasound localization to image heterogeneous hemoglobin distribution in large breast cancers." *Neoplasia* 7, no. 3 (2005): 263-270.

[15] Zhu, Quing, Patricia A. DeFusco, Andrew Ricci Jr, Edward B. Cronin, Poornima U. Hegde, Mark Kane, Behnoosh Tavakoli, Yan Xu, Jesse Hart, and Susan H. Tannenbaum. "Breast cancer: assessing response to neoadjuvant chemotherapy by using US-guided near-infrared tomography." *Radiology* 266, no. 2 (2013): 433-442.

[16] Ueda, Shigeto, Darren Roblyer, Albert Cerussi, Amanda Durkin, Anais Leproux, Ylenia Santoro, Shanshan Xu et al. "Baseline tumor oxygen saturation correlates with a pathologic complete response in breast cancer patients undergoing neoadjuvant chemotherapy." *Cancer research* 72, no. 17 (2012): 4318-4328.

[17] Falou, Omar, Hany Soliman, Ali Sadeghi-Naini, Sara Iradji, Sharon Lemon-Wong, Judit Zubovits, Jacqueline Spayne et al. "Diffuse optical spectroscopy evaluation of treatment response in women with locally advanced breast cancer receiving neoadjuvant chemotherapy." *Translational oncology* 5, no. 4 (2012): 238-246.

[18] Falou, Omar, Ali Sadeghi-Naini, Sameera Prematilake, Ervis Sofroni, Naum Papanicolau, Sara Iradji, Zahra Jahedmotlagh et al. "Evaluation of neoadjuvant chemotherapy response in women with locally advanced breast cancer using ultrasound elastography." *Translational oncology* 6, no. 1 (2013): 17-24.

[19] Busch, David R., Regine Choe, Mark A. Rosen, Wensheng Guo, Turgut Durduran, Michael D. Feldman, Carolyn Mies et al. "Optical malignancy parameters for monitoring progression of breast cancer neoadjuvant chemotherapy." *Biomedical optics express* 4, no. 1 (2013): 105-121.

[20] Jiang, Shudong, Brian W. Pogue, Peter A. Kaufman, Jiang Gui, Michael Jermyn, Tracy E. Frazee, Steven P. Poplack, Roberta DiFlorio-Alexander, Wendy A. Wells, and Keith D. Paulsen. "Predicting breast tumor response to neoadjuvant chemotherapy with diffuse optical spectroscopic tomography prior to treatment." *Clinical Cancer Research* 20, no. 23 (2014): 6006-6015.

[21] Zhu, Quing, Liqun Wang, Susan Tannenbaum, Andrew Ricci, Patricia DeFusco, and Poornima Hegde. "Pathologic response prediction to neoadjuvant chemotherapy utilizing pretreatment near-infrared imaging parameters and tumor pathologic criteria." *Breast Cancer Research* 16, no. 5 (2014): 456.

3. Development of Third-gen US-guided DOT System

3.1. Abstract

In this chapter, I'll describe the development of the third generation of ultrasound guided diffuse optical tomography (US-DOT) system and then present the US-DOT system progress of utilizing ultrasound-guided diffuse optical tomography for predicting and monitoring neoadjuvant chemotherapy outcomes of breast cancer patients. The clinical results acquired with the developed prototype for the first patient will be discussed in this chapter. The patients have been closely monitored before NAC, at day 2, day 8, end of first three cycles of NAC and before surgery and

the imaging result is given as an example to demonstrate the potential of US-guided DOT technique and the performance of our system in clinical setting.

3.2. Introduction

Neoadjuvant chemotherapy (NAC) is increasingly used treatment to prepare patients with locally advanced breast cancers for surgery. The patient may receive neoadjuvant chemotherapy for breast cancer to shrink a tumor that is inoperable in its current state, so it can be surgically removed. Neoadjuvant therapy is also used for the patients whose tumor can be removed by mastectomy, to shrink the tumor enough to allow breast-conserving surgery. If a tumor does not respond (shrink) or continues to grow during neoadjuvant chemotherapy, the doctor may stop treatment and try another type of chemotherapy or perform surgery instead, depending on the stage of cancer.

The role of imaging for treated patients with neoadjuvant therapy for breast cancer is not only to evaluate the therapeutic response in terms of tumor shrinkage but also to predict the histological response to chemotherapy, which is correlated to survival rate. Surgery and histopathological analysis after neoadjuvant therapy allow for an objective assessment of the accuracy of imaging techniques in evaluating response. Different modalities have been used to differentiate between patients who respond and who don't respond to NAC; while a method which can provide accurate results at early stages of treatment is yet to be fully developed.

Physical examination is providing mediocre accuracy for assessing the response of locally advanced breast cancer to NAC treatment. It could be because of either palpation of a fibrotic and necrotic mass which may mimic a residual tumor mass or due to the resolution of post-biopsy phenomena such as hemorrhage and edema. Mammography and ultrasound are the most used methods for the initial staging and the assessment of tumor response to neoadjuvant chemotherapies. These methods are aiming the comparative measurement of the tumoral volume and the accuracy of them highly depends on the contrast between the tumor and the surrounding normal tissue. MRI allows morphological analysis of tumors and kinetic study of the contrast enhancement reflecting the richness of the vascularization, which could provide early identification of nonresponders. This method can predict the presence of residual tumor after completion of each NAC which could decrease the patient additional exposure to ineffective and toxic treatments. 18F-fluorodeoxyglucose (18F-FDG) positron emission tomography/computed tomography (PET/CT) have been reported to show good performance in excluding distant metastases prior to neoadjuvant chemotherapy (NAC) treatment. The usage of MRI and PET/CT are not suitable for repetitive use, because the equipment is bulky and expensive, and PET/CT require the injection of contrast agents as well. These constraints prevent them from being used repeatedly for monitoring patients during treatment.

Diffuse optical tomography (DOT) in the near-infrared (NIR) spectrum provides a unique approach for functional diagnostic imaging. This imaging technique can detect endogenous absorbers, and also determine the hemoglobin concentration and oxygen saturation. Near-infrared diffuse optical tomography (NIR-DOT) systems are portable, low cost, non-ionizing and require no contrast agents, which make them an ideal alternative for repeated use in clinical settings. Near-

infrared (NIR) diffuse optical tomography also has demonstrated great potential in the assessment of tumor vasculature response to neoadjuvant chemotherapy.

3.3. Previous Systems

In the past, we have developed two frequency domain DOT prototype systems which were used with commercial ultrasound systems in clinical studies. The first prototype system consisted of 12 pairs of laser diodes of wavelength 780 and 830 nm and eight parallel channel photomultiplier tube (PMT) detectors [1]. Each pair of dual-wavelength laser diodes delivered the light through an optical coupler to a hand-held probe of 10 cm diameter and all parallel detectors received the reflected light simultaneously via optical light guides mounted on the probe. The laser diodes were modulated at 140MHz and the detected signals were mixed with the 140.02 MHz reference signal and were further amplified and filtered at 20 KHz for processing. A commercial ultrasound array transducer was located in the middle of the probe for guiding the localization of breast lesions and image reconstruction.

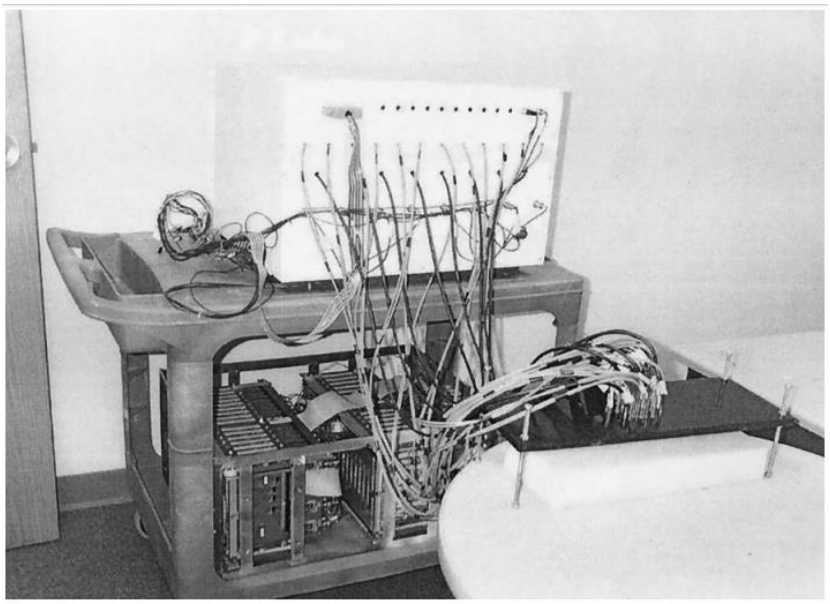

Figure.3.1. First generation of Ultrasound guided DOT system along with custom made 64 channels ultrasound system

The second prototype system consisted of four laser didoes of wavelengths 740, 780, 808 and 830nm which were sequentially switched by 4 x 1 and 1 x 9 optical switches to 9 source positions on the hand-held probe [2]. The detection included 10 photomultiplier tube (PMT) detectors and associated parallel electronics. The reflected light was coupled to the detectors via optical light guides mounted on the probe. The initial promising clinical results obtained from these prototype systems have been reported in several publications [2-7].

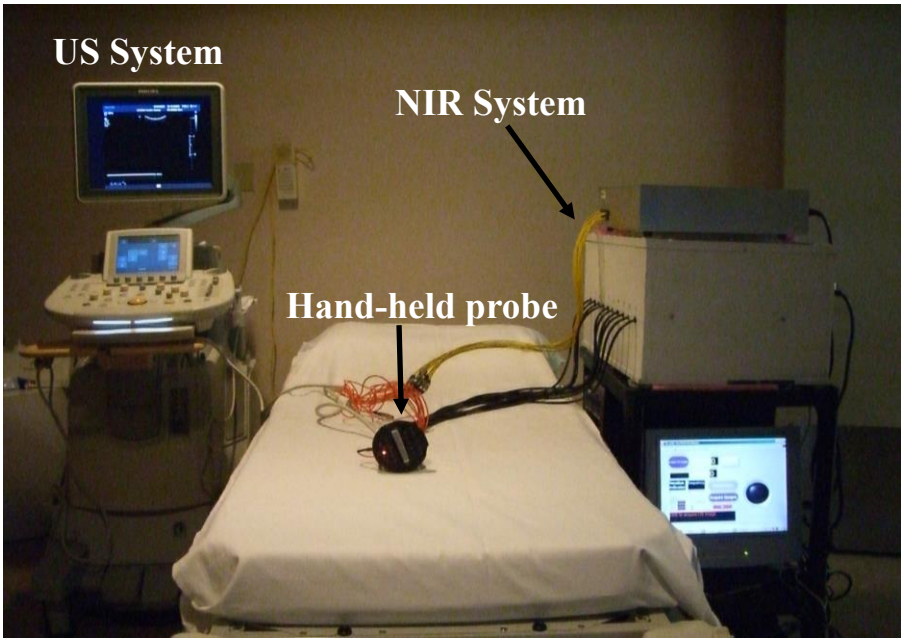

Figure.3.2. Second generation of Ultrasound guided DOT system along with a commercial ultrasound system

In both prototypes, a pair of National Instrument Data Acquisition (DAQ) boards and a desk top PC were used for data acquisition and display which has contributed to the bulkiness of the system in clinical studies.

3.4. Third-Gen of NIR-DOT system

In our early prototypes, the two National Instrument Data Acquisition (DAQ) boards and cables which connect DAQ boards inside a desktop PC to the NIR system have contributed to the cost and significant bulkiness of the system because two rigid RF shielding cables have to be used to reduce ~20KHz interference signals generated from beating of two high frequency signals from

source and detection systems. We have replaced the two NI DAQ boards with a custom-designed compact on-board DAQ board which will be housed inside the detection.

The DAQ consists of two AD7609 ICs (Analog Device), one SPARTAN 3E FPGA and 2MB SRAM. AD7609 has 8 simultaneously differential input channels with analog input range of ±10V which is ideal to handle a larger dynamic range of diffused light signals received from near and far source-detector pairs. The sampling speed of AD7609 is 200kHz and resolution is 18 bits. The SPARTAN 3E FPGA features 18-bit multipliers, 72Kbits of fast dual-port block RAM, and 500MHz+ operation. It has USB 2 full-speed port for FPGA configuration and data transfers to a lap top PC. The 2MB 16 SRAM is designed to buffer the data for one set of data acquired from all wavelengths and all sources and detectors. Figure 3.3 illustrate the block diagram of the FPGA based data acquisition board.

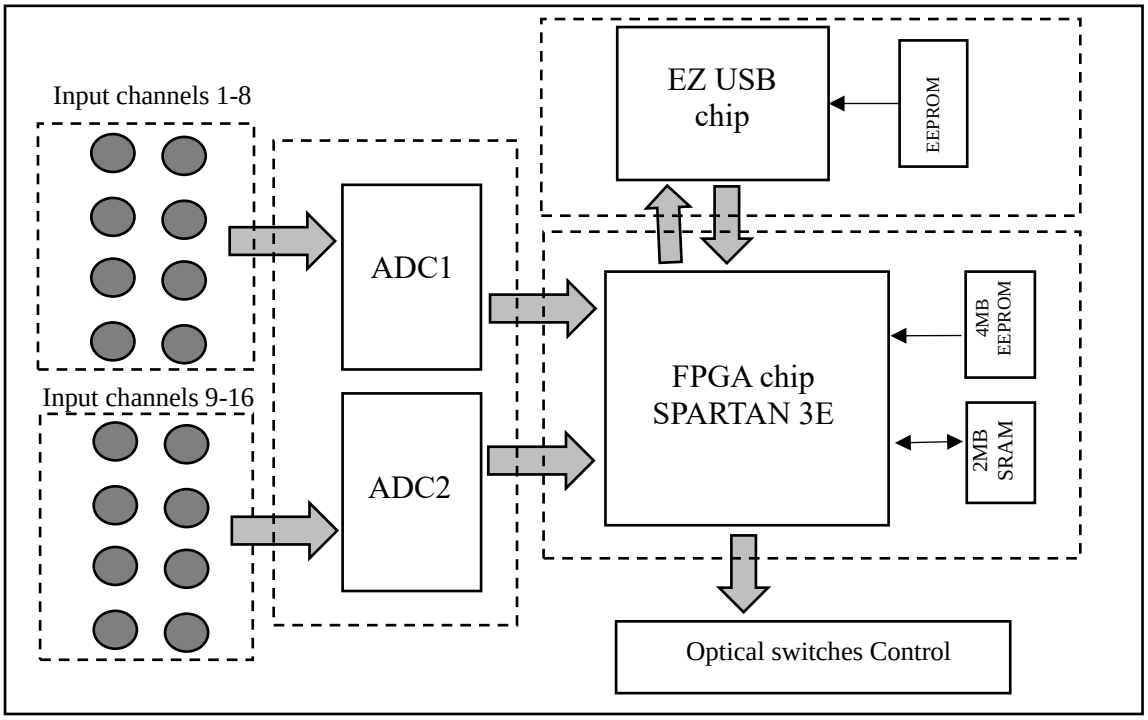

Figure.3.3. Block diagram of data acquisition board

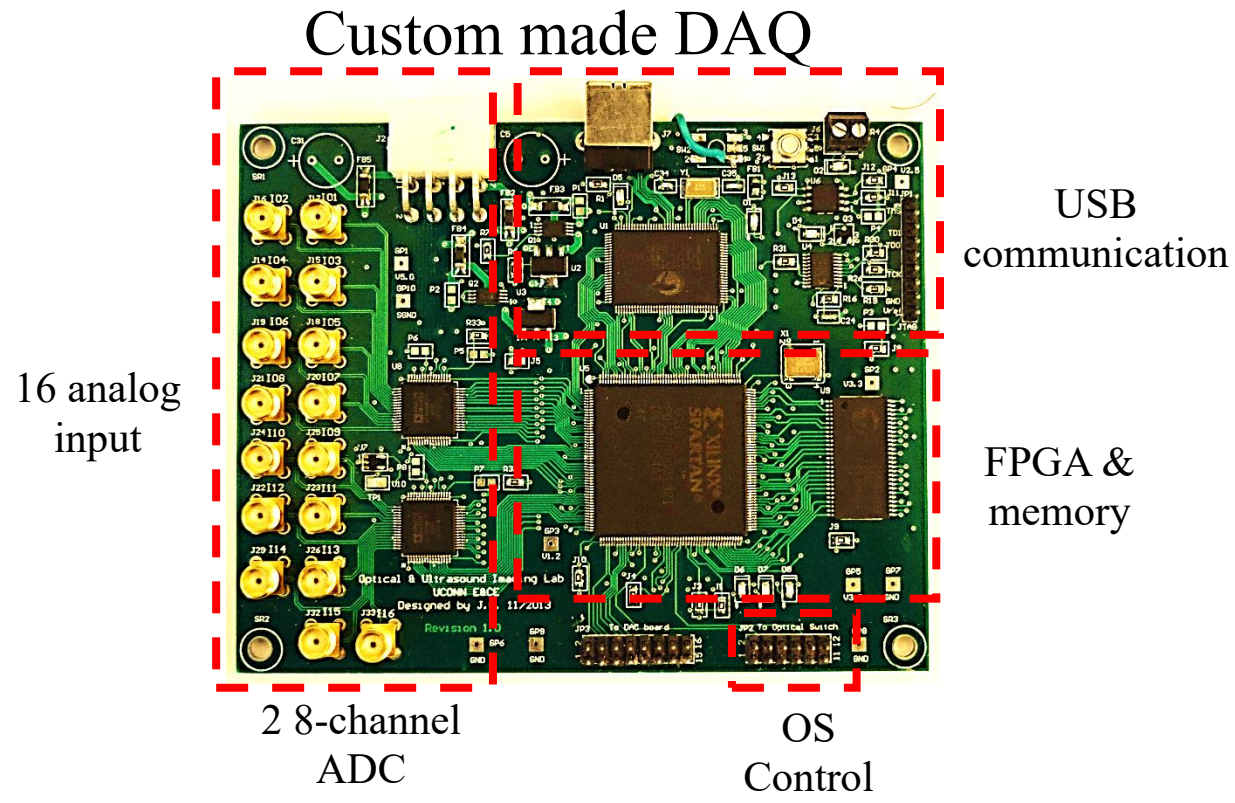

Figure 3.4. Final manufactured FPGA based data acquisition board

The SPARTAN 3E FPGA has a USB 2 full-speed port for FPGA configuration and data transfers to the laptop PC. Beside data acquisition, the FPGA is used to control the two optical switches of 4 x 1 and 1 x 9 for sequentially selecting one of the four wavelengths (740, 780, 808, 830nm) and one of the 9 source positions on the hand-held probe. PMT detectors and parallel electronic channels were used for parallel data acquisition

One of the other improvements in the third generation of our US-guided DOT system is the increase in the number of detection channels from 10 to 14. Besides that, a new layout of the electronics and optical components was designed to make the system as compact as possible without sacrificing the system heat dissipation, robustness, and signal to noise ratio.

Figure 3.5. shows the third prototype system dimensions (60 cm x 36 cm x 48 cm) and layouts.

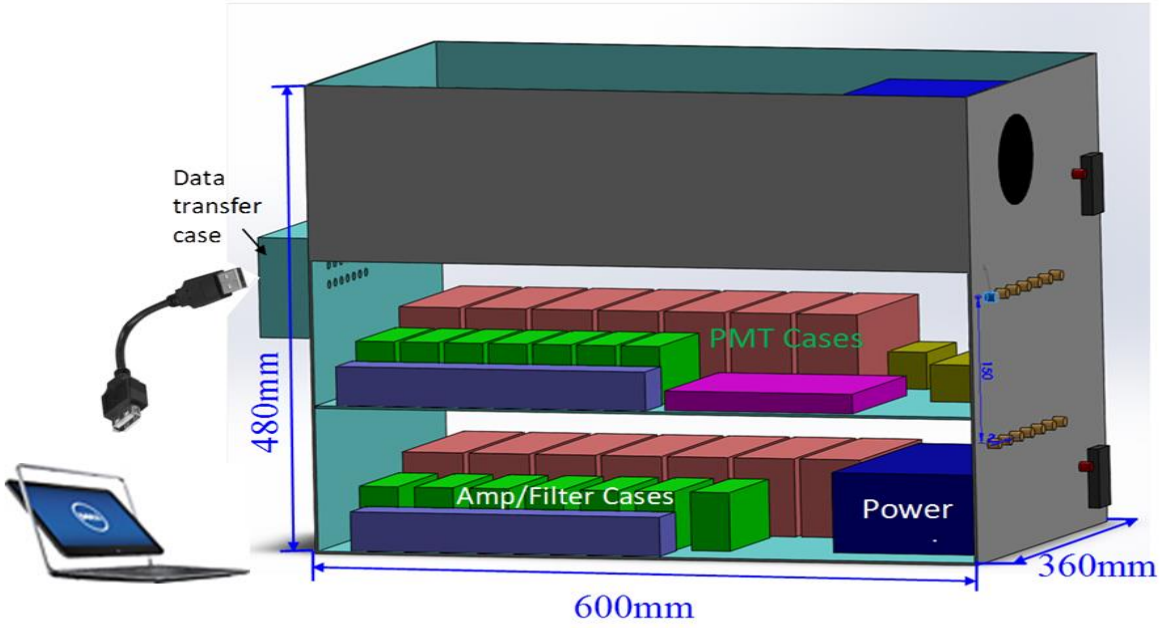

Figure 3.5. The layout of the optimized third gen DOT system

Our hybrid probe used in previous clinical studies was not robust. A commercial US probe was plugged into the open slot in the middle of the hybrid probe before each patient study and an engineer operator had to hold the bundle of optical fibers and the US probe tightly together during the study. Any significant bending of optical fibers during hand-held operation can produce bad channel (either detector or source) data with lower signal due to light loss. Often, we have had to manually remove these data during off-line processing. For the improved prototype, we use the following design to improve the hybrid probe for robust and user-friendly operation. As shown in Figure 3.6 (a), the US transducer will be inserted into the central slot of the probe base and firmly locked to the probe base by two spring plungers which push the transducer down at its shoulder.

After US transducer is connected, the probe cover which is used to cover and protect the optical fibers and US transducer can lock in with the probe. The final probe will be free of hand and fiber contact and easy to hold and operate as shown in Figure 3.6. (b).

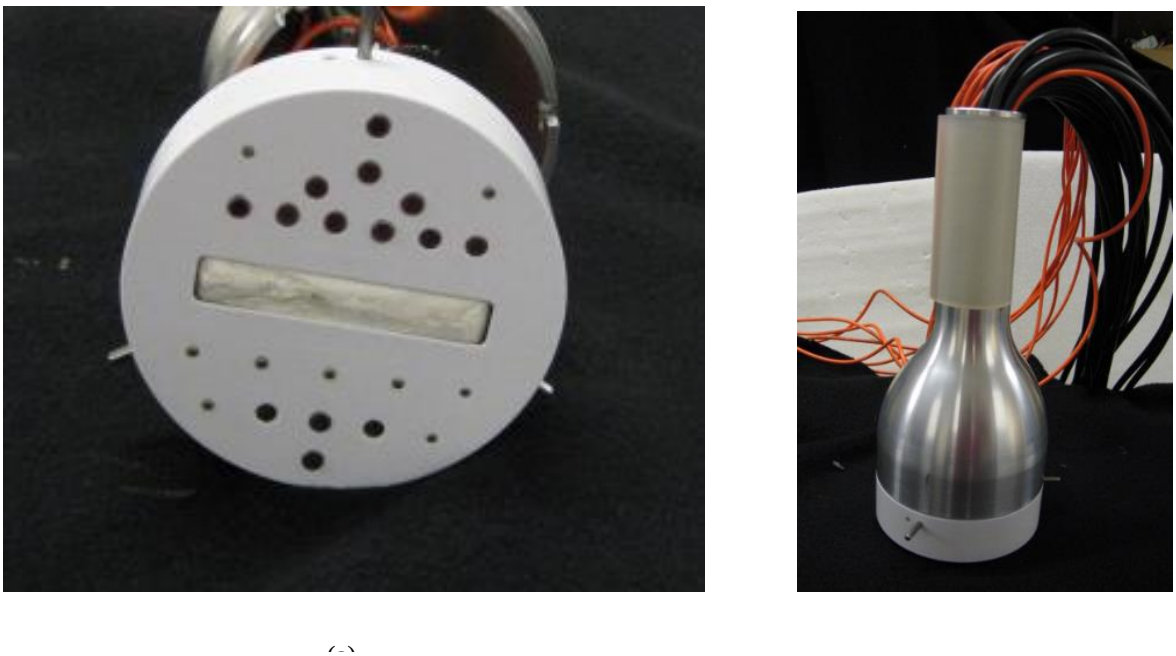

Figure 3.6. (a) The improved hybrid probe design; (b) Probe cover and probe.

The intralipid phantom data were collected using the improved NIR system. Figure 3.7(a) shows the amplitude vs. source-detector distance at 830nm, where amplitude is plotted in log(r2*I(r)). The amplitude shows good linearity, and the dynamic range of system can reach to 60 dB. Figure 3.7. (b) shows the phase vs. source-detector distance.

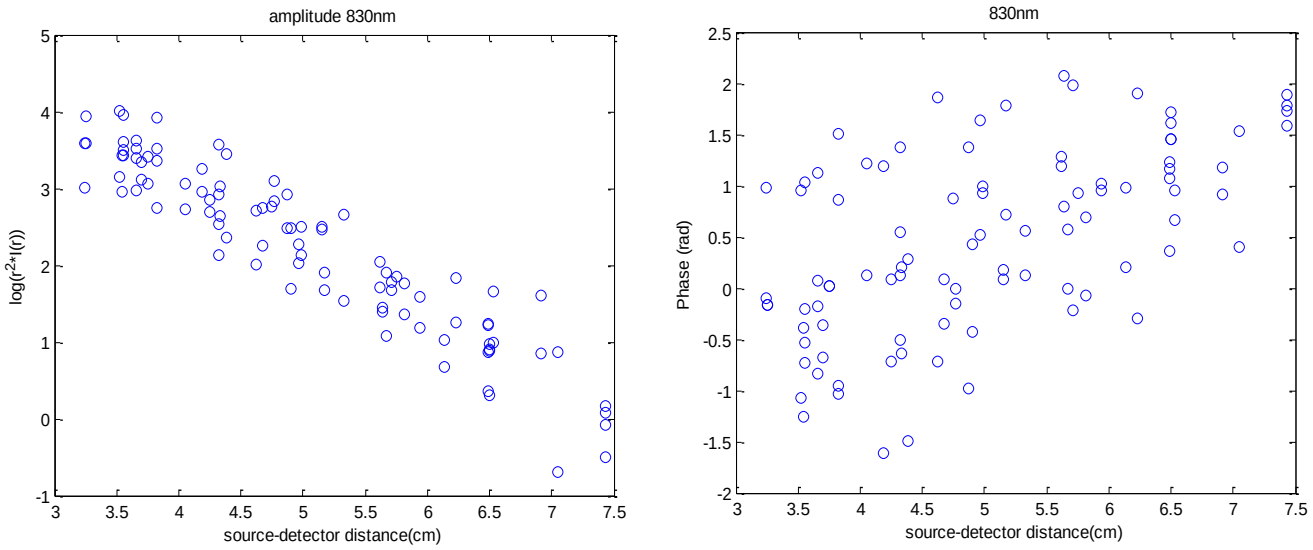

Figure 3.7. Intralipid phantom experiment data from the improved NIR system. (a) log(r2*I(r)) vs. source-detector distance; (b) Phase vs. source-detector distance

Figure 3.8 shows the block diagram of the optimized US-Guided NIR DOT system. Besides using a faster FPGA based data acquisition, by optimizing electronic components we were able increase number of detection channels from 10 to 14 in this new prototype. A custom made optical decoupling board have been designed to decouple any noise transfer between source and detector boxes and increase signal to noise ratio.

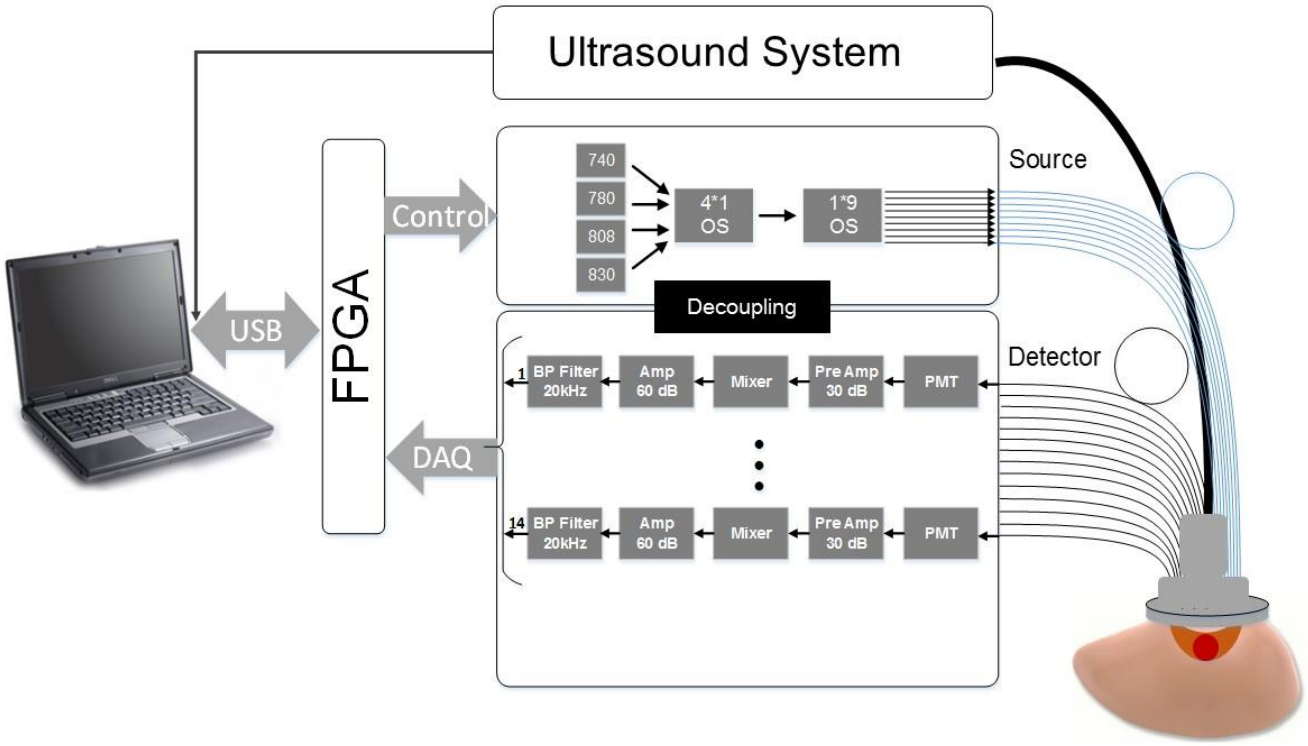

Figure. 3.8. Block diagram of the third generation of the ultrasound guided DOT system.

After described optimization steps, three prototypes of the third-gen ultrasound guided DOT system were developed and moved to three different hospitals for clinical studies.

Figure 3.9 shows a photograph of the upgraded NIR system used at the UCONN Health Center. A commercial ultrasound transducer can be readily plugged into the hand-held probe for simultaneous ultrasound and optical imaging.

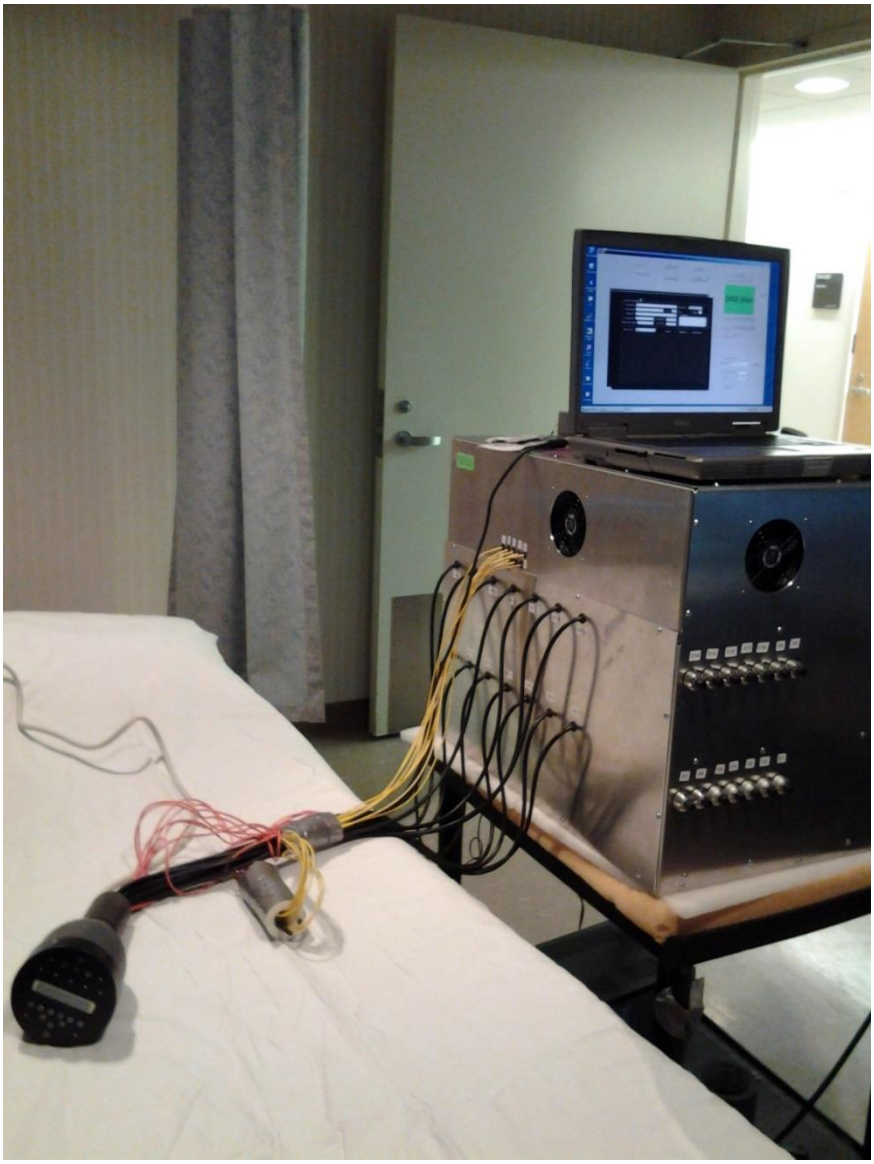

Figure 3.9. The upgraded NIR system currently used at the UCONN Health Center. The commercial ultrasound transducer is readily plugged into the combined probe which houses all source and detector fibers for light delivery and collection. The co-registered ultrasound images are captured by a video capture card and are used to guide the light illumination and optical imaging reconstruction.

3.5. Clinical Results

To validate the performance of the developed system in monitoring patients undergoing neoadjuvant chemotherapy, we have done a clinical study with three systems at three different hospitals. The study had IRB approval for all three sites and all patients consented to their participation. In this section, we are going to describe the clinical results obtained from the first patient. The first patient entered the new trial in March 2014 was a 37 years old woman with an invasive mammary carcinoma of mixed lobular and ductal features. The histological grade and nuclear grade were 3, and mitotic counts per 10 field high magnification were 9 and the Nottingham score was 8 out of 9. The receptor status was ER positive, PR positive and HER2 positive. The pre-treatment MRI image, co-registered ultrasound image, and the corresponding DOT total hemoglobin map are given in Figure 3.10 (a-c).

The total hemoglobin map is obtained in 7 slices from left to right and top to bottom corresponding to depths of 0.5 cm to 3.5 cm from the skin surface to the chest wall. Each slide is given in x-y spatial dimensions of 9 x 9 cm. The largest diameter of the tumor measured from MRI images was 3.6 cm, measured from US images was 2.5 cm. The total hemoglobin distribution provides functional information of tumor angiogenesis distribution and also quantitative levels. The tumor vascular distribution is mainly distributed at the periphery of the mass which is often seen in aggressive high-grade tumors. Quantitatively, the tHb level measured from the average maximum of several tHb images at the tumor site was 81.02 mol/L. The patient was treated with dual HER2 blockade of trastuzumab and pertuzumab for six cycles of total 18 weeks. The post-treatment MRI image, US, and DOT total hemoglobin map are given in Figure 3.10 (d-f). There

was no residual tumor seen in MRI images. The ultrasound image revealed a smaller mass which can be identified by the metal clip and total hemoglobin map revealed no vascular contrast. The final surgery report revealed a grossly identified mass of 5.5 cm at the location of 10-2 o'clock. Microscopically there were scattered tumor cells of ductal and lobular features within the scar tissue. The largest residual focus measured 1.25 mm. The Miller Payne grade was 4.

To assess the early changes during NAC, we have monitored the patient at day 2, day 8, end of cycle 1, 2 and 3. Figure 3.11 shows five sets of co-registered US images and total hemoglobin maps obtained at these time points and Figure 3.12 is the quantitative total hemoglobin level calculated from average maximum tHb levels with the average taken from several tHb images at the tumor site at each time point. It is interesting to note that at day 2, the periphery distribution of total hemoglobin is similar to the pre-treatment pattern, however, 24% higher total hemoglobin content was observed which may due to initial tumor vascular response to NAC treatment. At day 8, the total hemoglobin map has changed to more centralized distribution, but the level is still 12% higher than that at the pre-treatment level. At the end of cycle 1, the total hemoglobin level dropped to 73% of the pre-treatment level. At the end of cycles 2 and 3, the tHb is in the background level with no vascular contrast.

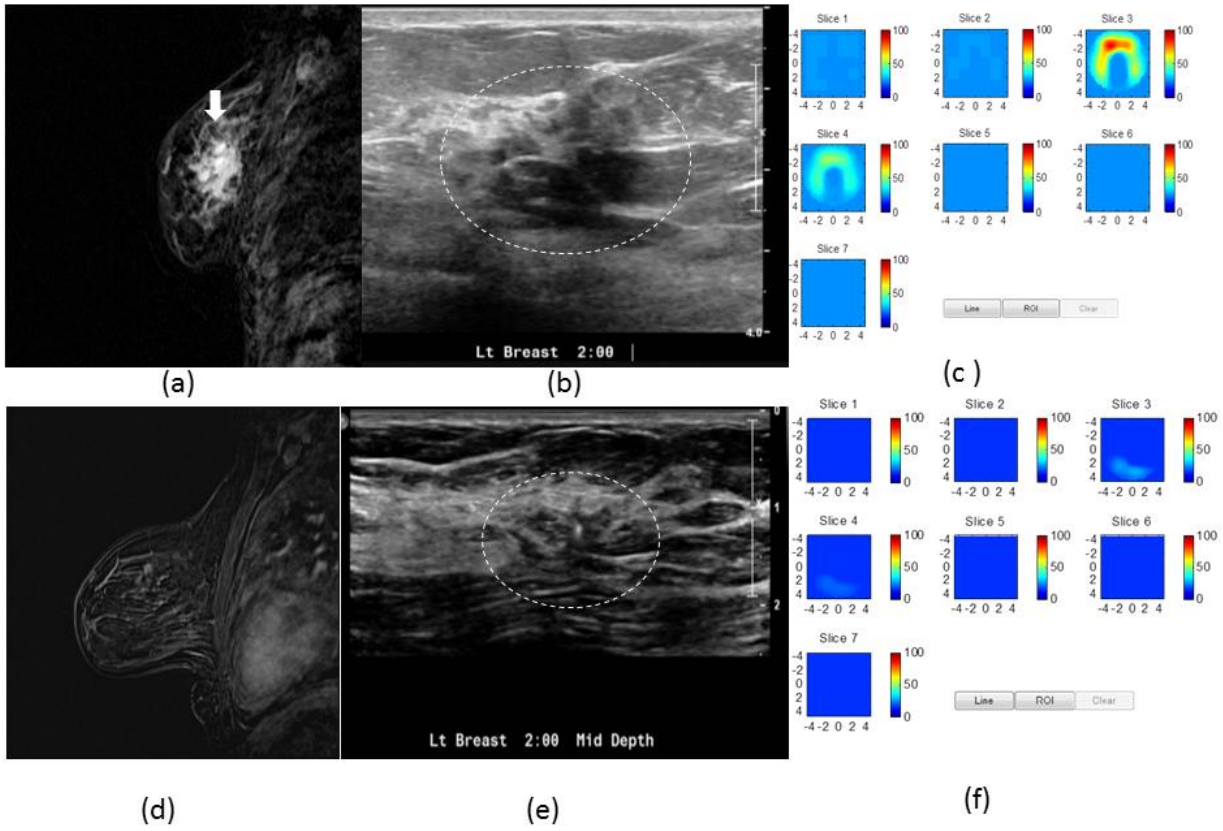

Figure 3.10. Patient with an invasive mammary carcinoma located at 2 o'clock position of her left breast. Baseline or pre-treatment MRI image (a), ultrasound image (b) and total hemoglobin map (c). Total hemoglobin map revealed periphery distribution which is often seen in aggressive carcinomas. Post-treatment MRI image (d), ultrasound image (e), and total hemoglobin map (f). MRI indicated no residual tumor and total hemoglobin map showed no vascular contrast. The total hemoglobin map is obtained in 7 slices from left to right and top to bottom corresponding to depths of 0.5 cm to 3.5 cm from skin surface to chest wall. Each slide is given in x-y spatial dimensions of 9 x 9 cm.

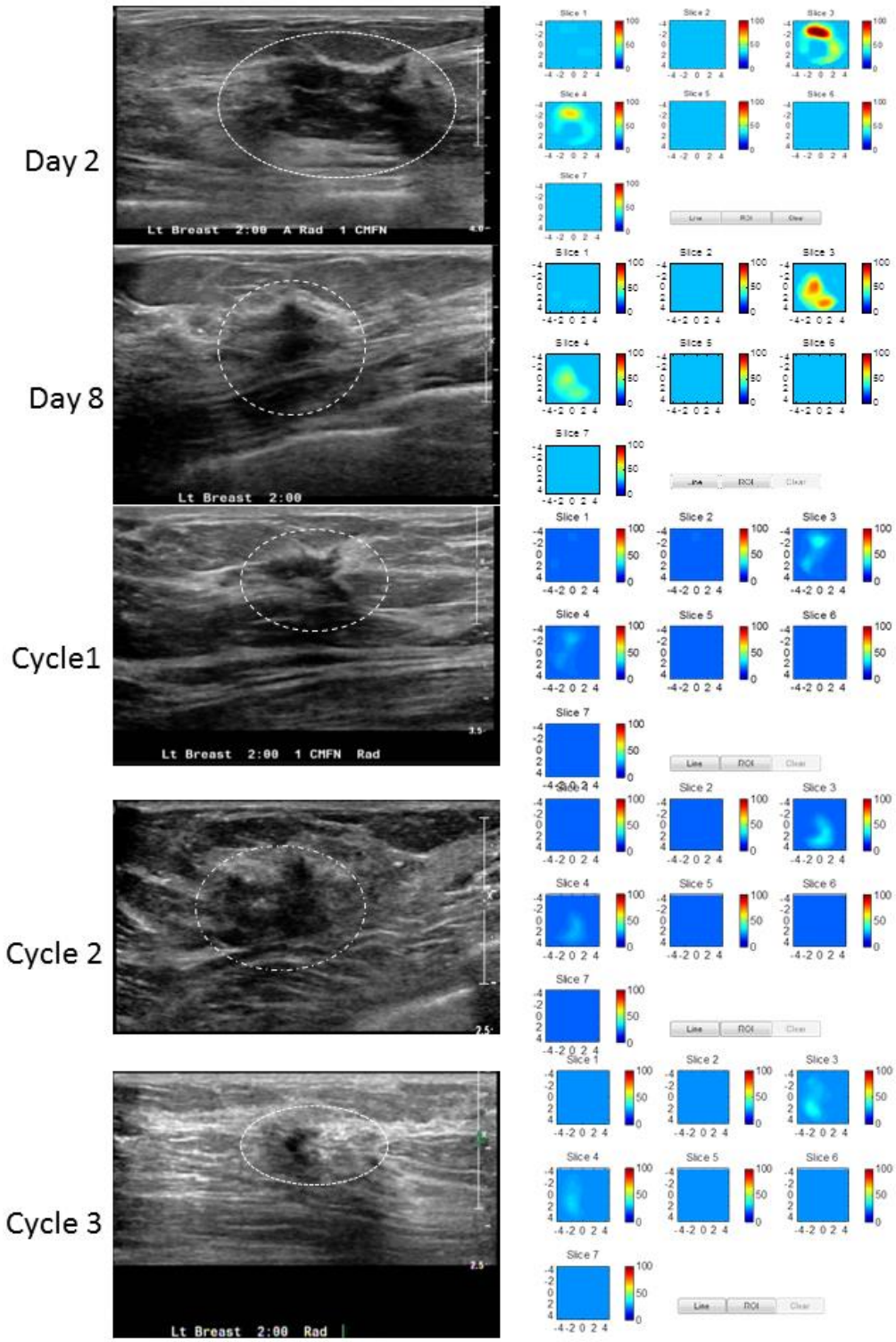

Figure 3.11. Co-registered US images and total hemoglobin maps obtained at five time points. Day 2, 8 and cycle 1 US images are zoomed into the depth range of 0 to 4 cm while Cycle 2 and 3 US images are zoomed in to the range of 0 to 2.5 cm to better visualize the tumor.

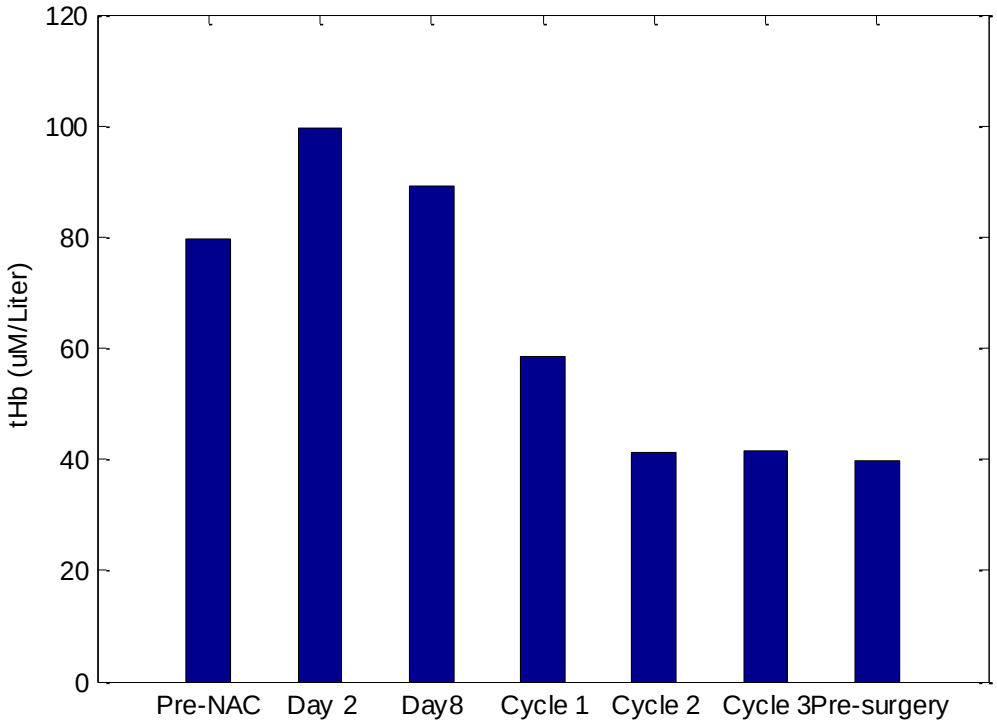

Figure 3.12. Quantitative total hemoglobin level calculated from average maximum tHb levels with the average taken from several tHb images at the tumor site at each time point.

3.6. Summary

In summary, we have designed and constructed an upgraded frequency domain diffuse optical tomography system for robust and reliable clinical operation at multiple clinical sites. The probe can be easily adapted to any commercial ultrasound probe and the system is compact in size. Three prototypes of the system were developed and used in three different hospitals. The systems have been used for assessing neoadjuvant chemotherapy response of breast cancer patients and the results are presented in the following sections. The results of one patients has been presented here

and it shows promising results in prediction of patient's response to neoadjuvant chemotherapy as early as first cycle of chemotherapy. These 3 systems in three hospitals have been continued to be used for clinical studies and the results has been submitted to the journal of clinical cancer research.

The results presented in this chapter have been published in multiple journals and conference proceeding as listed in the reference [8-11]

References

[1] Chen, Nan Guang, Puyun Guo, Shikui Yan, Daqing Piao, and Quing Zhu. "Simultaneous near-infrared diffusive light and ultrasound imaging." *Applied optics* 40, no. 34 (2001): 6367-6380.

[2] Zhu, Quing, Patricia A. DeFusco, Andrew Ricci Jr, Edward B. Cronin, Poornima U. Hegde, Mark Kane, Behnoosh Tavakoli, Yan Xu, Jesse Hart, and Susan H. Tannenbaum. "Breast cancer: assessing response to neoadjuvant chemotherapy by using US-guided near-infrared tomography." *Radiology* 266, no. 2 (2013): 433-442.

[3] Zhu, Quing, Susan Tannenbaum, Poornima Hegde, Mark Kane, Chen Xu, and Scott H. Kurtzman. "Noninvasive monitoring of breast cancer during neoadjuvant chemotherapy using optical tomography with ultrasound localization." *Neoplasia* 10, no. 10 (2008): 1028-1040.

[4] Zhu, Quing, Scott H. Kurtzman, Poornima Hegde, Susan Tannenbaum, Mark Kane, Minming Huang, Nan Guang Chen, Bipin Jagjivan, and Kristen Zarfos. "Utilizing optical tomography with ultrasound localization to image heterogeneous hemoglobin distribution in large breast cancers." *Neoplasia* 7, no. 3 (2005): 263-270.

[5] Zhu, Quing, Edward B. Cronin, Allen A. Currier, Hugh S. Vine, Minming Huang, NanGuang Chen, and Chen Xu. "Benign versus malignant breast masses: optical differentiation with US-guided optical imaging reconstruction." *Radiology* 237, no. 1 (2005): 57-66.

[6] Zhu, Quing, Minming Huang, NanGuang Chen, Kristen Zarfos, Bipin Jagjivan, Mark Kane, Poornima Hedge, and Scott H. Kurtzman. "Ultrasound-guided optical tomographic imaging of malignant and benign breast lesions: initial clinical results of 19 cases." *Neoplasia* 5, no. 5 (2003): 379-388.

[7] Zhu, Quing, Poornima U. Hegde, Andrew Ricci Jr, Mark Kane, Edward B. Cronin, Yasaman Ardeshirpour, Chen Xu et al. "Early-stage invasive breast cancers: potential role of optical tomography with US localization in assisting diagnosis." *Radiology* 256, no. 2 (2010): 367-378.

[8] Xu, Chen, Hamed Vavadi, Alex Merkulov, Hai Li, Mohsen Erfanzadeh, Atahar Mostafa, Yanping Gong, Hassan Salehi, Susan Tannenbaum, and Quing Zhu. "Ultrasound-guided diffuse optical tomography for predicting and monitoring neoadjuvant chemotherapy of breast cancers: recent progress." *Ultrasonic imaging* 38, no. 1 (2016): 5-18.

[9] Quing Zhu, Susan Tannenbaum, Scott H. Kurtzman, Patricia DeFusco, Andrew Ricci, Hamed Vavadi, Feifei Zhou, Chen Xu, 5 Alex Merkulov, Poornima Hegde, Mark Kane, Liqun Wang, Kert Sabbath, “An Optimal Time Window for Assessing Breast Cancer Response to Predicting Neoadjuvant Chemotherapy using Biomarkers and Pre-treatment and Early Changes of Hemoglobin Content Measured by US-guided Diffuse Optical” Journal of clinical cancer research (Under review)

[10] Xu, Chen, Hai Li, Guangqian Yuan, Hamed Vavadi, and Quing Zhu. "Development of a robust and fast calibration procedure for diffuse optical tomography." In *SPIE BiOS*, pp. 93192E-93192E. International Society for Optics and Photonics, 2015.

[11] Xu, Chen, Hamed Vavadi, Jigi Chen, Mohsen Erfanzadeh, Quangqian Yuan, Yanping Gong, Hassan Salehi, Hai Li, and Quing Zhu. "Toward miniature diffuse optical tomography system for assessing neoadjuvant chemotherapy." In *Biomedical Optics*, pp. BM3A-57. Optical Society of America, 2014.

4. Development of Fourth-gen US-guided DOT system

4.1. Abstract

Based on the statistics from World Health Organization, breast cancer is the most common cancer among women worldwide, claiming the lives of hundreds of thousands of women each year. Near-infrared diffuse optical tomography (DOT) has demonstrated a great potential as an adjunct modality for differentiation of malignant and benign breast lesions and for monitoring treatment response in patients with locally advanced breast cancers. The path toward commercialization of DOT techniques depends upon the improvement of robustness and user-friendliness of this technique in hardware and software. In the past, our group has developed frequency domain

prototype systems which were used in several clinical studies. In this study, we introduce our recently developed US-guided DOT system which is being improved in terms of size, robustness, and user-friendliness by several custom electronics and improved mechanical design. The new system benefits from a new user interface with includes automated data selection, outlier removal, and lesion boundary detection as well as a new calibration method based on the depth and size of the lesion detected from the ultrasound image. With all these improvements, our new system is more robust and accurate which is one step closer to commercialization and widespread use of this technology in clinical settings. This system is aimed to be used by minimally trained user in the clinical settings with robust performance. The system performance has been tested with several phantom experiments and the results show decent accuracy in terms of reconstructed absorption as well as strong sensitivity in terms of oxygen saturation. The system was moved to a hospital and was used in a clinical study to monitor patients undergoing neoadjuvant chemotherapy and the results are presented.

4.2. Introduction

Breast cancer is the most common cancer among women and is expected to account for 29% all new cancer diagnoses in women in 2017. Based on the statistics from American cancer society, there are around 2.8 million women with a history of breast cancer in the United States (US). This number includes women currently being treated and women who have completed treatment. In 2017, 255,180 new cases of invasive breast cancer along with 63,410 new cases of non-invasive breast cancer will be detected in US. Despite the decrease in death rates for breast cancer since

1989, it is estimated that about 40,610 women in the U.S. will die in 2017 from breast cancer [1,2]. Treatment for many breast cancer patients starts with preoperative or neoadjuvant therapy, which includes chemotherapy, targeted therapy or hormone therapy to shrink the size of the lesion and control the growth of the tumor before breast surgery. Neoadjuvant chemotherapy and hormone therapy drugs are mostly same as those used after surgery (adjuvant therapy) and can shrink a larger tumor enough so that lumpectomy plus radiation therapy becomes an alternative option to mastectomy. Patients are usually assessed during neoadjuvant therapy on response in case of tumor progression [3].

Different imaging methods have been used for both detection and treatment monitoring of breast cancer. Conventional imaging methods such as Mammography, ultrasound imaging (US), and magnetic resonance imaging (MRI), are the most commonly used methods for breast cancer diagnosis. Mammography as the most clinically used imaging modality for breast cancer screening and diagnosis has relatively low sensitivity in early cancer diagnosis especially low sensitivity in women with dense breasts [4]. US demonstrates robust results in detecting breast cancer with comparable rate to mammography, but it still lacks sensitivity and specificity [5]. MRI, on the other hand, shows a significantly higher sensitivity in breast cancer detection and diagnosis compared to US and mammogram, but the high costs of MRI and low cancer detection rate in the general screening population limits its applicability as a screening and monitoring tool [4]. In the treatment phase of breast cancer, different modalities have been used to monitor the patient response to the neo-adjuvant therapy, while a method which can provide accurate results at early stages of treatment is yet to be found. On one hand, US and mammography, are two highly used methods to monitor the response of patients to Neo-adjuvant therapy and they just show moderate sensitivity in the assessment of tumor response. On the other hand, dynamic contrast-enhanced

MRI and 18F-fluorodeoxyglucose (18F-FDG) positron emission tomography/computed tomography (PET/CT) can predict the presence of residual tumor after completion of each NAC which could decrease the patient additional exposure to ineffective and toxic treatments [4-6]. Although these methods have shown the ability in early identification of nonresponses, their equipment is bulky and expensive, and they require the injection of contrast agents which prevent them from being used repeatedly for monitoring patients during treatment.

Near-infrared (NIR) diffuse optical tomography (DOT) is a noninvasive imaging technique that uses near-infrared light to assess optical properties of tissue. Because of the minimal light absorption of water at the near infra-red wavelength range (~700 to 900 nm), the light will penetrate sufficiently in tissue to acquire tomographic images. Besides the low absorption of water at near infra-red wavelength range, this wavelength range is also sensitive to oxygenated and deoxygenated hemoglobin (HbO2 and Hb) [7-8]. DOT has shown promising results in the initial assessing breast cancer because of its sensitivity to oxygenated and deoxygenated hemoglobin. Besides that, DOT also has demonstrated great potential in the assessment of tumor vasculature response to neoadjuvant chemotherapy. DOT systems are usually portable, require no contrast agents, and have relatively low cost. Although these characteristics of DOT systems should make them an ideal alternative for currently used modality for breast cancer diagnosis and monitoring in clinical settings, but the low spatial resolution and lesion location uncertainty caused by intense light scattering in soft tissue limits the wide use of this technology in the clinical setting. To overcome this lower spatial resolution and location uncertainty, several groups investigated the complimentary use of DOT along with other conventional imaging techniques. Multiple groups have investigated the use of DOT guided by mammogram, US, and MRI [9-11] and demonstrated DOT as a promising complementary method to the existing imaging modalities. We have studied

the feasibility of using US-guided NIR imaging technique for detecting breast cancer as well as monitoring patients who were undergoing Neo-adjuvant chemotherapy [11,12].

In recent years, we have devoted a great deal of time to improve the robustness of the diffuse optical tomography in terms of hardware and software [12-14]. In this paper, we are introducing a robust and commercially designed ultrasound-guided diffuse optical tomography system which is moving this technology one step further in the commercialization and wide use in clinical setting. A finite element based calibration method has been introduced to improve the sensitivity of the system at different depth and size. The depth and size information has been made available from co-registered ultrasound images. The performance of the system was evaluated by solid and blood phantoms for absorption, total hemoglobin, and oxygen saturation sensitivity. The system was then moved to hospital and used in the clinical study for monitoring patient's response to neoadjuvant chemotherapy. The monitoring results of the first patient are presented in this paper.

4.3. Method

4.3.1. System Structure

The miniaturized frequency domain imaging system was designed in order to move the ultrasound-guided diffuse optical tomography system one step closer to wide use in clinical setting. This system benefits from miniaturized hardware design which reduces the size and improves the robustness of the DOT system. The system has four laser diodes of wavelengths 730, 785, 808 and 830nm as sources to characterize the breast tissue within a near-Infra red range and provide oxygenated, deoxygenated, and total hemoglobin concentration inside the breast tissue. These 4

laser diodes were sequentially switched by 4 x 1 and 1 x 9 optical switches to 9 source positions on the hand-held probe. The reflected light from each source location was received simultaneously at 14 parallel detection fibers and passed with fiber bundles to 14 PMT detectors. This system uses heterodyne detection channels, at which the light sources were modulated at 140.2MHz and the detected signals were mixed with the 140 MHz reference signal. The output of the mixers at each channel was further amplified and filtered at 20 kHz. Since we are guiding our DOT with ultrasound, a commercial ultrasound array transducer was located in the middle of the probe to estimate the approximate depth and size of the lesion. In order to make this system appropriate to be used by physicians in the clinical setting, a commercial case has been designed system based on hospital safety and standards. For the convenience of the physicians, a moveable arm has been added to this system in order to accommodate the touchscreen laptop for controlling data acquisition and processing.

Fig. 4.1. Shows the diagram of the miniaturized system along with the developed system which is currently moved to the hospital for clinical studies.

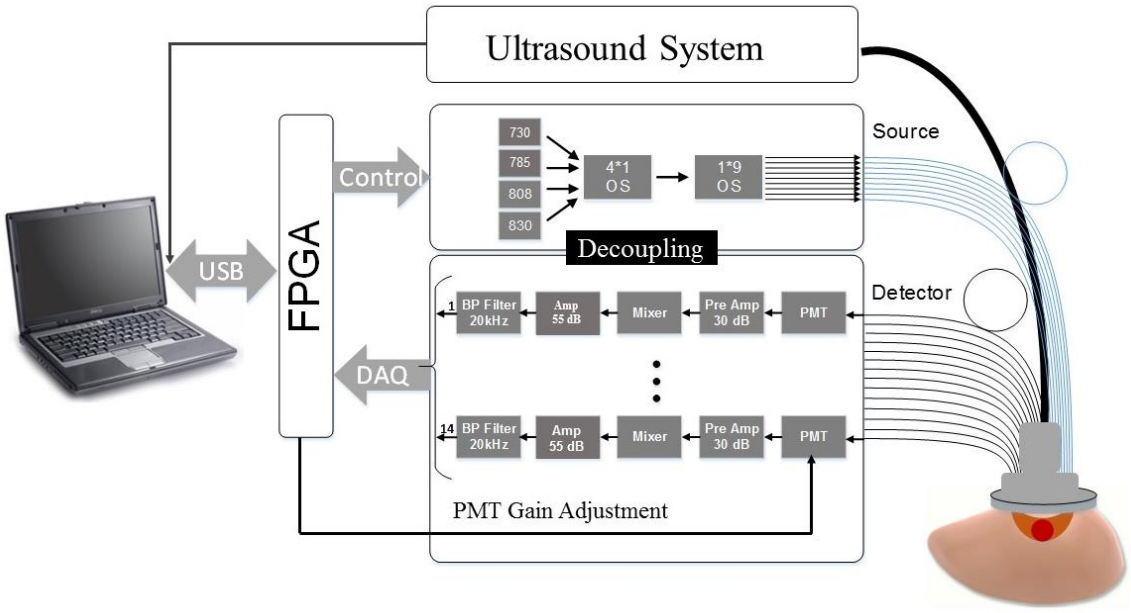

Figure 4.1. Block diagram of miniaturized diffuse optical tomography system

4.3.2. Hardware Miniaturization

In this section, we describe the specific hardware miniaturization and improvements in our new system. This system benefits from a miniaturized custom-made laser diode driver which can accommodate up to 6 laser diodes, a miniaturized custom-made detection circuit to reduce number of unnecessary cables and reduce the size and cost of the detection circuit, and a robust hand-held probe which would enable us to connect the DOT system with commercial ultrasound system in less than a minute in clinical setting. The details of hardware miniaturization processes are described in the following subsections.

4.3.2.1. Laser Diode Driver and Cooling

The DOT system has two main blocks as source and detector subsystems. One of the key contributing factors in the size of the DOT system in the source subsystem is the light source, its

associated current driver, frequency modulation blocks, and the cooling system. To miniaturize the laser diode drivers, a custom-made board is designed in order to reduce the bulkiness and cost of light source drivers. In our earlier prototypes, we were using 4 Thorlab's current driver boards which were running each laser diodes. This units were not only costly, they would increase the total size of the source subsystem as we had to mount 4 of them inside the source subsystem. In our new system, we have designed a single laser diode board which can accommodate up to 6 laser diodes of type A and C. This module can provide a stable feedback controlled DC current for up to 200 mA for each laser diode. Since we are modulating our light sources, this module has 6 build in bias-tee and a RF input to modulate laser diodes with different RF frequencies. In our system, all 4 light sources have been modulated at 140.02 MHz, which provide 4 frequency modulated light sources at 4 different wavelengths. The other two laser diode driver ports are not used in our current prototype since we are only using 4 wavelengths. Currently we are using four wavelengths of 730, 785, 808 and 830 nm in NIR range which are sensitive to oxy and deoxy hemoglobin. The output of the lasers is multiplexed via two optical switches from Piezojena co to 9 different positions and the light is delivered to the tissue with 9 optical fibers through our hand-held probe.

Besides the laser diode current driver, we have tried to reduce the size of our laser diodes cooling by using pigtailed laser diodes with thermal block from OZ Optics (LDPC-T3). The LDPC-T3 laser diode assembly has a flat metal surface on the back to attach a thermoelectric cooler (TEC). The LDPC-T3 laser diode assembly has a built-in 10 kΩ NTC type thermistor sensor which provides feedback for TEC cooler controller. The TCM1000T TEC control module from Thorlabs has been used to control current TEC cooler through a Thermal Electric Cooler. The module is designed to maintain temperature based on feedback provided from a 10 kΩ NTC type thermistor sensor. Temperature is set and monitored using a scaled voltage based on the thermistor resistance

for a given temperature, and is available at test points referenced to system ground. In this system the TEC drivers have been adjusted to keep the all 4 laser diodes below room temperature at 15 degrees Celsius.

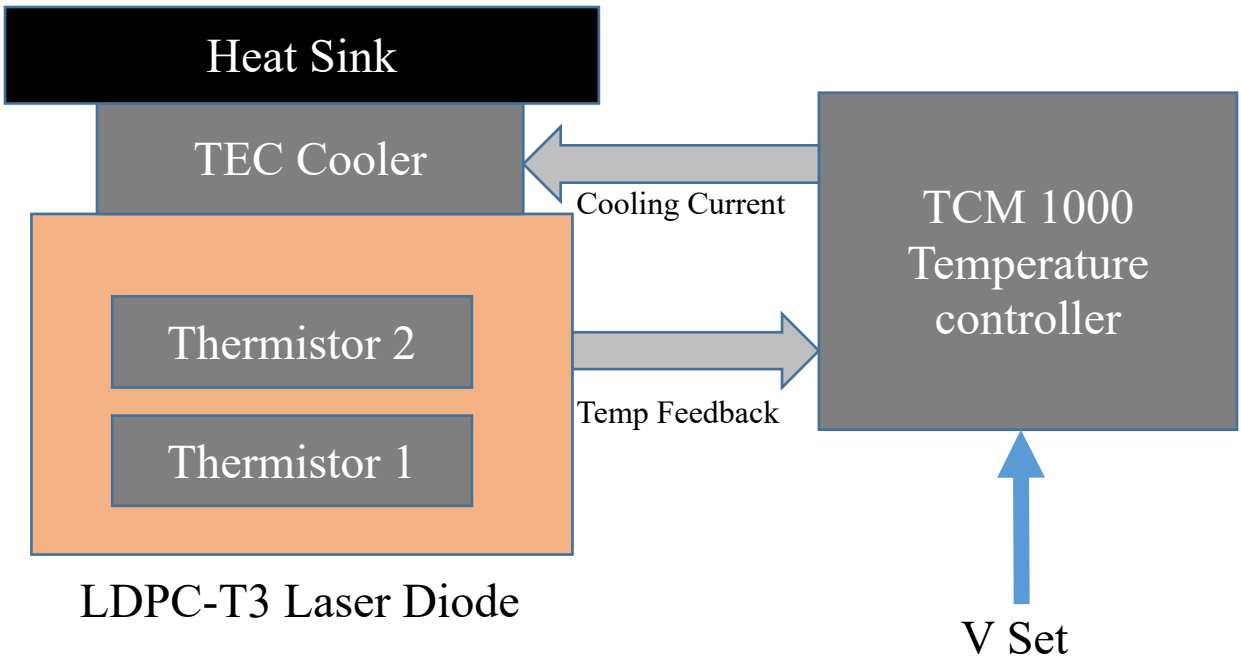

Figure 4.2. Thermal block laser diodes and it's cooling system for forth-Gen DOT

4.3.2.2. Miniaturized Detection Board

A custom-made miniaturized detection circuit is designed in order to miniaturize the system in the detection subsystem. As this system uses a heterodyne detection system with two very high frequency (140MHz and 140.02 MHz), the design need to be robust and precise to prevent any high increase in frequency interference and baseline noise. Different scenarios have been tested to miniaturize the detection circuit and finally we were able to successfully combine frequency mixer, second stage amplifier and the band pass filter together in one miniaturized board to reduce the

size of the detection channel. A gain adjustable amplifier is designed for this miniaturized detection circuit to provide more freedom in the dynamic range of the system. In the current prototype the gains for all 14 channels have been set to 55db. Besides that, a custom-made 20kHz band pass filter has been designed to replace the expensive commercial band-pass filter with similar performance in terms of baseline noise and filtering quality.

4.3.2.3. PMT Control with DAC

In the third gen US-guided DOT I described the use of the FPGA based data acquisition board. The miniaturized DAQ can accommodate up to 16 detection channels with two 8 channel A/D chip. THE FPGA passes the converted digital signals to a laptop computer through USB port. Besides data acquisition, this board is responsible for controlling the optical switches sequence. In the new modification on the FPGA based data acquisition board, a port is dedicated to control the sensitivity of the photon multiplier tubes.

4.3.3. Light Delivery and Probe Design

The system has two optical switches which sequentially multiplex the light of 4 laser diodes to 9 source fibers. These fibers then deliver the light into 9 source positions on our hand-held probe. Both optical switches are controlled by the DAQ board and are synchronized with the data acquisition. This light is then shined into tissue and the detected signals in the reflection geometry was collected at 14 detection location on our probe. The detected light at each detection position is then passed to the 14 parallel detection channels.

The ultrasound probe was located in the center of the probe to localize the lesion. In order to use PMT detectors in their maximum dynamic range and prevent the saturation, the very short

source- detector distances have been avoided in the system. The 9 sources are located in one side of the probe and the 14 detectors are located on the other half of the probe. Fig. 4.3 shows the distribution of source and detectors in the combined probe.

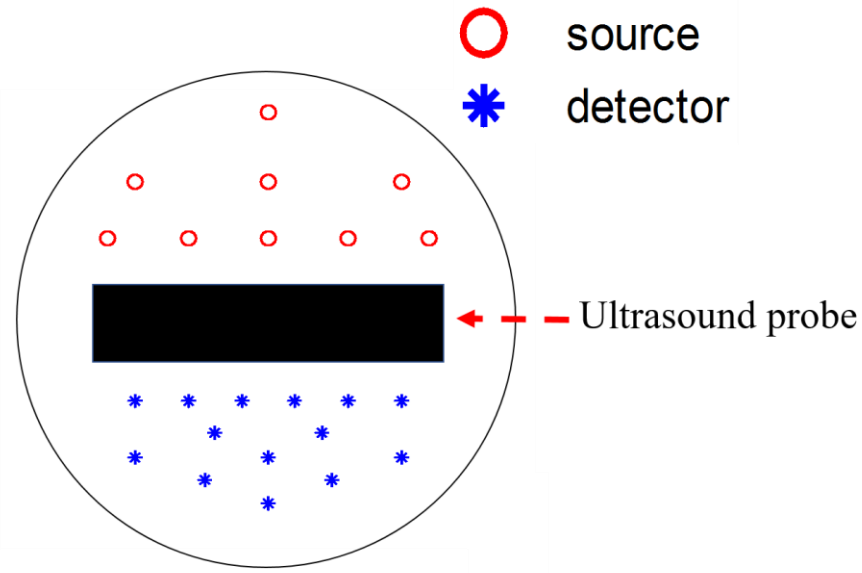

Figure 4.3. Combined diffuse optical tomography and ultrasound probe

4.3.4. Software Improvement

Improvements in robustness and user-friendliness of the software for diffuse optical tomography is one of the important steps to move this technology toward wide use in clinical setting. Our recent progress on reducing user interaction via automated calibration, outlier removal, data selection and lesion boundary detection showed significant improvement in robustness and user-friendliness of the ultrasound-guided DOT. To move this technique one step closer to wide use in the clinical setting, the presented prototype benefits from a graphical user interface with built-in automated data selection, outlier removal, lesion boundary detection from ultrasound image and image reconstruction.

4.4. Phantom Experiments

Multiple phantom experiments have been designed to evaluate the performance the system. In the first sets of experiments, the sensitivity of the system to differentiating high contrast and low contrast phantoms has been tested. Two sets of solid phantoms with absorption of 0.12 and 0.23 cm-1 and same scattering coefficient set at 7-8 cm-1 has been used. To evaluate the sensitivity of the system to different size of phantoms, the system has been tested with three different size (radius of 0.5, 1 and 1.5 cm) of each high contrast and low contrast phantoms. The phantoms were placed in intralipid solution with absorption of 0.02cm-1 and scattering of 7-8 cm-1. The Phantoms have been tested at different depths and below table shows the maximum reconstructed absorption for each of them.

Table 4.1. Maximum reconstructed absorption map for high contrast and low contrast phantoms.

phantom	radius	absorption
SHC	0.5 cm	0.23 cm-1
SLC	0.5 cm	0.11 cm-1
MHC	1 cm	0.23 cm-1
MLC	1 cm	0.11 cm-1
LHC	1.5 cm	0.23 cm-1
LLC	1.5 cm	0.11 cm-1

Table 4.2. Maximum reconstructed absorption map for high contrast and low contrast phantoms.

phantom center depth	SHC	SLC	MHC	MLC	LHC	LLC
1 cm	0.146	0.098				
1.5 cm	0.214	0.111	0.152	0.08		
2 cm	0.246	0.083	0.206	0.077	0.148	0.08
2.5 cm	0.157	0.059	0.253	0.098	0.197	0.079
3 cm	0.091	0.052	0.227	0.084	0.25	0.09
3.5 cm	0.077	0.049	0.208	0.078	0.211	0.097

Figure 4.4 shows the stability of the system over time. The experiments have been repeated for 5 days and the results shows strong stability in the reconstructed absorption over time. The small fluctuation of the reconstructed absorption value is related to the experimental errors, including minor error in adjusting the phantom at exact depth of 2 cm.

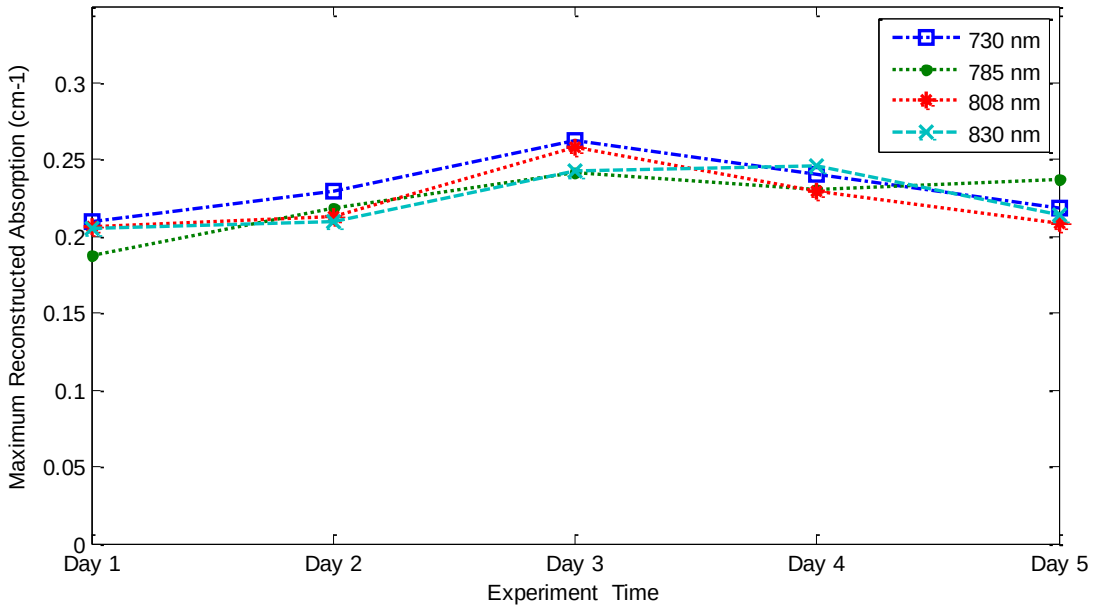

Figure 4.4. Maximum reconstructed absorption for small high contrast phantom at depth of 2cm on different dates. The reconstructed values at 730,785, 808 and 830nm are presented. The green dashed line represents the actual absorption of the phantom.

For later phantom experiment, as Instrumentation Laboratory provides standard Hb solution with the total hemoglobin (tHb) concentration similar to that of human and a known SO2 1, we propose to use this one (Multi-4, Level 2, Instrumentation Laboratory, MA) as the oxy-Hb sample. The Multi-4, Level 2 product specification provided by Instrumentation Laboratory is tHb=139 g/L, with HbO2 percentage equal to about 97%.

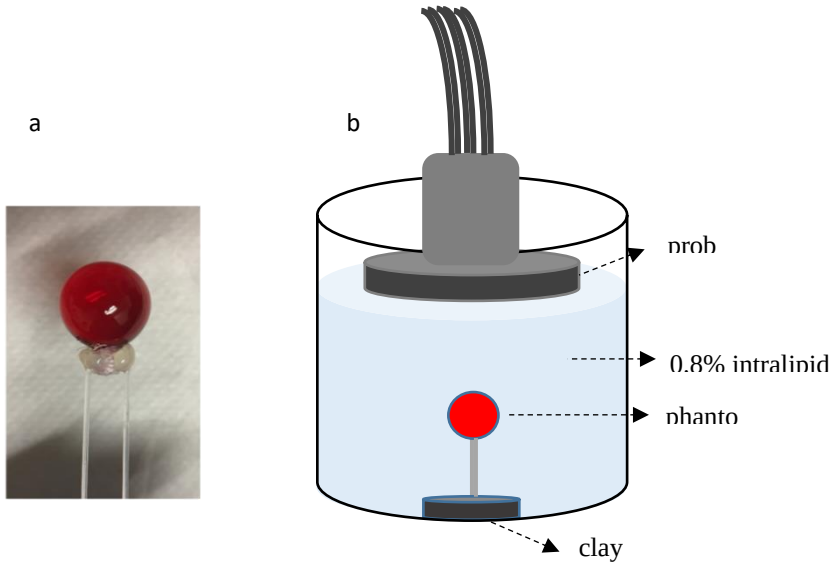

Figure 4.5. (a) Glass ball (0.9 cm radius) filled with HbO2 solution and connected to holding fibers. (b) Sketch of the testing experimental setup

Next, to evaluate the performance of the system in differentiating oxygenated and deoxygenated hemoglobin, the experiment was designed using a hollow glass bulb filled with oxygenated and deoxygenated hemoglobin.

The de-oxygenated hemoglobin (Hb) solution is prepared by adding Na2S2O4 solution into the diluted oxygenated hemoglobin (HbO2). 0.05 g Na2S2O4 is solved in 0.5 mL PBS solution (with 10 µL mixed solution corresponding to 1 mg Na2S2O4). We then add the Na2S2O4 solution into 3.5 mL HbO2 solution to prepare Hb solution. Solution preparation and mixing were operated on top of the dry ice to keep the temperature at around 0 °C and slow down the speed of de-oxygenated Hb reacting with O2. After sealing the glass ball, we incubated it at around 37 °C for 6 min for the Na2S2O4 to work. We calibrated de-oxygenating process with a standard UV-

Vis spectrometer (Varian Cary®, Agilent, US). For each ball and Hb solution, the DOT imaging procedure was donein less than 10 minutes.

The images were reconstructed from measured data and the maximum reconstructed μa were compared with the calibrated values with the spectrometer. We used the max reconstructed μa to compute SO2. We analyzed the DOT measured SO2 of hemoglobin target at different calibrated SO2 (~5-10% and ~97%).

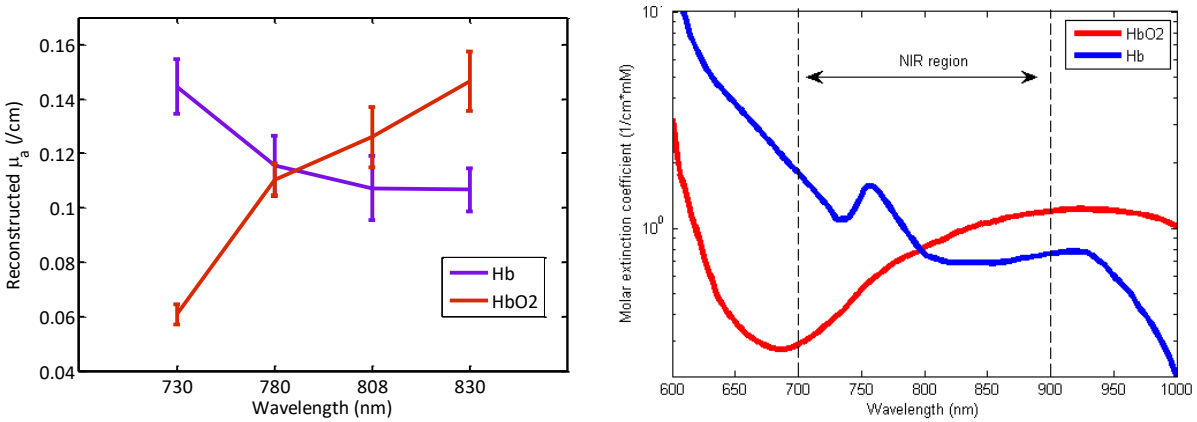

Figure 4.6. Oxygenated and deoxygenated hemoglobin spectrum; a) reconstructed absorption based on 4 wavelength data with the DOT system. b) measured with spectrometer.

To evaluate the performance of the system in terms of sensitivity to oxygenated and deoxygenated hemoglobin, 5 samples of oxygenated hemoglobin and 5 samples of deoxygenated hemoglobin has been prepared separately in different dates and each sample was measured with the spectrometer and then imaged with the ultrasound-guided DOT system. Table 4 demonstrates the calibrated SO2 level for all 10 samples (5 oxygenated, 5 deoxygenated) with spectrometer along with reconstructed SO2 level by using the ultrasound guided DOT system.

Table 4.4. Reconstructed oxygen saturation of 100% oxygenated oxyhemoglobin and 0% deoxygenated hemoglobin calculated with spectrometer as gold standard and DOT system for 5 different samples.

	HBO2		HB	
	Spectrometer	DOT system	Spectrometer	DOT system
SAMPLE 1	97.8%	100%	6.6%	7.0%
SAMPLE 2	97.5%	100%	5.3%	4.7%
SAMPLE 3	97.4%	98.2%	13.4%	5.9%
SAMPLE 4	96.7%	100%	6.0%	1.4%
SAMPLE 5	97.3%	94.9%	4.3%	22.0%

It can be seen that the DOT system is following the spectrometer results very closely with a slight variation. Figure 4.7 shows the comparison of these 5 oxygenated and deoxygenated samples calibrated value with the spectrometer and calculated value with DOT system.

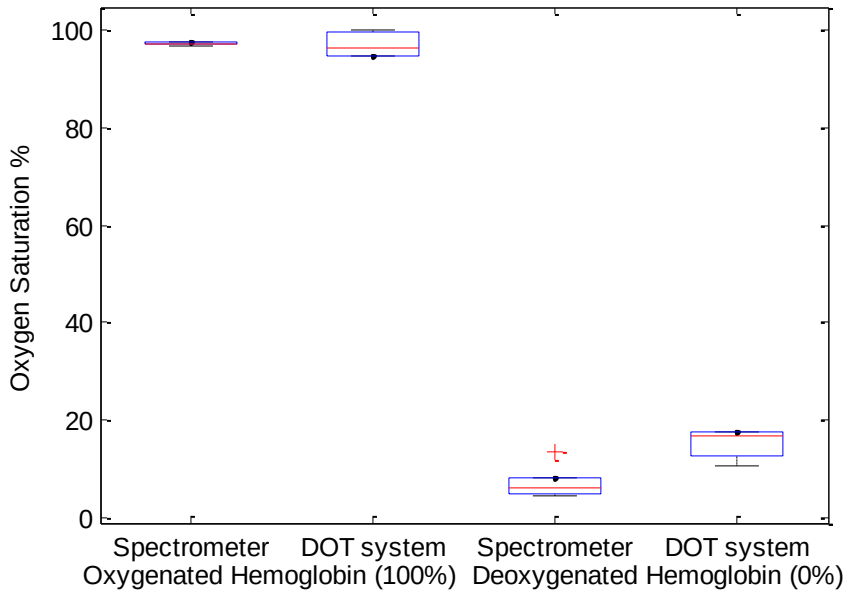

Figure 4.7. Oxygenated and deoxygenated hemoglobin calibrated with spectrometer and measured with DOT system

4.5. Finite element calibration

In order to improve the accuracy of the reconstructed absorption and total hemoglobin concentrations, and reduce the sensitivity of the reconstructed value for different depth and size of the lesion, a finite element model of the breast has been developed in COMSOL Multiphysics (COSMOL Inc, Burlington, MA 01803). The model mimic the breast tissue in ultrasound guided imaging technique as a 10cm cylinder with background optical properties of μa =0.02 cm-1 and μs'=7cm-1 similar to the average normal breast. The model includes a spherical lesion with different sizes and depth to mimic the lesion inside the breast. Figure 10 shows the finite element model of the breast which has been used in this study.

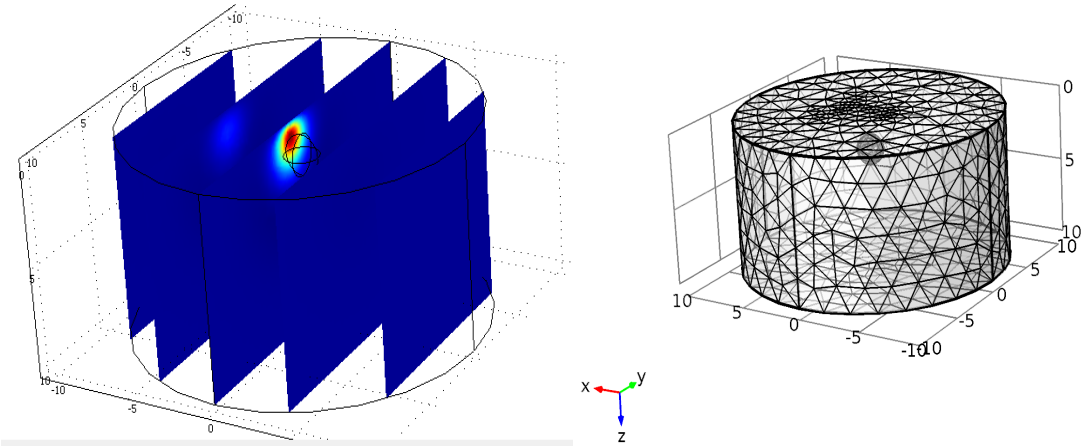

Figure 4.8. Finite element based cylindrical model of breast using COMSOL.

Since the ultrasound image provides the approximate depth and size of the lesions, we decided to use this information in a finite element model to further calibrate our reconstructed absorption maps. The model has been used to simulate the forward data for multiple lesions with different sizes at different depth.

Using this model, we have reconstructed multiple lesions with different optical properties and size at different depths. By comparing the average of maximum reconstructed absorption of each lesion and average of the actual absorption of the lesions, a generalized calibration factor has been calculated for each lesion size and depth. Then by using the depth and size information from the ultrasound images we were able to calibrate the reconstructed absorption map for each lesion. Table 5 shows the maximum reconstructed absorption by using the forward data provided by finite element model. In order to decouple the effect of different absorption on the compensation factors, for each radius of lesion at each depth, a range of absorption starting at 0.08 cm-1 up to 0.24 cm-1 have been simulated.

Table 4.5. Maximum reconstructed absorption for different lesions with absorption ranging from 0.08-0.24 cm-1 at different depths.

Lesion radius: 0.5 cm

Depth\mua	0.08 cm-1	0.12 cm-1	0.16 cm-1	0.20 cm-1	0.24 cm-1
1cm	0.0554	0.0837	0.1093	0.1324	0.1532
1.5cm	0.0711	0.1105	0.1474	0.1817	0.2133
2cm	0.0772	0.1209	0.1614	0.1988	0.2333
2.5cm	0.0622	0.096	0.1266	0.1544	0.1796
3cm	0.0373	0.0559	0.0729	0.0881	0.1016
3.5 cm	0.0337	0.0537	0.0719	0.0884	0.1034

Lesion radius: 1 cm

Depth\mua	0.08 cm-1	0.12 cm-1	0.16 cm-1	0.20 cm-1	0.24 cm-1
1.5cm	0.0754	0.1116	0.1395	0.1607	0.177
2cm	0.0958	0.1443	0.183	0.2138	0.2385
2.5cm	0.0921	0.1355	0.1703	0.1983	0.2211
3cm	0.0845	0.1218	0.1513	0.1751	0.1947
3.5cm	0.0884	0.1237	0.1514	0.1736	0.1917

Lesion radius: 1.5 cm

Depth\mua	0.08 cm-1	0.12 cm-1	0.16 cm-1	0.20 cm-1	0.24 cm-1
2cm	0.081	0.113	0.1331	0.1459	0.1544
2.5cm	0.0859	0.1219	0.1476	0.1662	0.1802
3cm	0.1036	0.1482	0.1806	0.2048	0.2234
3.5cm	0.095	0.1342	0.1631	0.1851	0.2023

By using each reconstructed value, and comparing it to the real absorption in the model, one calibration factor has been extracted. To eliminate the sensitivity of the compensation factor to absorption of the lesion, the calibration factors was averaged over different optical absorptions. As a result, one number was achieved as the calibration factor for each depth and size of the lesion.

Table 4.6. Calculated calibration factor for different size and depth of the lesion

	Lesion Radius		
Lesion Depth	**0.5 cm**	**1 cm**	**1.5 cm**
1cm	1.4981		
1.5cm	1.1050	1.2045	
2cm	1.0106	0.9139	1.2751
2.5cm	1.2928	0.9788	1.1399
3cm	2.2485	1.0998	0.9296
3.5cm	2.2786	1.0977	1.0260

The maximum reconstructed absorption of the high contrast and low contrast balls presented in the section 3, has been calibrated using this calibrations factors. The results of the calibrated maximum reconstructed absorption have been presented in table 4.7.

Table 7. maximum reconstructed absorption for different size of high contrast and low contrast phantoms at different depths after calibration with finite element model.

phantom center depth	SHC	SLC	MHC	MLC	LHC	LLC
1 cm	0.178	0.135				
1.5 cm	0.246	0.125	0.201	0.117		
2 cm	0.332	0.139	0.205	0.072	0.136	0.088
2.5 cm	0.221	0.133	0.285	0.087	0.175	0.087
3 cm	0.277	0.108	0.293	0.139	0.229	0.112
3.5 cm	0.233	0.107	0.205	0.144	0.266	0.143

Figure 4.9. compares the average accuracy (%) of the maximum reconstructed absorption for different solid high contrast and low contrast phantoms before and after finite element calibration. The results show an increase in the average accuracy for different phantom sizes and contrasts.

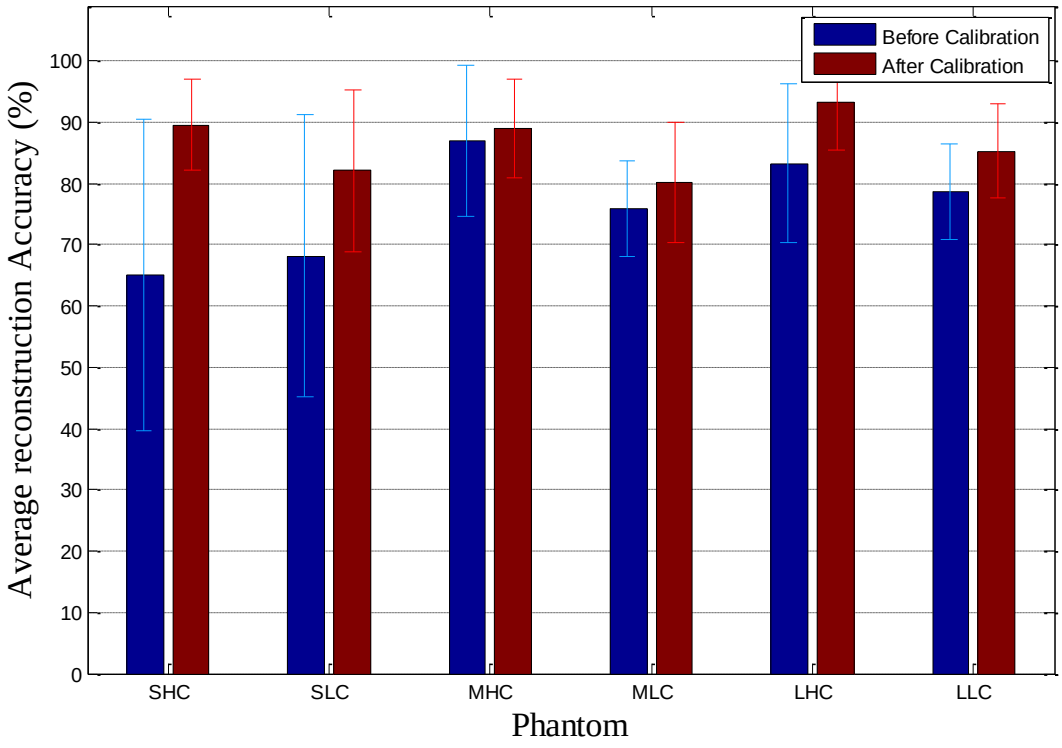

Figure 4.9. Maximum reconstruction accuracy (%) for different phantoms before and after finite element calibration

4.6. Summary

In summary, fourth generation of the DOT system has been presented in this chapter. This generation of the system benefits from several improvements in terms of hardware and software which make it more robust to be used in clinical setting. Besides that, we have worked alongside a professional design company to improve the mechanical design and stability of the fourth generation DOT system.

The system was evaluated by intense phantom experiments and the results have been presented and discussed here. Moreover, the new calibration method has been presented based on the depth and size information of lesion acquired from the finite element simulation. This calibration method uses readily provided information by ultrasound image in terms of depth and size of the lesion and calibrate the reconstructed absorption based on that.

The results presented in this chapter are either published or under publication in multiple journal and conference papers as listed in the reference [21,22].

References

[1] American Cancer Society "Cancer Facts & Figures 2016," Cancer.org. (2016).

[2] Breast cancer organization "U.S. Breast Cancer Statistics 2017, " (http://www.breastcancer.org) (2017).

[3] Zheng, B., A. B. Hollingsworth, M. Y. Tan, R. G. Stough, and H. Liu. "Abstract P4-02-06: Improving efficacy of applying breast MRI to detect mammography-occult breast cancer." (2016): P4-02.

[4] Berg, Wendie A., Andriy I. Bandos, Ellen B. Mendelson, Daniel Lehrer, Roberta A. Jong, and Etta D. Pisano. "Ultrasound as the primary screening test for breast cancer: analysis from ACRIN 6666." *JNCI: Journal of the National Cancer Institute* 108, no. 4 (2016).

[5] Smith, Ian C., Steven D. Heys, Andrew W. Hutcheon, Iain D. Miller, Simon Payne, Fiona J. Gilbert, Antoinne K. Ah-See et al. "Neoadjuvant chemotherapy in breast cancer: significantly enhanced response with docetaxel." *Journal of Clinical Oncology* 20, no. 6 (2002): 1456-1466.

[6] Xu, Chen, Hamed Vavadi, Alex Merkulov, Hai Li, Mohsen Erfanzadeh, Atahar Mostafa, Yanping Gong, Hassan Salehi, Susan Tannenbaum, and Quing Zhu. "Ultrasound-guided diffuse optical tomography for predicting and monitoring neoadjuvant chemotherapy of breast cancers: recent progress." *Ultrasonic imaging* 38, no. 1 (2016): 5-18.

[7] Loo, Claudette E., Marieke E. Straver, Sjoerd Rodenhuis, Sara H. Muller, Jelle Wesseling, Marie-Jeanne TFD Vrancken Peeters, and Kenneth GA Gilhuijs. "Magnetic resonance imaging response monitoring of breast cancer during neoadjuvant chemotherapy: relevance of breast cancer subtype." *Journal of Clinical Oncology* 29, no. 6 (2011): 660-666.

[8] Xu, Chen, Hamed Vavadi, Jigi Chen, Mohsen Erfanzadeh, Quangqian Yuan, Yanping Gong, Hassan Salehi, Hai Li, and Quing Zhu. "Toward miniature diffuse optical tomography system for assessing neoadjuvant chemotherapy." In *Biomedical Optics*, pp. BM3A-57. Optical Society of America, 2014.

[9] Larusson, Fridrik, Pamela G. Anderson, Elizabeth Rosenberg, Misha E. Kilmer, Angelo Sassaroli, Sergio Fantini, and Eric L. Miller. "Parametric estimation of 3D tubular structures for diffuse optical tomography." *Biomedical optics express* 4, no. 2 (2013): 271-286.

[10] Durduran, Turgut, Regine Choe, W. B. Baker, and Arjun G. Yodh. "Diffuse optics for tissue monitoring and tomography." *Reports on Progress in Physics* 73, no. 7 (2010): 076701.

[11] Chance, Britton, Shoko Nioka, Jun Zhang, Emily F. Conant, Emily Hwang, Susanne Briest, Susan G. Orel, Mitchell D. Schnall, and Brian J. Czerniecki. "Breast cancer detection based on incremental biochemical and physiological properties of breast cancers: a six-year, two-site Study1." *Academic radiology* 12, no. 8 (2005): 925-933.

[12] Quarto, Giovanna, Lorenzo Spinelli, Antonio Pifferi, Alessandro Torricelli, Rinaldo Cubeddu, Francesca Abbate, Nicola Balestreri, Simona Menna, Enrico Cassano, and Paola Taroni. "Estimate of tissue composition in malignant and benign breast lesions by time-domain optical mammography." *Biomedical optics express* 5, no. 10 (2014): 3684-3698.

[13] Zhu, Quing, Andrew Ricci Jr, Poornima Hegde, Mark Kane, Edward Cronin, Alex Merkulov, Yan Xu, Behnoosh Tavakoli, and Susan Tannenbaum. "Assessment of functional differences in malignant and benign breast lesions and improvement of diagnostic accuracy by using US-guided diffuse optical tomography in conjunction with conventional US." *Radiology* 280, no. 2 (2016): 387-397.

[14] Vavadi, Hamed, Chen Xu, Atahar Mostafa, and Quing Zhu. "Automated Data Selection Method for Diffuse Optical Tomography to Improve the Robustness of Breast Cancer Detection." In *Clinical and Translational Biophotonics*, pp. JM3A-2. Optical Society of America, 2016.

[15] Vavadi, Hamed, Chen Xu, and Quing Zhu. "The effect and correction of reference heterogeneity in diffuse optical tomography." In *SPIE BiOS*, pp. 93192D-93192D. International Society for Optics and Photonics, 2015.

[16] Vavadi, Hamed, and Quing Zhu. "Automated data selection method to improve robustness of diffuse optical tomography for breast cancer imaging." *Biomedical optics express* 7, no. 10 (2016): 4007-4020.

[17] Xu, Chen, Hai Li, Guangqian Yuan, Hamed Vavadi, and Quing Zhu. "Development of a robust and fast calibration procedure for diffuse optical tomography." In *SPIE BiOS*, pp. 93192E-93192E. International Society for Optics and Photonics, 2015.

[18] Mostafa, Atahar, Hamed Vavadi, and Quing Zhu. "Extraction of tumor features from ultrasound images for diffused optical tomography reconstruction." In *Optical Tomography and Spectroscopy*, pp. JTu3A-14. Optical Society of America, 2016.

[19] Althobaiti, Murad, Hamed Vavadi, and Quing Zhu. "Diffuse optical tomography reconstruction method using ultrasound images as prior for regularization matrix." *Journal of Biomedical Optics* 22, no. 2 (2017): 026002-026002.

[20] Althobaiti, Murad, and Quing Zhu. "Evaluation of a Dual-Mesh for Reconstruction of Diffuse Optical Tomography using NIRFAST." In *Cancer Imaging and Therapy*, pp. JTu3A-9. Optical Society of America, 2016.

[21] Hamed Vavadi, Atahar Mostafa, jinglong Li, Feifei Zhu, Shihab Uddin, Chen Xu, and Quing Zhu, "Development and miniaturization of a robust Ultrasound guided diffuse optical tomography system for breast imaging*", Journal of Biomedical Optics (submit).*

[22] Vavadi, Hamed, Atahar Mostafa, Jinglong Li, Feifei Zhou, Shihab Uddin, Chen Xu, and Quing Zhu. "Preliminary results of miniaturized and robust ultrasound guided diffuse optical tomography system for breast cancer detection." In *Optical Tomography and Spectroscopy of Tissue XII*, vol. 10059, p. 100590F. International Society for Optics and Photonics, 2017.

5. Reference Smoothing

5.1. Abstract

Near infrared (NIR) diffuse optical tomography has demonstrated great potential in the initial diagnosis of tumor and in the assessment of tumor vasculature response to neoadjuvant chemotherapy. To reconstruct the absorption map of a breast lesion, perturbation is needed which is the normalized difference between the measurements of lesion-side breast and contralateral reference breast. However, the heterogeneity in the reference breast can produce unwanted

perturbation which will result in distortion of the reconstructed target absorption map. This cahpter introduces a filtering method to overcome the reference heterogeneity. This method corrects affected source-detector measurements obtained from the reference side by using averages of unaffected measurements. As a result, the filtered perturbation has decreased the effect of heterogeneity on the reconstructed absorption maps. To evaluate the performance of this filtering method, we have compared the reconstructed results with and without the filtering algorithm using simulated heterogeneous reference with heterogeneous absorbers ranging from 0.05 to 0.20 cm-1 and heterogeneous scatters ranging from 10 to 20cm-1. The results show that the algorithm can improve the maximum reconstructed target value up to 99% of the value with homogeneous reference. In the worst case of high absorption heterogeneity in reference breast, the maximum reconstructed value was around 30.85% of the true absorption without filtering correction and was improved to 60.4% of the true absorption value, which is 95% of the reconstructed value when using the homogeneous reference.

5.2. Introduction

Neoadjuvant chemotherapy (NAC) is a frequently used treatment to downstage the disease and prepares patients with locally advanced breast cancers for surgery [1]. Different modalities have been used to differentiate between patients who respond and who don't respond to NAC; while a method which can provide accurate results at early stages of treatment is still under study. Physical examination, ultrasound and mammography, conventionally are used to monitor the response of patients to NAC and shown moderate results in the assessment of tumor response. In contrast to

conventional methods dynamic contrast enhanced MRI shows the ability in early identification of nonresponders. This method can predict the presence of residual tumor after completion of each NAC which could decrease the patient additional exposure to ineffective and toxic treatments [2]. 18F-fluorodeoxyglucose (18F-FDG) positron emission tomography/computed tomography (PET/CT) have been reported to show good performance in excluding distant metastases prior to neoadjuvant chemotherapy (NAC) treatment [3-5]. Besides these methods, near infrared (NIR) diffuse optical tomography also has demonstrated great potential in assessment of tumor vasculature response to neoadjuvant chemotherapy [3-5]. MRI and PET equipment are not only bulky and expensive, but require the injection of contrast agents. These constraints prevent them from being used repeatedly for monitoring patients during treatment. However, near infra-red (NIR) systems are portable, require no contrast agents, and have lower cost which make them an ideal alternative for repeated use in clinical settings.

Our group has studied the feasibility of using US-guided NIR imaging technique on patients who were undergoing NAC. We assessed them at the pretreatment stage, at the end of every treatment cycle, and before surgery. The system used in our study consists of four wavelength laser diodes with 740, 780, 808, and 830 nm and ten channels detectors. The laser diodes are connected to 4 by 1 switch and 1 by 9 switch. The source fibers and detector fibers are connected to a housing probe with commercial US transducer located in the middle. Patients were scanned in a supine position and multiple sets of ultrasound images and optical measurements with reflection geometry were collected at the lesion location and at a contra-lateral region of the normal breast (reference location). The results showed that the initial tumor Hb content was a strong predictor of final pathologic response. Besides that, the tHb variation during early treatment cycles can be used to predict final pathologic response [4, 5].

Our experiments reveal that using a contralateral reference breast measurement to calculate normalized perturbation could reduce the effect of different tissue properties in different patients [6]. While using normalized perturbation can improve the consistency and reliability of the results between different patients, it is highly dependent on the reference tissue, which is homogeneous ideally. However, in clinical setting the reference tissue itself is not completely homogeneous which can cause inaccuracy in calculating optical properties and tHb of the tumors. This chapter is focused on evaluating the effect of heterogeneous reference breast on the optical properties and shape of tumors.

5.3. Method and Model

In our phantom and clinical experiment procedure, two sets of measurements were collected from lesion breast (lesion or target site) and contralateral normal breast (reference site) to calculate normalized perturbation as shown below:

$$U_{sc}(i) = \frac{A_l(i)exp(\varphi_l(i)) - A_r(i)exp(\varphi_r(i))}{A_r(i)exp(\varphi_r(i))} \quad (1)$$

where $A_l(i)$,$\varphi_l(i)$ were measured amplitude and phase for ith source-detector pair from lesion breast while$A_r(i)$, $\varphi_r(i)$ were measured amplitude and phase for ith source-detector pair from reference breast. Heterogeneity in the reference tissue can affect the reference measurements, which can cause inaccuracy in normalized perturbation. Finite-element based method in COMSOL Multiphysics (COSMOL Inc, Burlington, MA 01803) was used to simulate the effect of heterogeneous reference on the reconstructed NIR image. A 10cm cylinder was modeled as the

scattered medium to mimic the breast tissue with optical properties of μa =0.02 cm-1 and μs'=7cm-1. The ideal reference was homogeneous medium. To model the heterogeneity, a sphere with different optical properties was placed inside the reference model. The position, size and optical properties of heterogeneity were changed to mimic different scenario of heterogeneous reference breasts. Same model was used for the lesion side without the heterogeneous target as shown in Figure 1(a), but with a spherical lesion located at center in depth of 2cm with optical properties of μa =0.2 cm-1 and μs'=7cm-1. The light was induced to the model from 9-point sources on the top of the cylindrical model and the reflected light was collected at 14 different locations on top of the cylinder to mimic the 9source positions and 14 detector channels in the hand-held probe. The fluence distribution inside the medium when one source was on was shown in Figure 1(b).

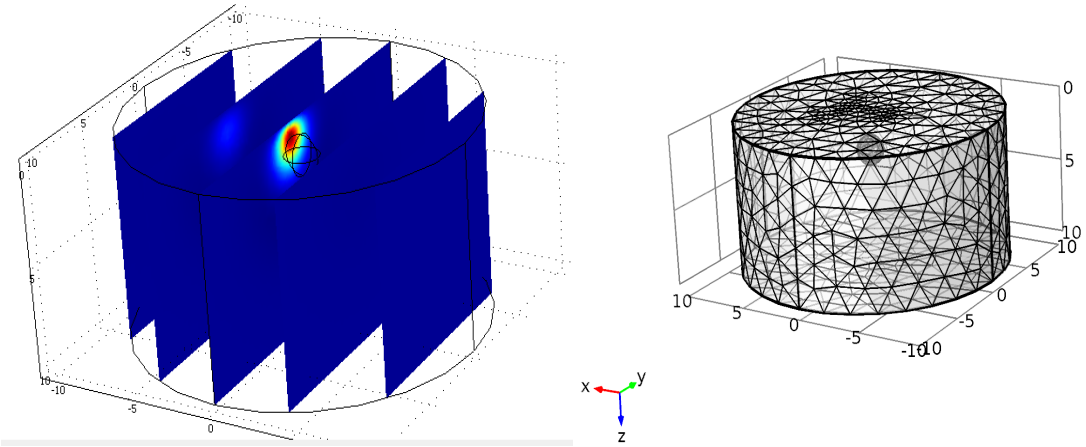

Figure 5.1. Finite element based cylindrical model of breast using COMSOL.

The simulated data at reference side and lesion sides was used to calculate normalized perturbation based on formula (1). Optical properties of lesion inside breast were calculated by using normalized perturbation and solving inverse problem.

The simulated data at reference side and lesion sides was used to calculate normalized perturbation based on formula (1). Optical properties of lesion inside breast were calculated by using normalized perturbation and solving inverse problem.

$$U_{sc} = W \times \delta\mu_a \tag{3}$$

$$[m \times 1] \; = \; [m \times n] \times [n \times 1]$$

To overcome effect of heterogeneity of modeled reference breast, a filtering method was developed. Filtering method was focused on smoothing the reference breast measurements toward homogeneous breast tissue measurements. Two different approaches developed to reduce the effect of heterogeneity. First approach is based on smoothing the normalized perturbation directly while second approach is based on smoothing the heterogeneous reference measurements only.

First approach (Perturbation Correction):

Find positive perturbation for each source detector pairs $U_{sc}(i) => 0$

Calculate the average perturbation around that S-D distance by using other measurement data

$$\left\{ \forall i \in [1, m] \; if \; U_{sc}(i) > 0 \middle| U_{sc}^{*}(i) = \frac{\sum_{j=1}^{k} U_{sc\_R}(j)}{k} \right\} \tag{4}$$

where U_{sc_R} are measurements from SD distance equal to i

Use corrected perturbation to solve the inverse problem and calculate absorption map.

$$U_{sc}^{*} = W \times \delta\mu_a \tag{5}$$

$$[m \times 1] \; = \; [m \times n] \times [n \times 1]$$

Second approach (Reference Smoothing):

Find positive perturbation for each source detector pairs$U_{sc}(i) => 0$

Calculate the average reference measurement for S-Ds with similar distance.

$$\left\{ \forall i \in [1, m] \; if \; U_{sc}(i) > 0 \middle| U_r(i) = \frac{\sum_{j=1}^{k} U_{r\_R}(j)}{k} \right\} \tag{6}$$

where U_{r_R} are measurements from SD distance equal to i

Smoothing reference based on approximated expected value calculated with other pairs in same distance

$$U_{sc}^{*}(i) = \frac{U_l(i) - U_r^{*}(i)}{U_r^{*}(i)} \tag{7}$$

Use smoothed reference to solve the inverse problem and calculate absorption map.

$$U_{sc}^{*} = W \times \delta\mu_a \tag{8}$$

$$[m \times 1] \; = \; [m \times n] \times [n \times 1]$$

5.4. Results

To evaluate the effect of heterogeneity in reference tissue on perturbation and reconstructed image different sets of measurements from different reference and one set of measurement from simulated lesion breast have been used to calculate perturbation and reconstruct the image. For the sake of brevity, we illustrate the result of 3 cases here, but for all scenarios same trend is observed. In first scenario perturbation have been calculated by using homogeneous reference with homogeneous background optical properties of μa =0.02 cm-1 and μs'=7cm-1. In the second scenario perturbation calculated by using heterogeneous reference with small heterogeneous ball with radius of 0.5cm and optical properties of μa =0.02 cm-1 and μs'=7cm-1 in depth of 1 cm. Finally, for third scenario an extreme case of heterogeneity have been considered. In this case absorption coefficient of small ball in second scenario have been increased to μa =0.2 cm-1. Figure 5.2. (a) and (b) shows the normalized perturbation calculated with homogeneous reference while Figure 5.2. (c) and (d) shows the real and imaginary parts of normalized perturbation calculated with heterogeneous reference of second scenario and Figure 5.2 (e) and (f) shows the real and imaginary parts of normalized perturbation calculated with heterogeneous reference of third scenario. As shown in Figure 3, all the calculated perturbations are negative both in real and imaginary parts when using homogeneous reference, while positive perturbation observed when heterogeneous reference from second scenario have been used to calculate normalized perturbations. Last row of figure 5.2 shows that by increasing the absorption heterogeneity in reference tissue, the number and value of positive perturbation have been increased.

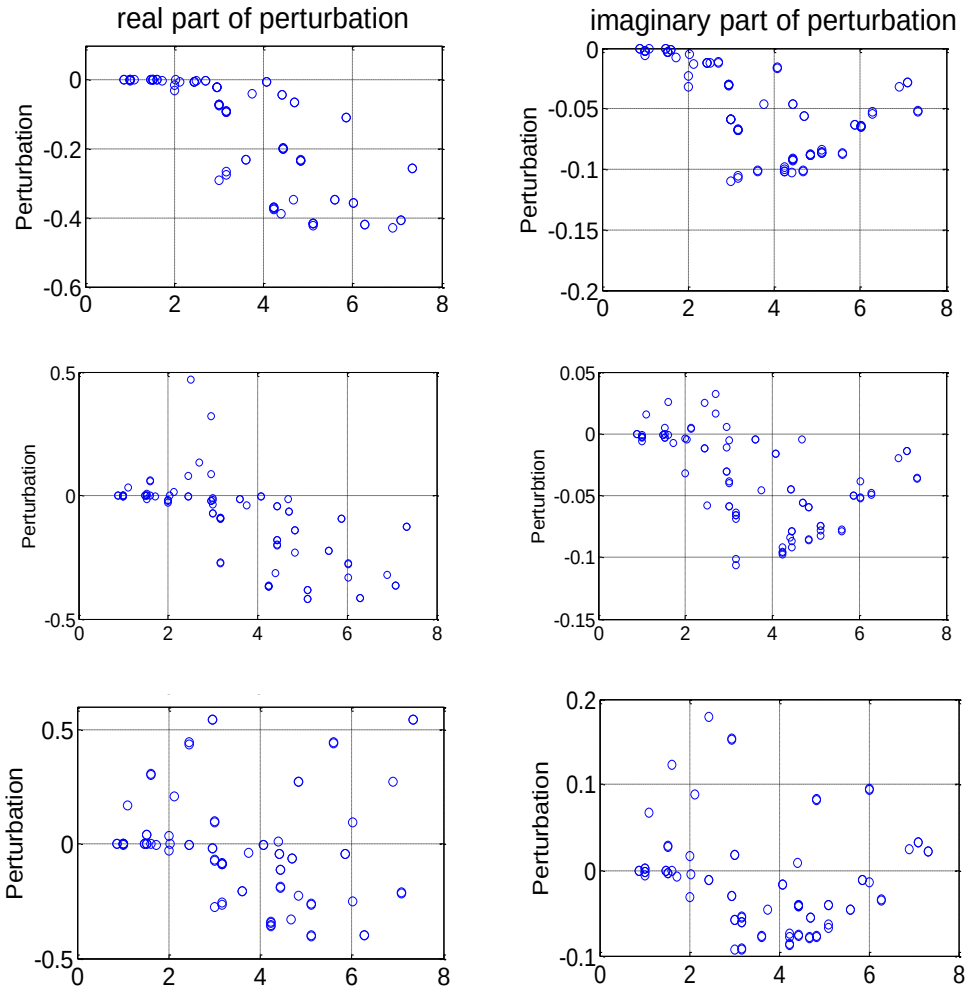

Figure 5.2. Real and imaginary part of normalized perturbation a) & b) homogeneous reference breast model, c) &d) heterogeneous reference breast model in second scenario, e) &f) heterogeneous reference breast model in third scenario.

The Effect of different references on the reconstructed image is illustrated in Figure 5.3. Figure 5.3.a shows reconstructed image with normalized perturbation calculated from homogeneous reference while 5.3.b and 5.3.c show reconstructed image heterogeneous references described in scenario 2 and 3, respectively. Maximum reconstructed value by using homogeneous reference was0.1271 cm-1. By using measurements from modeled reference in second scenario,

maximum reconstructed value was changed to 13.06 cm-1 and with measurements from heterogeneous reference in third scenario, maximum reconstructed value changed to 0.0617 cm-1. It can be seen that by changing the amount of heterogeneity shape and maximum reconstructed value of lesion has changed.

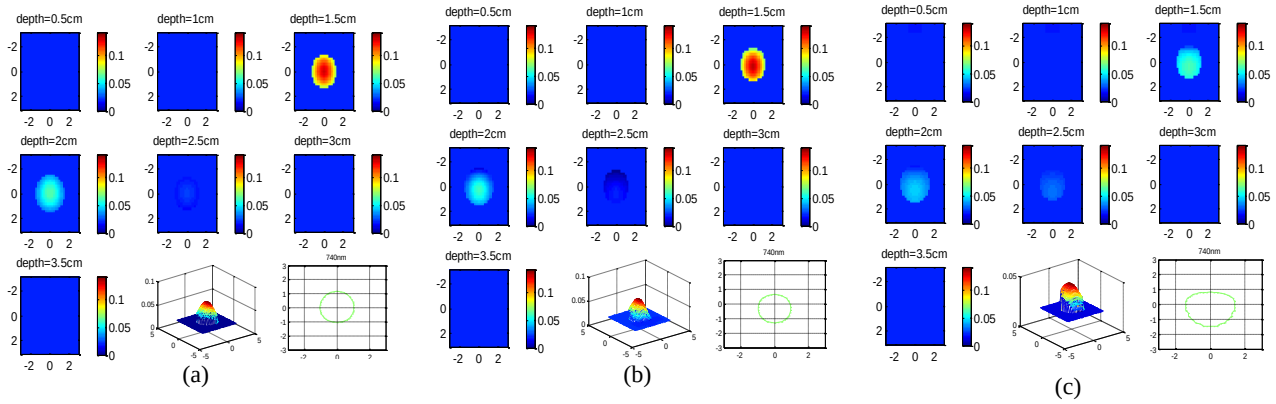

Figure 5. 3. Effect of heterogeneity in the reference breast in the reconstructed image. a) Completely homogeneous reference, b) Low absorption heterogeneity inside the reference, c) High absorption heterogeneity inside the reference

Both perturbation correction and reference smoothing methods have been applied to the different heterogeneous reference. After applying both of these approaches, in all the cases, the reconstructed image was improved toward shape and value reconstructed by using homogeneous reference. The result of both smoothing algorithms on the worst-case scenario with maximum heterogeneity (third scenario) is discussed quantitatively.

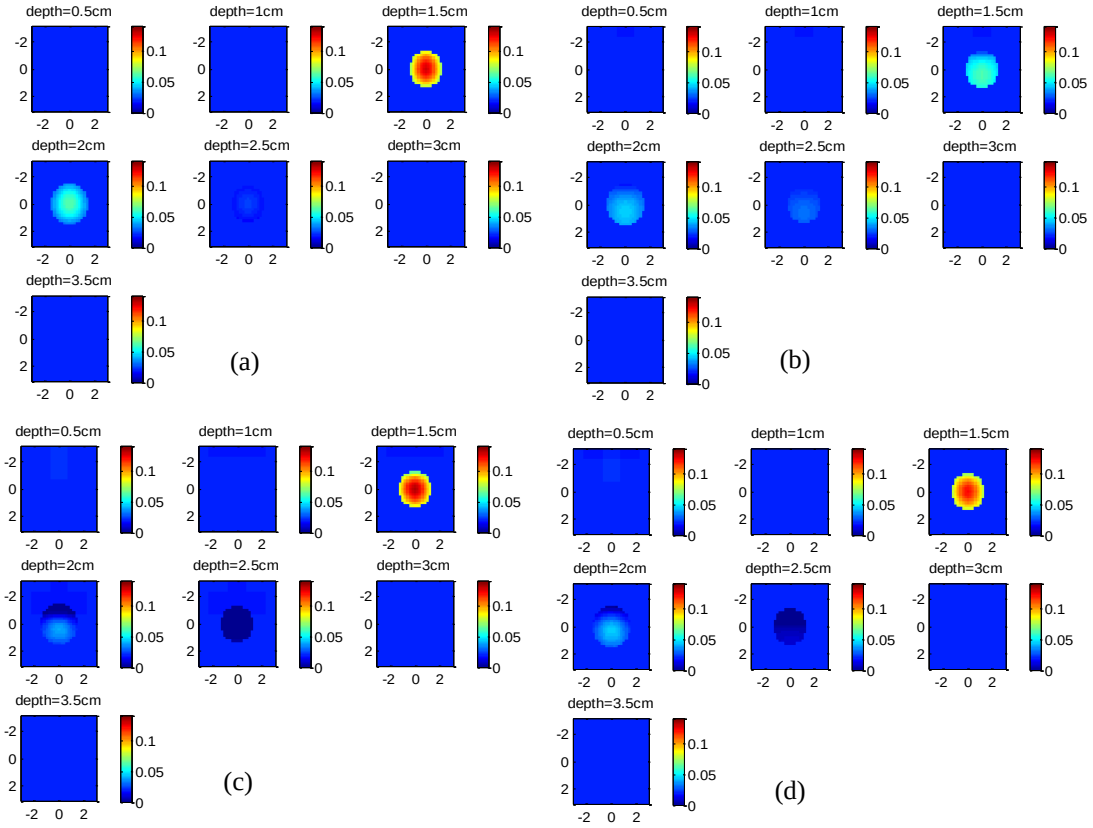

Figure 5.4. Reconstructed image based on a) Completely homogeneous reference, b) Heterogeneous reference before correction, c) Heterogeneous reference after perturbation correction, d) Heterogeneous reference after reference smoothing.

Figure 5.4 shows the reconstructed image with homogeneous reference, heterogeneous reference without correction, heterogeneous reference with perturbation correction and heterogeneous with reference smoothing. As shown in Figure 5.b, the shape and value of lesion by using reference of third scenario differ dramatically from the reconstructed image by using homogeneous reference in Figure 5.4.a. This heterogeneity caused maximum reconstructed value to be less than 48.54% of the maximum reconstructed value with homogeneous reference. By applying our reference smoothing and perturbation correction methods, we were able to improve

it to 95.04% and 104.48% of reconstructed value with homogeneous reference, respectively. Figure 5.c and 5.d shows the reconstructed image with heterogeneous reference of third scenario with perturbation correction and reference smoothing, respectively.

The maximum reconstructed absorption with homogeneous reference, heterogeneous reference of third scenario without correction, heterogeneous reference of third scenario with perturbation correction and heterogeneous reference of third scenario with reference smoothing are shown in table 5.1.

Table5.1. Maximum reconstructed absorption value with homogeneous, heterogeneous and heterogeneous after applying perturbation correction and reference smoothing methods

	True value	Homogeneous reference	Heterogeneous reference	perturbation correction	Reference smoothing
μa	0.2 cm-1	0.1271 cm-1	0.0617 cm-1	0.1328 cm-1	0.1208 cm-1

Although the effect of the heterogeneity inside the reference could not be completely compensated, it could be reduced by applying these two methods. For example, in the case of high heterogeneity inside the reference breast, the maximum reconstructed value shows 51.56% error compared to the reconstructed value using homogeneous reference.

By applying the perturbation correction and reference smoothing methods, this error has been reduced to 4.48% and 4.96%, respectively.

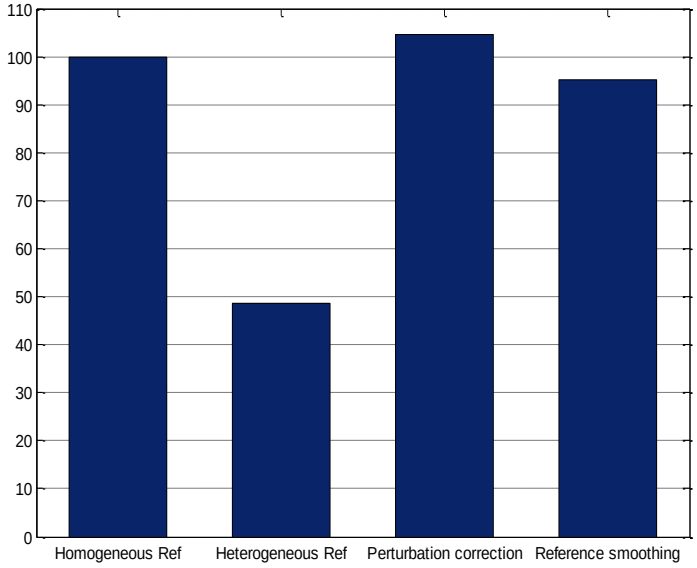

Figure 5.5. Percentage of maximum reconstructed value with completely homogeneous reference (first column), heterogeneous reference (second column), heterogeneous reference after perturbation correction (third column) and heterogeneous reference after reference smoothing (fourth column).

This method has been used in multiple clinical cases with wavelength dependency due to reference heterogeneity and the results have been improved significantly after using the reference smoothing method. Below are the results of one malignant case before and after reference smoothing. The results are showing clear increase in the consistency of the reconstructed image across multiple wavelengths.

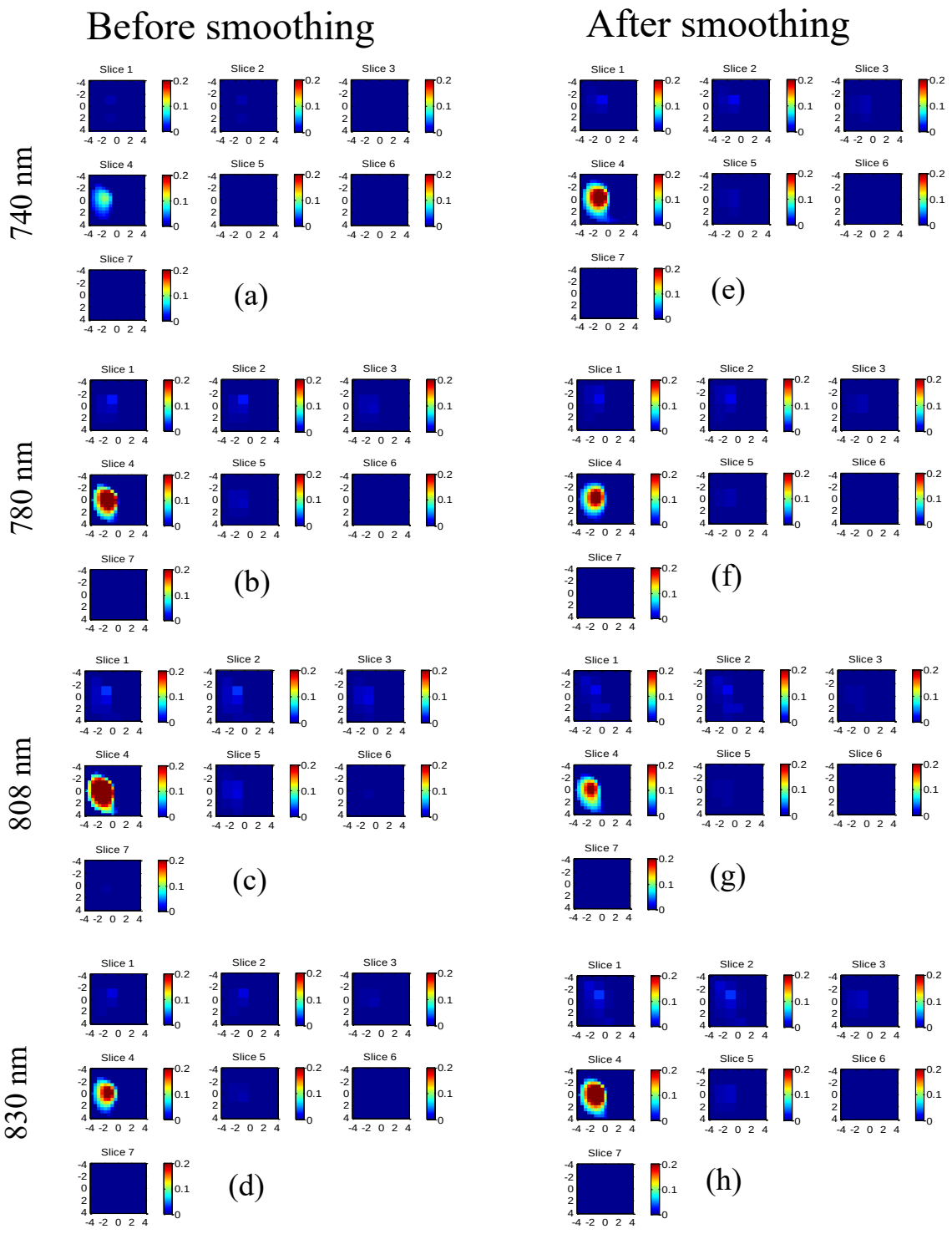

Figure 5.6. Reconstructed image of a malignant case before and after reference smoothing method. The left column represents the results of 740, 780, 808 and 830 nm before reference smoothing (a-d respectively) and right column represents the results of 740, 780, 808 and 830 nm after reference smoothing (e-h respectively)

5.5. Discussion

In this chapter the effect of the heterogeneity inside the reference breast on the perturbation and reconstructed absorption map have been studied. The simulation indicates that by increasing the heterogeneity inside the reference, the number and value of positive points in perturbation increases dramatically. As demonstrated, this change in the perturbation will affect the reconstructed absorption map in terms of maximum value, center and shape of the lesion inside the target breast. The introduced smoothing methods show promising results to reduce the effect of the heterogeneity in the reconstructed image. The application of the method on the clinical results showed promising results in terms of improving the robustness of reconstructed absorption map.

This simulation part of this method has been published in a proceeding paper at SPIE conference and the completed method along with clinical cases will be further completed and submitted separately [7].

References

[1] Rastogi, Priya, Stewart J. Anderson, Harry D. Bear, Charles E. Geyer, Morton S. Kahlenberg, André Robidoux, Richard G. Margolese et al. "Preoperative chemotherapy: updates of national surgical adjuvant breast and bowel project protocols B-18 and B-27." *Journal of Clinical Oncology* 26, no. 5 (2008): 778-785.

[2] Loo, Claudette E., Marieke E. Straver, Sjoerd Rodenhuis, Sara H. Muller, Jelle Wesseling, Marie-Jeanne TFD Vrancken Peeters, and Kenneth GA Gilhuijs. "Magnetic resonance imaging response monitoring of breast cancer during neoadjuvant chemotherapy: relevance of breast cancer subtype." *Journal of Clinical Oncology* 29, no. 6 (2011): 660-666.

[3] Xu, Chen, Hamed Vavadi, Alex Merkulov, Hai Li, Mohsen Erfanzadeh, Atahar Mostafa, Yanping Gong, Hassan Salehi, Susan Tannenbaum, and Quing Zhu. "Ultrasound-guided diffuse optical tomography for predicting and monitoring neoadjuvant chemotherapy of breast cancers: recent progress." *Ultrasonic imaging* 38, no. 1 (2016): 5-18.

[4] Zhu, Quing, Patricia A. DeFusco, Andrew Ricci Jr, Edward B. Cronin, Poornima U. Hegde, Mark Kane, Behnoosh Tavakoli, Yan Xu, Jesse Hart, and Susan H. Tannenbaum. "Breast cancer: assessing response to neoadjuvant chemotherapy by using US-guided near-infrared tomography." *Radiology* 266, no. 2 (2013): 433-442.

[5] Xu, Chen, Hamed Vavadi, Jigi Chen, Mohsen Erfanzadeh, Quangqian Yuan, Yanping Gong, Hassan Salehi, Hai Li, and Quing Zhu. "Toward miniature diffuse optical tomography system for assessing neoadjuvant chemotherapy." In *Biomedical Optics*, pp. BM3A-57. Optical Society of America, 2014.

[6] Zhu, Quing, NanGuang Chen, and Scott H. Kurtzman. "Imaging tumor angiogenesis by use of combined near-infrared diffusive light and ultrasound." *Optics letters* 28, no. 5 (2003): 337-339.

[7] Vavadi, Hamed, Chen Xu, and Quing Zhu. "The effect and correction of reference heterogeneity in diffuse optical tomography." In *SPIE BiOS*, pp. 93192D-93192D. International Society for Optics and Photonics, 2015.

6. Automated Data Pre-Processing

6.1. Abstract

Imaging-guided near infrared diffuse optical tomography (DOT) has demonstrated a great potential as an adjunct modality for differentiation of malignant and benign breast lesions and for monitoring treatment response of breast cancers. However, diffused light measurements are sensitive to artifacts caused by outliers and errors in measurements due to probe-tissue coupling, patient and probe motions, and tissue heterogeneity. In general, pre-processing of the measurements is needed by experienced users to manually remove these outliers and therefore

reduce imaging artifacts. An automated method of outlier removal, data selection, and filtering for diffuse optical tomography is introduced in this chapter. This method consists of multiple steps to first combine several datasets collected from the same patient at contralateral normal breast and form a single robust reference dataset using statistical tests and linear fitting of the measurements. The second step improves the perturbation measurements by filtering out outliers from the lesion site measurements using model based analysis. The results of 20 malignant and benign cases show similar performance between manual data processing and automated processing and improvement in tissue characterization of malignant to benign ratio by about 27%.

6.2. Introduction

According to the American Cancer Society, breast cancer is estimated to be the most common type of cancer among women with more than 246000 new cases and approximately 40,000 deaths projected in the United States in 2016 [1]. Mammography, ultrasound (US) and magnetic resonance imaging (MRI), are widely used to detect and diagnose breast lesions. Mammography is the most clinically used imaging modality for breast cancer screening, but it suffers from significant limitations such as relatively low sensitivity in early cancer diagnosis, reduced sensitivity in women with dense breasts, and low specificity that results in a large number of unnecessary biopsies [2]. A new study demonstrates comparable results for breast cancer detection rate between US and mammography. However, US still lacks sensitivity and specificity with a large number of false positive cases reported [3]. Although MRI has a higher sensitivity in breast

cancer detection, the low cancer detection yields in the general screening population and high costs of MRI prohibit its applicability as a screening tool [2].

Diffuse optical tomography (DOT) is a noninvasive functional imaging modality that utilizes near-infrared (NIR) light to probe tissue optical properties. Minimal light absorption in the NIR wavelength range allows for several centimeters of light penetration in soft tissue such as breast and brain and facilitates probing lesions deep in the tissue. Image reconstruction is performed using reflected or transmitted light at the tissue surface [4-7]. NIR diffuse optical tomography has emerged as a promising modality to detect and monitor functional changes related to blood flow and tumor angiogenesis. Using multi-wavelength data acquisition, it is possible to quantify tissue characteristics such as oxygenated, deoxygenated, and total hemoglobin (HbO2, HbR, and HbT) concentrations as well as hemoglobin oxygen saturation (SO2) and lipid and water concentrations [8,9]. Clinical studies of female breasts have demonstrated higher HbT in the malignant lesions compared to both healthy tissue and benign lesions [8,10,12,14,15].

High sensitivity and cost effectiveness of DOT make it an ideal alternative for conventional breast imaging modalities. Currently DOT is not widely used in clinical settings mainly due to the low spatial resolution and lesion location uncertainty caused by intense light scattering in soft tissue. However, DOT guided by mammography, US, and MRI [10-13] have overcome lesion location uncertainty and improved the light quantification accuracy, and have been demonstrated as promising complementary methods to the existing imaging modalities. Ultrasound-guided DOT system and technique has been developed by our group and clinical results have demonstrated its potential in differentiating malignant and benign breast lesions and reducing the need for unnecessary benign biopsies [10,15]. In this approach, DOT is used to characterize the US detected lesions and to improve the diagnostic accuracy of US by providing complementary optical

contrast. In a recent study, we have demonstrated that when US detection and diagnosis used together with optical hemoglobin contrast, the sensitivity of breast cancer detection and diagnosis has researched 96.6-100% [10].

The path toward commercialization of imaging guided DOT techniques depends upon the improvement of robustness and user-friendliness of this technique in hardware and software. Several groups have investigated various approaches to improve the robustness of the hardware, system calibration, data selection, target localization, and image reconstruction [16-20]. Reducing user interaction via automated processing of calibration and data selection is an important step toward clinical applicability of DOT.

In US-guided DOT or other hand-held DOT operation, a hand-held probe is placed on top of a patient's breast while the patient is in a supine position [21]. Movements of patient or operator's hand could cause a bad coupling between the light guides and the breast which may result in some outliers in measurements. In other imaging guided DOT approaches, the probe may be fixed, however, the bad coupling between tissue and light guides can occur which may result in outlier measurements. Additionally, tissue heterogeneity can cause measurement errors at some source-detector pairs. Recovered background and lesion optical properties highly depend on the boundary measurements of light propagating through the tissue underneath and any errors in these measurements could cause inaccuracy in fitted background and reconstructed lesion optical properties [22,23]. In this study, we introduce an automated outlier removal, data selection, and perturbation filtering method for imaging-guided DOT to improve its robustness in breast imaging. This method utilizes multiple sets of reference measurements acquired at a normal contralateral breast in one imaging session to produce a robust set of reference measurements. Then, the lesion measurement set is subtracted and scaled by this robust reference to form the normalized

perturbation of the scattered field. Next, the perturbation was filtered for outliers and measurement errors based on analysis from simulations. Finally, the filtered perturbation is used for reconstruction of absorption maps and total hemoglobin distributions to characterize malignant and benign breast masses. The method of combining multiple measurements to perform statistical test for noise and outlier removal and saturation data rejection, can be applied to other methods of imaging-guided DOT, such as mammogram or MRI guided diffuse optical tomography with some modifications.

6.3. Dataset and System

6.3.1. Patients

US-guided DOT is used to characterize 10 malignant and 10 benign lesions of 20 patients. The study protocol was approved by the local internal review board (IRB). Signed informed consent was obtained from all patients and the study was compliant with the Health Insurance Portability and Accountability Act. For each patient, US images and optical measurements were simultaneously acquired before biopsy at the lesion site and at the normal contralateral breast of the same quadrant as the lesion which is used as reference. Mammograms, US images before the NIR scan were reviewed by attending radiologists and all contralateral measurements were taken at normal areas based on the available information [10].

6.3.2. System

The DOT system used in this study consisted of four laser diodes of wavelengths 740, 780, 808 and 830 nm. The outputs of the diodes were multiplexed by two optical switches to nine positions and were then coupled to a hand-held probe through optical fibers. Ten optical light guides coupled diffused light reflected from tissue to 10 photomultiplier tubes. The outputs of the laser diodes were amplitude modulated at 140 MHz and the detector outputs were demodulated to 20 kHz. The entire data acquisition took approximately 3 to 4 seconds, which was fast enough to repeat several times during one imaging session and obtain multiple measurements from each patient at the lesion site and the contralateral normal breast at the same quadrant as the lesion, referenced as reference measurement in the following text. For each patient, we typically collect 4 to 6 sets of measurements from the contralateral breast at slightly different locations. Each set consists of 3 consecutive measurements which takes around 4 to 5 seconds. The separation between each set of measurements varies from few seconds to tens of seconds because of hand-held operation. Therefore, a total 12 to 18 measurements may take about one to two minutes. A commercially available US transducer located in the middle of the hand-held probe of 9 cm diameter was used to acquire US images and optical source fibers and light guides distributed at the periphery were used to collect the diffused light from tissue [10].

6.4. Methods

Fast data acquisition of US-guided DOT system allows the collection of several datasets during one imaging session. The data contains multiple datasets from both lesion and contralateral

reference breast. A novel automated method for outlier removal and data selection is introduced to eliminate the effect of inaccurate measurements. The block diagram of the procedures is given in Fig. (1).

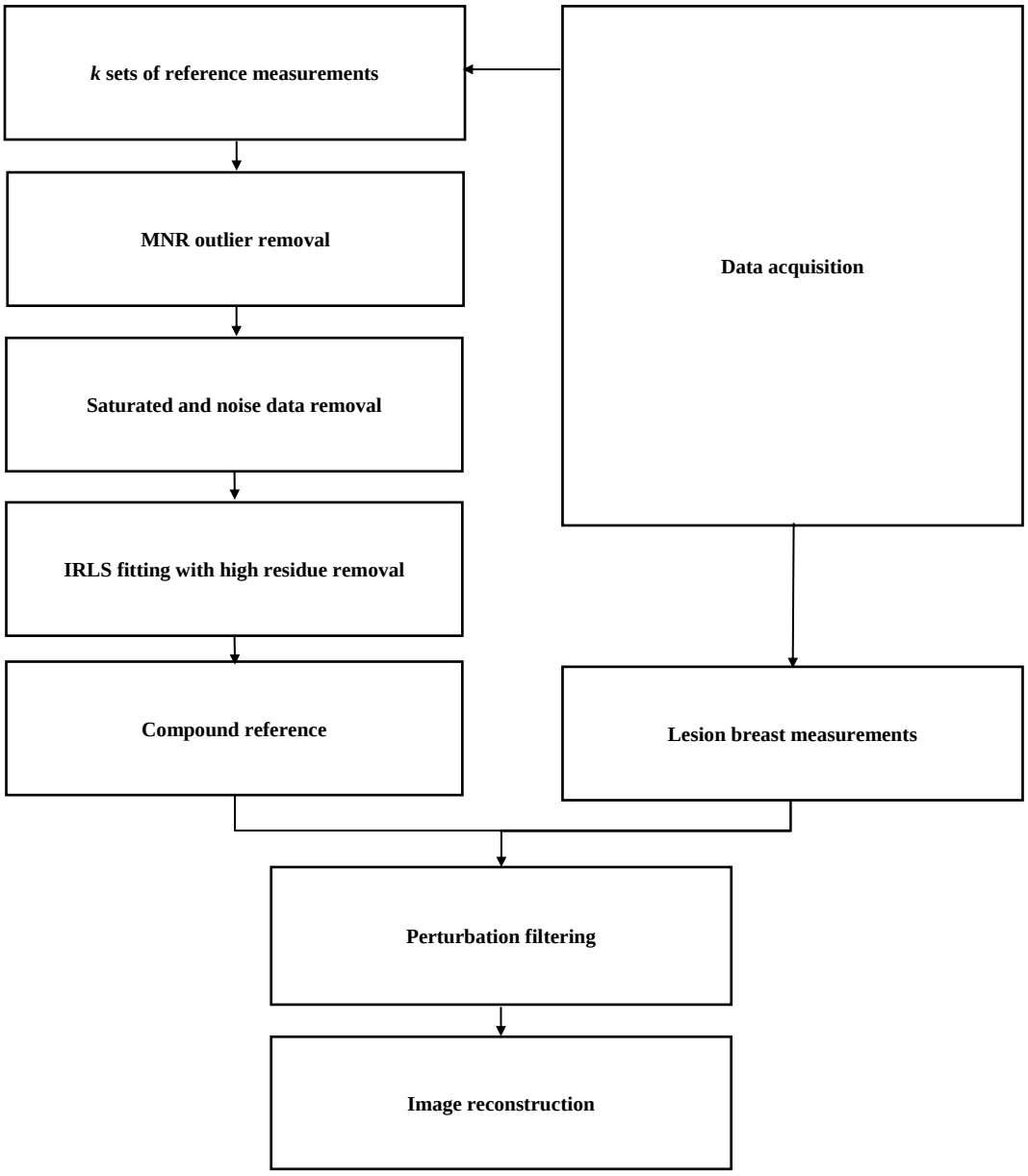

Figure 6.1 Block diagram of the automated outlier removal and data selection method. In the block diagram MNR stands for maximum normed residual and IRLS stands for iterative reweighted least square.

Multiple sets of reference measurements were used to form a single high-quality dataset. First, an outlier removal procedure is incorporated to eliminate the highly inaccurate measurements with a criterion based on the distribution of data collected at each source-detector pair. Second, a piece-linear fitting is used to reject the source-detector pair measurements obtained from the saturated PMTs. Third, an iterative fitting of residue of the remaining data is calculated to further eliminate inaccurate measurements based on the linearity of fitted results of the reference measurements of all source-detector pairs. Fourth, a least-square error method is used to form the most accurate reference dataset from the remaining measurements. Finally, a perturbation filtering based on analysis obtained from the semi-infinite analytical solution of light propagation in tissue [24] is utilized to form accurate perturbation set that is more robust to outlier and inaccurate measurements. The aforementioned steps are described in detail below.

6.4.1. Outlier Rejection in Reference Measurements

Each dataset contains measurements from s sources and d detectors with the total number of m=s×d measurements. The system used in this study provides 90 source-detector measurements per dataset. A total of k datasets of total k×s×d measurements collected at the reference site were used for selecting a best reference dataset. In general, k is in the range of 12 to 18. Since we are using a frequency domain DOT system, each dataset consists of amplitude and phase data. The maximum normed residual (MNR) is a widely used statistical test to address the problem of outlier rejection [25] that has shown outstanding performance in both linear and nonlinear data [26]. The MNR test is based on the largest absolute deviation from the sample mean in units of the sample

standard deviation. This test is applied to remove outliers for each source-detector pair of total k datasets. The outlier measurement is expunged from each source-detector pair dataset based on the following criterion. An upper critical value of the t-distribution with k−2 degrees of freedom is calculated, and a threshold is obtained based on Eq. (1).

$$G_{Threshold}(i) = \frac{k-1}{\sqrt{k}} \sqrt{\frac{t^2_{\alpha/(2k),k-2}(i)}{k-2+t^2_{\alpha/(2k),k-2}(i)}}. \quad (1)$$

In this equation GThreshold(i) is the outlier threshold for ith source-detector pair, tα/(2k), k-2(i) denotes the upper critical value of the t-distribution with k−2 degrees of freedom, and α represents the level of significance which determines the strictness of outlier removal procedure. By changing this value between 0 and 1, the total number of the outliers and the significance of these outliers removed from the database have changed. To find the optimal value of α, the outlier removal process is performed for different significance level ranging from 0.01 to 0.5 and the optimal value is set to 0.05 based on visual examination of the removed outliers. This optimal value is selected in a way that the test only removes the significant outlier data. A G value is determined as an absolute deviation of the data point from mean value of the measurements and normalized by standard deviation. The data point corresponding to maximum G value which has absolute deviation higher than the threshold is considered as an outlier and removed from the dataset. The test is iterated until no further outliers are detected beyond the threshold. This test is done for both amplitude and phase measurements separately. The details of this method can be found in [27,28]. If a data point in either amplitude or phase measurements is considered as an outlier, both amplitude and phase measurements are removed from the datasets.

6.4.2. Saturation and Noise Data Rejection

In addition to outliers in the reference measurements, detector saturation is another common problem in DOT that can happen as a result of higher light intensity detected at a shorter source detector distance. A semi-infinite analytic solution predicts that the logarithm of the detected amplitude for each source-detector pair multiplied by square distance of that specific source-detector pair, referred as logarithmic amplitude, should linearly decrease with the source-detector distance for homogeneous reference measurements. The phase measurement should increase linearly with the source-detector distance. A piece-linear fitting method is implemented for the amplitude measurements of all remaining source-detector pairs in the reference data after outlier rejection. In general, three sections of shorter source-detector distance, mid-range, and longer distance range were used. If a measured logarithmic amplitude at a shorter source-detector distance does not follow the linear profile plotted as a function of the source-detector separation in the mid and longer range, we can assume that the PMT is saturated at this detector distance. The measurements that fit the linear profile are kept for further processing. Additionally, the phase data corresponding to the saturated amplitude data are not reliable and are removed from both reference and lesion datasets.

Besides the saturated measurements which usually happen for the source-detector pairs with shorter distances, there are measurements of source-detector pairs with longer distances which are dominated by the noise of the system and are not reliable. To improve the dataset, any measurements of longer source detector pairs with amplitudes below the electronic noise of the system are considered as noisy measurements and expunged from the data. Since the corresponding phase data with amplitudes at noise level are not reliable and these data have also removed from the data.

6.4.3. Iterative Reweighted Least Square Fitting

The MNR test is based on each source detector measurements separately and it removes the outliers at each source-detector pair. At this stage, all remaining datasets after MNR and saturation data removal are inputted to an iterative reweighted least square (IRLS) method to obtain an accurate linear fit with the minimum fitting residue for both log scaled amplitude and phase measurements as functions of source and detector separation. This method has given great results in different p-norm minimization problems ranging from compressive sensing to baseline correction in industrial settings [29,30].

As shown in Eq. (2) IRLS iteratively minimizes the bi-square weighted residual in the least-square sense [29]:

$$\beta_{n+1} = \sum_{i=1}^{m} w(i)\beta_n \left| y(i) - f(i,\beta) \right|^2 . \tag{2}$$

Here i is the index of the measurement, w is the bi-square weight function, y is the measurement value, β includes slope and intercept of the line fitted to the data and f(i,β) is the fitted measurement based on the current β . This method reduces the influence of large residuals in the fitted reference parameters and improves the fitted results. After the fitting for both logarithmic amplitude and phase is completed, the distance of each amplitude and phase measurement from the corresponding value on the fitted line of same source-detector distance is calculated. All the measurements with higher absolute residue compared to the threshold in either amplitude or phase measurements are selected as non-accurate measurements and removed from the dataset. The absolute residue threshold of 0.5 has been empirically selected for both amplitude and phase based on trial and error from clinical data. Since the IRLS-based minimization is robust and less sensitive to noise bursts, it improves the robustness of the dataset selection [30].

6.4.4. Compounded Reference

Even though accurately fitted lines for both log scaled amplitude and phase are obtained from the previous steps, there may still be more than one measurement for each remaining source-detector separation. Now one amplitude and one phase measurement per source-detector pair need to be selected to form a single robust reference dataset. Here, a least square method is utilized to select the measurements with minimum distance from the center of the distribution of remaining measurements for each source-detector pair. This processed is done separately on the remaining amplitude and phase data. Therefore, a final reference dataset with high similarity to the fitted slope and intercept of outlier removed combination of all the reference datasets is achieved. This reference dataset consists of the selected amplitude and phase measurements for the remaining source-detector pairs. This robust set of reference measurements is named as the compounded reference and is less sensitive to outliers, PMT saturation and noise.

To visualize the effect of the proposed process, the amplitudes and phase profiles of one clinical case before and after preprocessing, as well as the final compound reference have been illustrated in Fig. 6.2. The preprocessing includes, outlier removal, saturation and noise rejection and iterative reweighted fitting with higher residue removal.

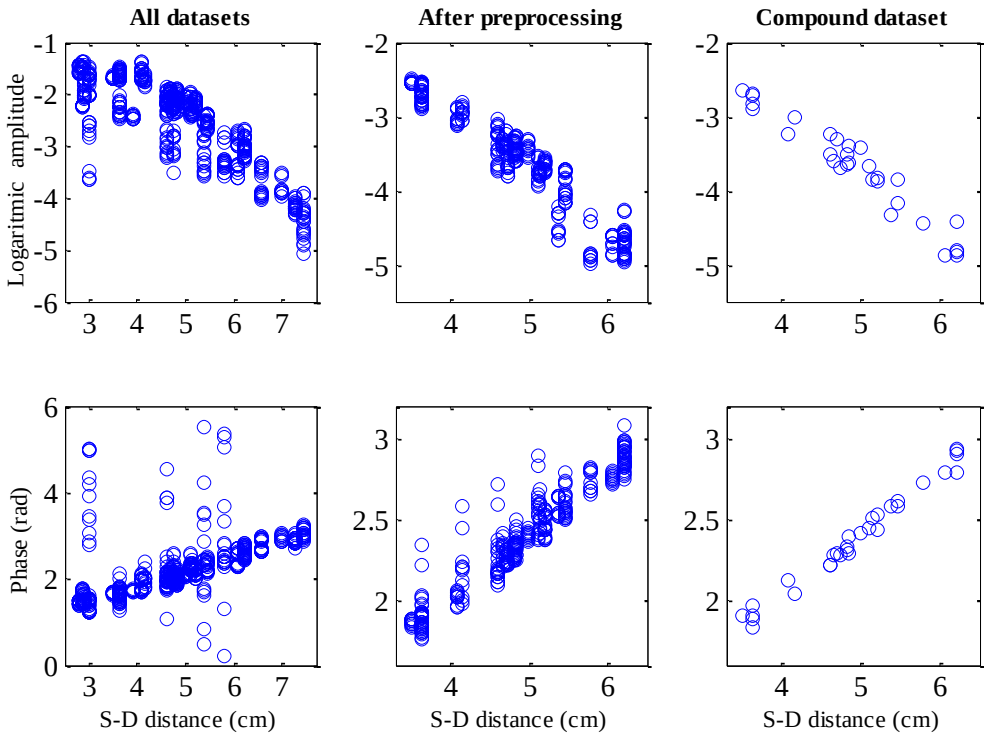

Fig. 6.2. Log scaled amplitude and phase profiles of reference datasets before (first column) and after preprocessing (second column) as well as final compound reference (third column). Saturated source-detector pairs have been marked with red rectangle in the amplitude part of the first column.

6.4.5. Perturbation filtering

The procedures described above provide a robust set of reference measurement. For reconstruction of lesion absorption map at each wavelength, perturbation is calculated by subtracting the compound reference from the lesion data as shown in Eq. (3), in which Al and Ar are amplitude and φl and φr are phase of each source-detector pair obtained at the lesion and compound reference, respectively.

$$U_{sc} = \frac{A_l(i).\exp\left(\varphi_l(i)\right) - A_r(i).\exp\left(\varphi_r(i)\right)}{A_r(i).\exp\left(\varphi_r(i)\right)}$$
$$= \left(\frac{A_l(i)}{A_r(i)}\cos\left(\varphi_l(i) - \varphi_r(i)\right) - 1\right) + j\left(\frac{A_l(i)}{A_r(i)}\sin\left(\varphi_l(i) - \varphi_r(i)\right)\right) \quad (3)$$

The outliers may present in the perturbation data due to 1) measurements errors caused by movements of patient or operator's hand as well as bad coupling between the light guides and the breast; and 2) heterogeneity of the background tissue and the lesion. Lesion measurements are expected to be more heterogeneous than the reference measurements because the heterogeneity is partially caused by the lesion and partially by the background tissue heterogeneity. Therefore, outlier removal procedures applied to reference measurements cannot be implemented to the lesion measurements. Instead, a filtering method is applied to the perturbation based on the constraints imposed on the phase difference between the lesion data and the reference data given in Eq. (3). These conditions are determined based on the predictions obtained from the semi-infinite analytical solution derived from diffusion approximation [24, 31]. Simulations were performed using different background optical properties for both reference and lesion breasts as well as different optical properties for lesions of different sizes located at different depths [32]. The simulations used the same probe geometry and the same number of the sources and detectors as the experiments. Table 6.1 shows the range of the parameters used for simulations. The results show that the maximum phase difference between lesion and reference measurements of all source detector pairs for most scenarios listed in table 1 are in the range of few degrees. For a 4 cm larger lesion of optical contrast of 10 times higher than the background, the maximum phase difference is only 22 degrees. This implies that the maximum phase difference of none of the source detector pairs can exceed 90 degrees even in extreme cases. This indicates that the cosine term in Eq. (3) should always be positive. Therefore, the real part of the perturbation cannot be less than -1 assuming that the amplitude measured from lesion A_l is smaller than that of the amplitude measured at reference A_r due to a higher absorption of the lesion in general. Furthermore, the mean and the standard deviation of the imaginary part of the perturbation are calculated. If the imaginary

part of a data point is farther than three standard deviations from the mean, it is considered an outlier. Any data points in the perturbation that do not meet these two criteria are rejected. This step removes outliers in the perturbation likely caused by measurement errors rather than heterogeneity of the lesion data.

Table 6.1. Range of parameters used for analytical model and obtained maximum phase delay.

Background μ_a	Background μ'_s	Lesion $\Delta\mu_a$	Lesion depth	Lesion radius
0.02 -0.08 (cm^{-1})	5 – 10 (cm^{-1})	0.05 – 0.2 (cm^{-1})	1.5- 3.5 (cm)	0.5-2 (cm)

This normalized perturbation is used for reconstructing the absorption map at each wavelength. The total hemoglobin map was calculated from the four wavelength absorption data. The dual-zone mesh scheme is used for inversion [32]. Briefly, the imaging volume is segmented into two regions consisting of the lesion and the background regions. These two regions are identified by the co-registered ultrasound images. This method reduces the total number of voxels with unknown optical properties by using smaller mesh size for lesion region and a larger coarse mesh size for background. The conjugate gradient method is utilized for iterative optimization of the inverse problem. Patient results are calculated from the selected data based on this automated outlier removal and data selection procedures.

6.5. Results

To quantify the effectiveness of the proposed method, the results obtained from manually selected and processed dataset were compared with the results obtained from the automated data processing method. The malignant versus benign classification was based on biopsy result which is the “gold” standard in current clinical practice. The manual selection was performed by a trained user to obtain the best outlier removal result. The absorption maps obtained at four optical wavelengths of benign and malignant examples are shown in Figure 6.3 and 6.4, respectively. The effect of outlier and bad measurements on the reconstructed image with no preprocessing is clearly seen from the 740 nm image of first row in Fig. 6.4. Both manual and automated methods were able to improve wavelength consistency by removing outlier measurements from the dataset. The automated method provides similar reconstruction results as the manually processed ones with only minor differences.

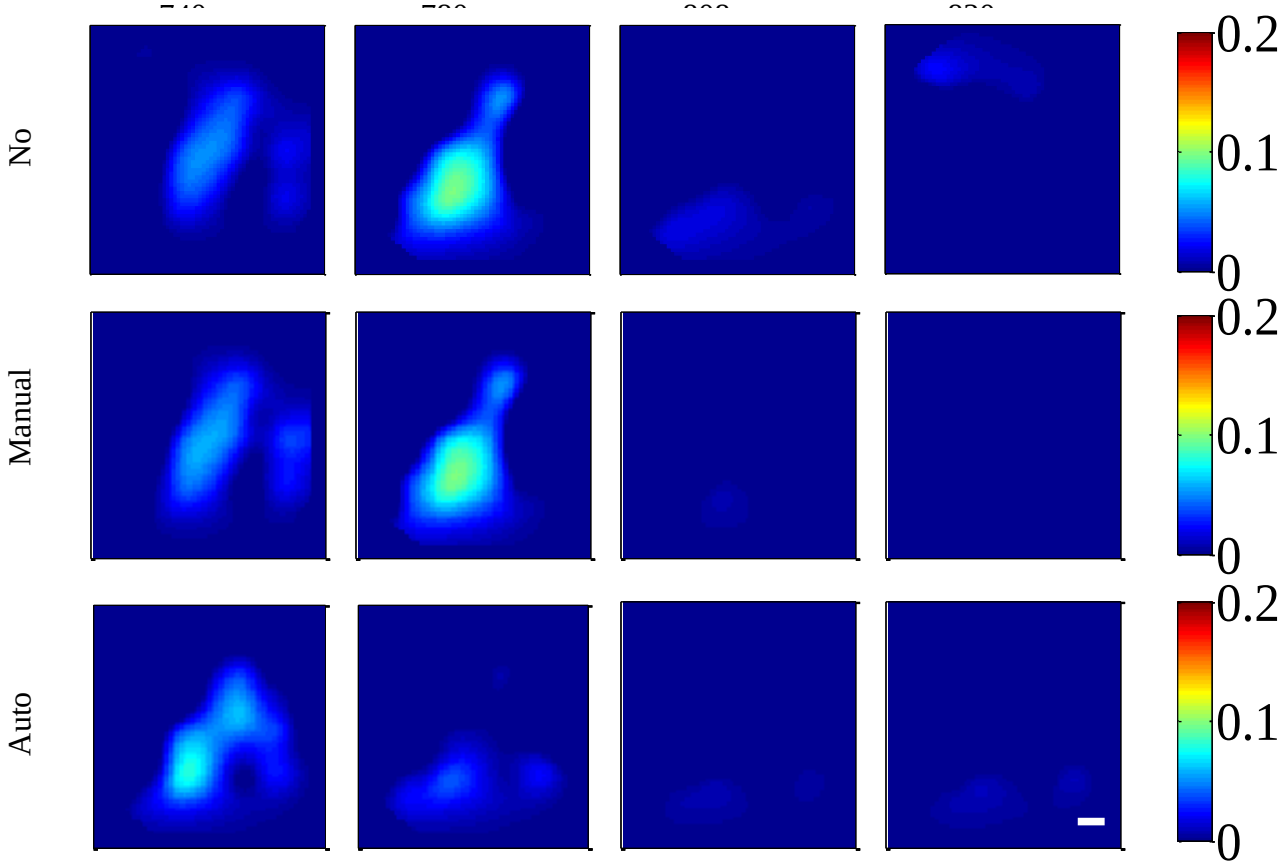

Fig. 6.3. Reconstructed absorption maps of a benign breast lesion obtained at 740, 780, 808 and 830 nm with no preprocessing (1st row), with manual data selection (2nd row) and automated data selection (3rd row). Each slide is 9 cm by 9 cm reconstructed at the center depth of the lesion. Images from other depths were not shown. Vertical bars are absorption in cm^{-1} unit.

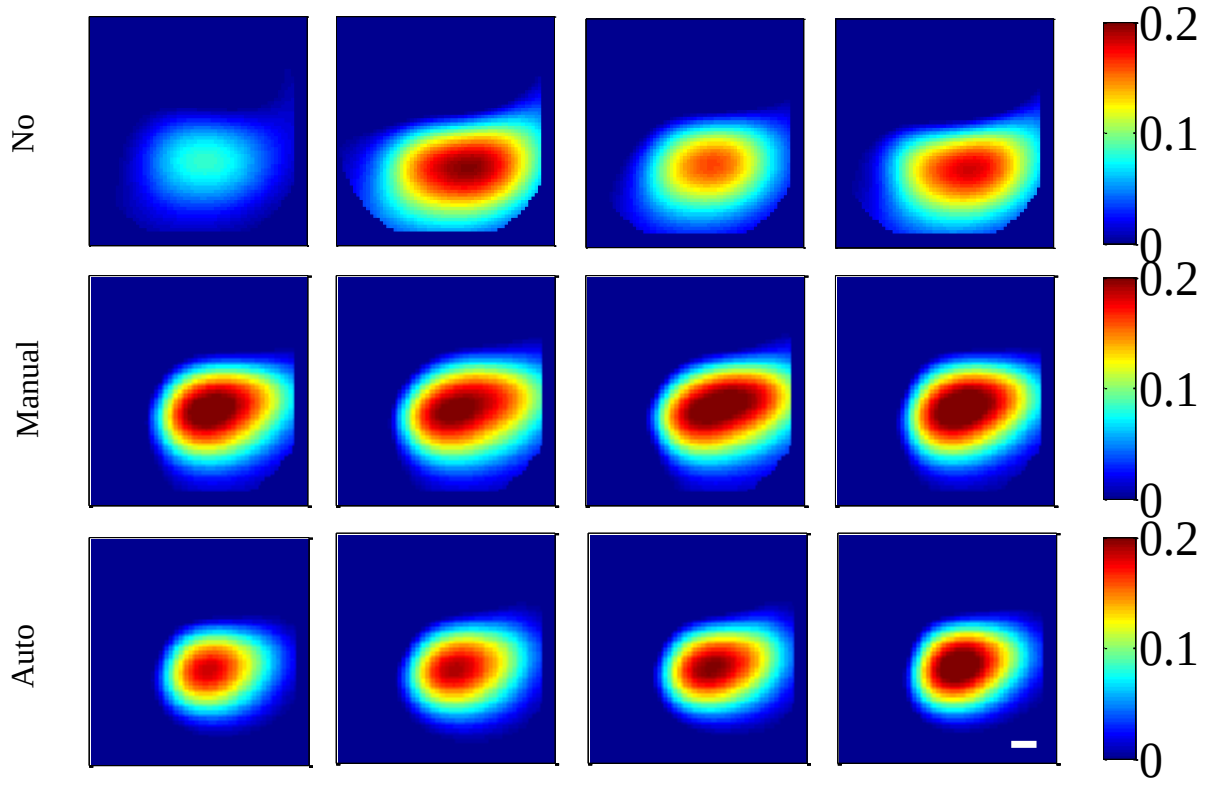

Fig. 6.4. Reconstructed absorption maps of a malignant breast lesion at 740, 780, 808 and 830 nm with no preprocessing (1st row), with manual data selection (2nd row) and automated data selection (3rd row). Each slide is 9 cm by 9 cm reconstructed at the center depth of the lesion. Images from other depths were not shown. Vertical bars are absorption in cm^{-1} unit.

The corresponding ultrasound images and the calculated total hemoglobin maps obtained by both manual and automatic methods along with calculated total hemoglobin maps with no outlier removal and data selection are presented in Fig. (5) for the benign and malignant cases. The lower reconstructed absorption at 740 nm of the malignant case with no data selection caused wavelength inconsistency and reduced the calculated total hemoglobin concentration. It can be seen that both manual and automated methods have improved wavelength consistency and better malignant to benign separation by reducing the effect of saturated, noisy and outlier data. The HbT concentrations are also comparable between manual and automated methods.

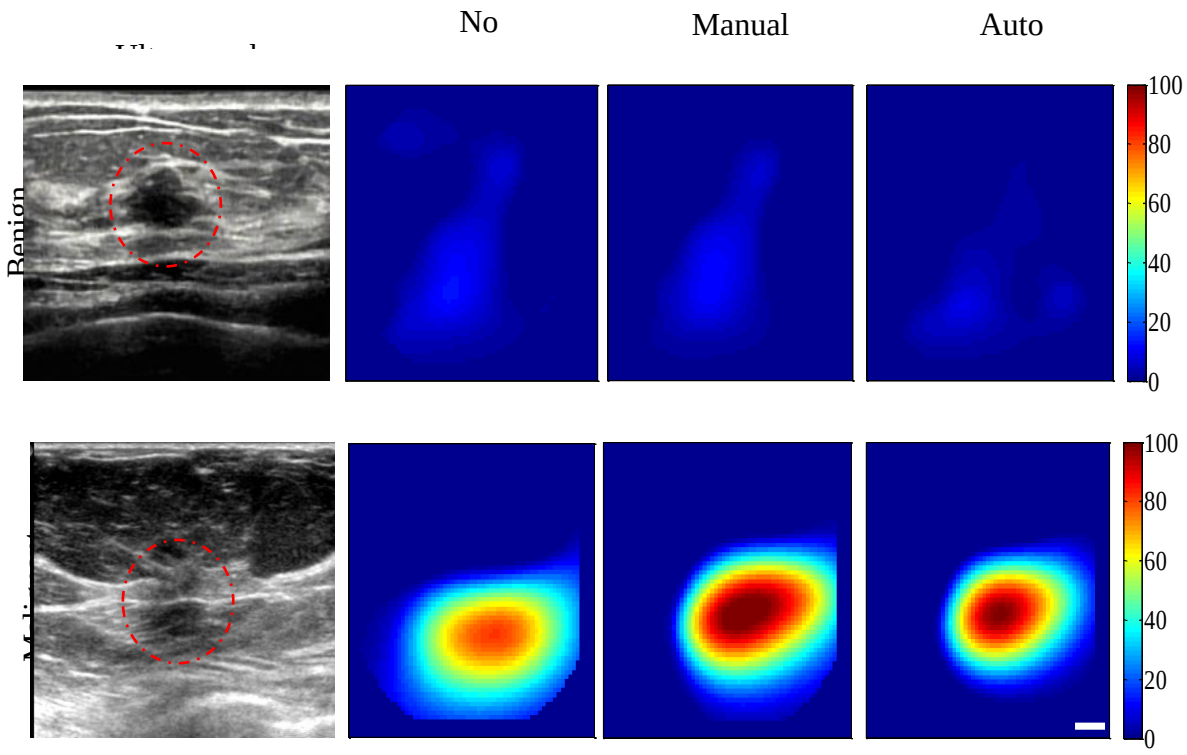

Fig. 6.5. Ultrasound image (1st column) and total hemoglobin map calculated with no data selection (2nd column), with manual data selection (3rd column) and automatic data selection (4th column) of the benign (top row) and the malignant breast lesion (bottom row) reconstructed with automated data selection method. Each slide is 9 cm by 9 cm and vertical bars are hemoglobin concentrations in uM unit.

To compare manual and automated methods statistically, both have applied to the datasets collected from 20 patients (10 malignant and 10 benign). The maximum reconstructed absorption coefficient with each method was calculated. The mean value and the standard deviation of the maximum reconstructed absorption coefficient for malignant and benign groups along with the ratio of the mean values are presented in Table 6.2. The proposed automated data selection and outlier removal method shows slightly higher malignant to benign ratio of all wavelengths due to improved data selection.

Table 6.2. Comparison of maximum reconstructed absorption coefficients of malignant and benign groups using manual and automated data selection method

Maximum reconstructed absorption with manual data selection (cm^{-1})			
	Malignant group	Benign group	Ratio
740 nm	0.22 (0.05)	0.11 (0.03)	2.02
780 nm	0.24 (0.05)	0.13 (0.04)	1.88
808 nm	0.24 (0.05)	0.14 (0.03)	1.74
830 nm	0.24 (0.04)	0.12 (0.04)	1.96
Maximum reconstructed absorption with automatic data selection (cm^{-1})			
	Malignant group	Benign group	Ratio
740 nm	0.209 (0.06)	0.10 (0.03)	2.06
780 nm	0.22 (0.06)	0.09 (0.03)	2.53
808 nm	0.23 (0.05)	0.09 (0.03)	2.57
830 nm	0.24 (0.06)	0.10 (0.03)	2.47

The total hemoglobin concentrations for all 20 patients are calculated using both manual and automated data selection methods. Table 3 shows the comparison of the mean and the standard deviation of the maximum total hemoglobin concentration reconstructed by both methods as well as the ratio of the average HbT concentration between malignant and benign cases. Fig. (6) shows the box plots of the reconstructed HbT concentrations of malignant and benign cases. The results indicate a slight increase of the malignant to benign ratio of HbT from 2.01 to 2.55 by using the automated data selection method.

Table 6.3. Comparison of maximum reconstructed absorption coefficients of malignant and benign groups using manual and automated data selection method

Maximum reconstructed total hemoglobin concentration (μM)			
	Malignant group	Benign group	Ratio
Manual Data selection	115.38 (20.90)	57.28 (12.38)	2.01
Automatic Data selection	112.31 (25.06)	43.97 (13.31)	2.55

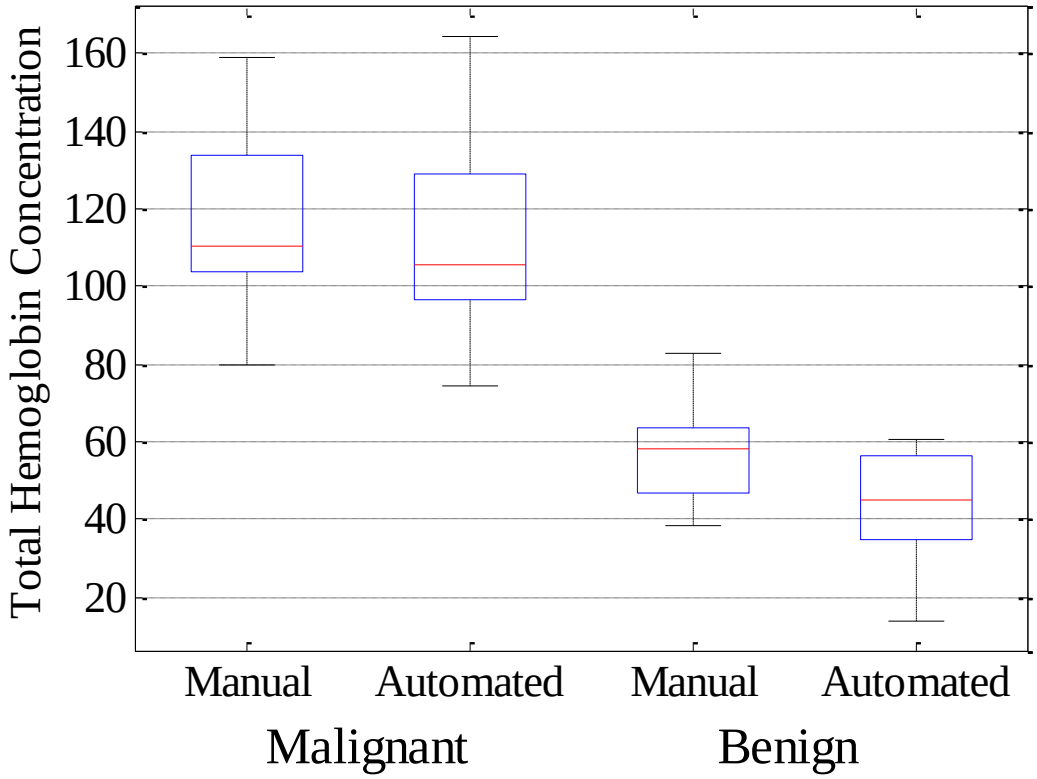

Fig. 6.6. Comparison of maximum total hemoglobin concentration reconstructed with both manual and automated data selection methods for 10 malignant and 10 benign cases. Vertical axis is the total hemoglobin concentration in μmol/Liter.

6.6. Discussion and Summary

In this chapter an automated pre-processing method for imaging-guided DOT is introduced. This method combines multiple datasets obtained from a normal breast which is used as a reference and implements outlier and saturation data removal, and linear fitting to form a robust compound set of reference measurements. Because the reference site does not have lesions inside, the location of the probe relative to the imaged area is not as critical as lesion site. Therefore, multiple reference datasets obtained from slightly different positions can be combined and used as the inputs of the automated compound reference selection method. On the other hand, in the affected breast, due to the presence of the lesion, the described outlier removal and compound data selection method is not appropriate. Instead, a perturbation filtering method, based on simulations, is introduced to eliminate the outliers and inaccurate data due to measurement errors.

The clinical results using the automated compound reference selection method were compared with the manually processed results. An experienced user performed the manual outlier removal and data selection after the imaging session and the best manually selected datasets have been used for the image reconstruction to compare with the automated method. Although the results calculated by our experienced user shows high significance for malignant and benign classification, the proposed automated compound outlier removal and data selection method outperforms the experienced user without the need for user interactions. On average, an expert need about 15 to 20 minutes to perform the outlier removal and data selection manually, while the automated method takes about 20 seconds using a typical dual core computer of 2.3 to 2.8 GHz speed. T-test is performed on the total hemoglobin results obtained from each method and the test shows p-values of less than 0.001 in both cases which indicates strong statistical significance

between malignant and benign groups. Although both methods provide strong statistical significance between malignant and benign groups, but the ratio for malignant to benign has been improved with the automated method. In particular, the ratio of malignant to benign lesions has been increased from 2.01 using manual data selection to 2.55 using automated data selection method with about 27% improvement.

Although our automated compound data selection method is introduced in the US-guided DOT approach, it can be readily applied to other imaging guided DOT approaches. In general, diffuse optical tomography relies on reference measurements either reference data from a normal area of the same breast with lesions or a contralateral normal breast. The reference selected from a normal area of the same patient is considered the best healthy control because each patient has different background tissue optical properties depending on age, tissue composition, and menopausal status as reported by several research groups in the past. Some groups used average background tissue by excluding the tumor area in mammography guided or MRI guided diffuse optical tomography [12]. Some groups used a localized area of healthy tissue in the lesion breast [14] and some including our group used the mirror region in the contralateral breast [8, 10, 15]. Depending on the heterogeneity of the healthy tissue, the choice of reference area and the data quality of the area impacts the level of tissue contrast. The proposed automated robust reference selection method removes data outliers, rejects saturated and noise data, and performs a linear fitting if a linear model is used such as approaches using hand-held probes where semi-infinite boundary condition is applicable. Thus, the proposed automated reference selection method is applicable to these approaches to improve the reference data quality, reduce data processing time. This is an important step toward clinical translation and commercialization of diffuse optical tomography techniques.

In conclusion, an automated compound data selection method is introduced. This method forms a compound set of measurements from multiple datasets and outperformed the manual method in two different aspects. First, this method is able to eliminate the effect of inaccurate and noisy measurements by combining multiple datasets and improves the differentiation between malignant and benign cases. The results show improved differentiation between malignant and benign lesions compared to the manual data selection. Second, this method makes outlier removal, data selection, and processing automated by removing the need for experienced users to perform the manual data selection and outlier removal. Utilizing the automated and compound data selection method, the data processing speed is significantly improved, and the user dependency of data processing is reduced. Future work includes automatic measurements of lesion boundaries in US images and input the measurements into image reconstruction.

The results presented in this chapter was published in journal of biomedical optics express and proceeding of OSA conference [32,33].

References

[1] Zheng, B., A. B. Hollingsworth, M. Y. Tan, R. G. Stough, and H. Liu. "Abstract P4-02-06: Improving efficacy of applying breast MRI to detect mammography-occult breast cancer." (2016): P4-02.

[2] Berg, Wendie A., Andriy I. Bandos, Ellen B. Mendelson, Daniel Lehrer, Roberta A. Jong, and Etta D. Pisano. "Ultrasound as the primary screening test for breast cancer: analysis from ACRIN 6666." *JNCI: Journal of the National Cancer Institute* 108, no. 4 (2016).

[3] Boas, David A., Dana H. Brooks, Eric L. Miller, Charles A. DiMarzio, Misha Kilmer, Richard J. Gaudette, and Quan Zhang. "Imaging the body with diffuse optical tomography." *IEEE signal processing magazine* 18, no. 6 (2001): 57-75.

[4] Wu, Xue, Adam T. Eggebrecht, Silvina L. Ferradal, Joseph P. Culver, and Hamid Dehghani. "Fast and efficient image reconstruction for high density diffuse optical imaging of the human brain." *Biomedical optics express* 6, no. 11 (2015): 4567.

[5] Durduran, Turgut, Regine Choe, W. B. Baker, and Arjun G. Yodh. "Diffuse optics for tissue monitoring and tomography." *Reports on Progress in Physics* 73, no. 7 (2010): 076701.

[6] Larusson, Fridrik, Pamela G. Anderson, Elizabeth Rosenberg, Misha E. Kilmer, Angelo Sassaroli, Sergio Fantini, and Eric L. Miller. "Parametric estimation of 3D tubular structures for diffuse optical tomography." *Biomedical optics express* 4, no. 2 (2013): 271-286.

[7] Chance, Britton, Shoko Nioka, Jun Zhang, Emily F. Conant, Emily Hwang, Susanne Briest, Susan G. Orel, Mitchell D. Schnall, and Brian J. Czerniecki. "Breast cancer detection based on incremental biochemical and physiological properties of breast cancers: a six-year, two-site Study1." *Academic radiology* 12, no. 8 (2005): 925-933.

[8] Quarto, Giovanna, Lorenzo Spinelli, Antonio Pifferi, Alessandro Torricelli, Rinaldo Cubeddu, Francesca Abbate, Nicola Balestreri, Simona Menna, Enrico Cassano, and Paola Taroni. "Estimate of tissue composition in malignant and benign breast lesions by time-domain optical mammography." *Biomedical optics express* 5, no. 10 (2014): 3684-3698.

[9] Zhu, Quing, Andrew Ricci Jr, Poornima Hegde, Mark Kane, Edward Cronin, Alex Merkulov, Yan Xu, Behnoosh Tavakoli, and Susan Tannenbaum. "Assessment of functional differences in malignant and benign breast lesions and improvement of diagnostic accuracy by using US-guided diffuse optical tomography in conjunction with conventional US." *Radiology* 280, no. 2 (2016): 387-397.

[10] Ntziachristos, Vasilis, A. G. Yodh, Mitchell D. Schnall, and Britton Chance. "MRI-guided diffuse optical spectroscopy of malignant and benign breast lesions." *Neoplasia* 4, no. 4 (2002): 347-354.

[11] Fang, Qianqian, Juliette Selb, Stefan A. Carp, Gregory Boverman, Eric L. Miller, Dana H. Brooks, Richard H. Moore, Daniel B. Kopans, and David A. Boas. "Combined optical and X-ray tomosynthesis breast imaging." *Radiology* 258, no. 1 (2011): 89-97.

[12] Mastanduno, Michael A., Junqing Xu, Fadi El-Ghussein, Shudong Jiang, Hong Yin, Yan Zhao, Kelly E. Michaelsen et al. "Sensitivity of MRI-guided near-infrared spectroscopy clinical breast exam data and its impact on diagnostic performance." *Biomedical optics express* 5, no. 9 (2014): 3103-3115.

[13] Cerussi, Albert, Natasha Shah, David Hsiang, Amanda Durkin, John Butler, and Bruce J. Tromberg. "In vivo absorption, scattering, and physiologic properties of 58 malignant breast

tumors determined by broadband diffuse optical spectroscopy." *Journal of biomedical optics* 11, no. 4 (2006): 044005-044005.

[14] Zhu, Quing, Poornima U. Hegde, Andrew Ricci Jr, Mark Kane, Edward B. Cronin, Yasaman Ardeshirpour, Chen Xu et al. "Early-stage invasive breast cancers: potential role of optical tomography with US localization in assisting diagnosis." *Radiology* 256, no. 2 (2010): 367-378.

[15] Mastanduno, Michael A., Shudong Jiang, Roberta DiFlorio-Alexander, Brian W. Pogue, and Keith D. Paulsen. "Automatic and robust calibration of optical detector arrays for biomedical diffuse optical spectroscopy." *Biomedical optics express* 3, no. 10 (2012): 2339-2352.

[16] Dehghani, Hamid, Matthew E. Eames, Phaneendra K. Yalavarthy, Scott C. Davis, Subhadra Srinivasan, Colin M. Carpenter, Brian W. Pogue, and Keith D. Paulsen. "Near infrared optical tomography using NIRFAST: Algorithm for numerical model and image reconstruction." *International Journal for Numerical Methods in Biomedical Engineering* 25, no. 6 (2009): 711-732.

[17] Srinivasan, Subhadra, Brian W. Pogue, Hamid Dehghani, Frederic Leblond, and Xavier Intes. "Data subset algorithm for computationally efficient reconstruction of 3-D spectral imaging in diffuse optical tomography." *Optics express* 14, no. 12 (2006): 5394-5410.

[18] Kavuri, Venkaiah C., Zi-Jing Lin, Fenghua Tian, and Hanli Liu. "Sparsity enhanced spatial resolution and depth localization in diffuse optical tomography." *Biomedical optics express* 3, no. 5 (2012): 943-957.

[19] Kepshire, Dax L., Hamid Dehghani, Frederic Leblond, and Brian W. Pogue. "Automatic exposure control and estimation of effective system noise in diffuse fluorescence tomography." *Optics express* 17, no. 25 (2009): 23272-23283.

[20] Xu, Chen, Hamed Vavadi, Alex Merkulov, Hai Li, Mohsen Erfanzadeh, Atahar Mostafa, Yanping Gong, Hassan Salehi, Susan Tannenbaum, and Quing Zhu. "Ultrasound-guided diffuse optical tomography for predicting and monitoring neoadjuvant chemotherapy of breast cancers: recent progress." *Ultrasonic imaging* 38, no. 1 (2016): 5-18.

[21] Arridge, Simon R., and John C. Schotland. "Optical tomography: forward and inverse problems." *Inverse Problems* 25, no. 12 (2009): 123010.

[22] Dehghani, Hamid, Subhadra Srinivasan, Brian W. Pogue, and Adam Gibson. "Numerical modelling and image reconstruction in diffuse optical tomography." *Philosophical Transactions of the Royal Society of London A: Mathematical, Physical and Engineering Sciences* 367, no. 1900 (2009): 3073-3093.

[23] Danen, R. M., Yong Wang, X. D. Li, W. S. Thayer, and A. G. Yodh. "Regional imager for low-resolution functional imaging of the brain with diffusing near-infrared light." *Photochemistry and Photobiology* 67, no. 1 (1998): 33-40.

[24] Stefansky, Wilhelmine. "Rejecting outliers by maximum normed residual." *The Annals of Mathematical Statistics* 42, no. 1 (1971): 35-45.

[25] Sutradhar, Brajendra C., David PT Chu, and Wasimul Bari. "Estimation effects on powers of two simple test statistics in identifying an outlier in linear models." *Journal of Statistical Computation and Simulation* 77, no. 4 (2007): 305-328.

[26] Grubbs, Frank E. "Sample criteria for testing outlying observations." *The Annals of Mathematical Statistics* (1950): 27-58.

[27] Grubbs, Frank E. "Procedures for detecting outlying observations in samples." *Technometrics* 11, no. 1 (1969): 1-21.

[28] Chartrand, Rick, and Wotao Yin. "Iteratively reweighted algorithms for compressive sensing." In *Acoustics, speech and signal processing, 2008. ICASSP 2008. IEEE international conference on*, pp. 3869-3872. IEEE, 2008.

[29] Zhang, Zhi-Min, Shan Chen, and Yi-Zeng Liang. "Baseline correction using adaptive iteratively reweighted penalized least squares." *Analyst* 135, no. 5 (2010): 1138-1146.

[30] Fishkin, Joshua B., and Enrico Gratton. "Propagation of photon-density waves in strongly scattering media containing an absorbing semi-infinite plane bounded by a straight edge." *JOSA A* 10, no. 1 (1993): 127-140.

[31] Huang, Minming, and Quing Zhu. "Dual-mesh optical tomography reconstruction method with a depth correction that uses a prioriultrasound information." *Applied optics* 43, no. 8 (2004): 1654-1662.

[32] Vavadi, Hamed, and Quing Zhu. "Automated data selection method to improve robustness of diffuse optical tomography for breast cancer imaging." Biomedical optics express 7, no. 10 (2016): 4007-4020.

[33] Vavadi, Hamed, Chen Xu, Atahar Mostafa, and Quing Zhu. "Automated Data Selection Method for Diffuse Optical Tomography to Improve the Robustness of Breast Cancer Detection." In Clinical and Translational Biophotonics, pp. JM3A-2. Optical Society of America, 2016.

7. Summary and Future Works

7.1. Summary

In this dissertation we have discussed the use of ultrasound-guided diffuse optical tomography method to detect breast cancer and monitor patients undergoing neoadjuvant chemotherapy.

In the first chapter, we have briefly reviewed the history of medical imaging. The field first started after discovery of X-rays and its application in imaging the tissue and bones. Several methods and modalities for medical imaging has been developed during last century and they have found wide

application in disease screening, diagnosis and treatment monitoring. We discussed that, while each of the currently used conventional imaging, methods have their strength and drawbacks, the need to develop a new imaging technique which could address current needs in medical community and improve human health monitoring is being felt more than ever.

As described in chapter 2, One of the promising ideas for next gen medical imaging devices are optical imaging. While several methods of optical imaging with different wavelength sub bands are currently under investigation, we discussed the use of near-Infrared light in optical imaging. The infrared light has multiple interesting characteristics such as good depth of penetration inside the tissue and sensitivity to hemoglobin. In chapter 2, we specifically reviewed near-infrared diffuse optical tomography method, followed by description of ultrasound-guided DOT to improve the lesion localization and reconstruction accuracy. we have also discussed the use of diffuse optical tomography in clinical setting for breast cancer detection.

In the third chapter, we discussed the development of the third generation of the ultrasound-guided diffuse optical tomography system and presented the results of clinical studies which have been done with that system. we started by reviewing the older two generation of diffuse optical tomography and then continued by the details of improvements in the third generation of the ultrasound-guided DOT system. we discussed the new compact design, increase number of detection channels, improved hand-held probe and improvements in the data acquisition and design of the FPGA based data acquisition to reduce the system bulkiness and improve data acquisition speed and robustness. Following the system development, we discussed the clinical results obtained from one prototype of that system. The total hemoglobin monitoring for a breast cancer patient undergoing neoadjuvant chemotherapy has been presented in that chapter. The

results show the ability of the third generation of the ultrasound guided DOT system to monitor patients undergoing neoadjuvant chemotherapy.

Chapter 4 was devoted to the development of the fourth generation of our ultrasound guided diffuse optical tomography. The improvements in the system in terms of hardware and software were discussed. Intensive phantom experiments have been designed and performed to evaluate the performance of the fourth generation of the ultrasound guided DOT. The results show strong ability of the system in reconstructing optical properties and total hemoglobin concentration inside the tissue. Besides the system development an algorithm for calibration of the diffuse optical tomography at different depth and sizes have been developed. The results show strong improvement in the system sensitivity specially for the deeper targets.

Besides system robustness and stability, one of the main challenges in the clinical studies of the using DOT for breast imaging is the effect of the heterogeneity in the reference measurement. In chapter 5 we discussed the effect of reference heterogeneity on the reconstructed absorption map. We introduced a smoothing method to reduce the effect of reference heterogeneity and measurement inaccuracy in the reconstructed absorption map. The results show strong improvement in the value and shape of reconstructed absorption map by use of this method.

In chapter 6, we introduced an automated algorithm for removing the need for expert user to perform data selection and outlier removal. The discussed algorithm was using multiple references and a perturbation filtering to eliminate the outliers in the measurements, make the process of data preprocessing automated and form a robust reference measurement to improve the accuracy of US-guided DOT. The results of a clinical data show strong improvements in the differentiation of the malignant and benign lesion.

The results of the developed systems and algorithms in the above in this dissertation was published in multiple journal and conference proceedings as listed at the end of this chapter [1-15].

7.2. Future Works

By describing all the discussed topics in the previous 6 chapter we covered pretty much the steps I took to move the ultrasound guided diffuse optical tomography one step closer to clinical use.

Although several improvements have been applied to the system development part and improve the robustness of the DOT system, there are still several works remaining that one can continue upon to increase the performance of the system. In terms of system development one of the first steps can be taken is to increase number source wavelengths from four to 6 and incorporate wavelengths in the range of 800-900 nm to probe additional chromophores inside the tissue, including water and lipid.

In terms of software improvements, automated detection of the ultrasound boundaries is an important step to make this process more robust and less user dependent. The process of automated data selection can be extended to the different lesion measurements as well to improve the accuracy of the system.

One of the main fields that one can improve is the use of ultrasound information in differentiating malignant from benign lesions as well as monitoring patients undergoing neoadjuvant chemotherapy. As we are currently only using the depth and size of the lesion provided by the ultrasound images, looking into ultrasound signals would give us much more data.

References

[1] Hamed Vavadi, Atahar Mostafa, jinglong Li, Feifei Zhu, Shihab Uddin, Chen Xu, and Quing Zhu, "Development and miniaturization of a robust Ultrasound guided diffuse optical tomography system for breast imaging", Journal of Biomedical Optics (submit).

[2] Vavadi, Hamed, and Quing Zhu. "Automated data selection method to improve robustness of diffuse optical tomography for breast cancer imaging." Biomedical optics express 7, no. 10 (2016): 4007-4020.

[3] Xu, Chen, Hamed Vavadi, Alex Merkulov, Hai Li, Mohsen Erfanzadeh, Atahar Mostafa, Yanping Gong, Hassan Salehi, Susan Tannenbaum, and Quing Zhu. "Ultrasound-guided diffuse optical tomography for predicting and monitoring neoadjuvant chemotherapy of breast cancers: recent progress." *Ultrasonic imaging* 38, no. 1 (2016): 5-18.

[4] Quing Zhu, Susan Tannenbaum, Scott H. Kurtzman, Patricia DeFusco, Andrew Ricci, Hamed Vavadi, Feifei Zhou, Chen Xu, 5 Alex Merkulov, Poornima Hegde, Mark Kane, Liqun Wang, Kert Sabbath, "An Optimal Time Window for Assessing Breast Cancer Response to Predicting Neoadjuvant Chemotherapy using Biomarkers and Pre-treatment and Early Changes of Hemoglobin Content Measured by US-guided Diffuse Optical*" Journal of clinical cancer research (Under review)*

[5] Murad Althobaiti, Hamed Vavadi, Quing Zhu, "An automated preprocessing method based on multiple wavelength measurements for image reconstruction of Diffuse Optical Tomography", *Under revision Journal of Biomedical Optics (2017).*

[6] Atahar Mostafa, Hamed Vavadi, K M Shihab Uddin, Quing Zhu, "Diffuse Optical Tomography using Semi-Automated Co-Registered Ultrasound Measurements" *Journal of Biomedical Optics* (October 2017).

[7] Althobaiti, Murad, Hamed Vavadi, and Quing Zhu. "Diffuse optical tomography reconstruction method using ultrasound images as prior for regularization matrix." *Journal of Biomedical Optics* 22, no. 2 (2017): 026002-026002.

[8] Hassan Salehi, Hai Lli, Alex Merkulov, Patrik Kumavor, Hamed Vavadi, Melinda Sanders, Molly Brewer, and Quing Zhu. "Co-registered Photoacoustic and Ultrasound Imaging and Classification of Ovarian Cancer: Ex Vivo and in Vivo Studies." *Journal of Biomedical Optics*, (2016).

[9] Vavadi, Hamed, Atahar Mostafa, Jinglong Li, Feifei Zhou, Shihab Uddin, Chen Xu, and Quing Zhu. "Preliminary results of miniaturized and robust ultrasound guided diffuse optical tomography system for breast cancer detection." In *Optical Tomography and Spectroscopy of Tissue XII*, vol. 10059, p. 100590F. International Society for Optics and Photonics, 2017.

[10] Vavadi, Hamed, Chen Xu, Atahar Mostafa, and Quing Zhu. "Automated Data Selection Method for Diffuse Optical Tomography to Improve the Robustness of Breast Cancer Detection." In *Clinical and Translational Biophotonics*, pp. JM3A-2. Optical Society of America, 2016.

[11] Vavadi, Hamed, Chen Xu, and Quing Zhu. "The effect and correction of reference heterogeneity in diffuse optical tomography." In *SPIE BiOS*, pp. 93192D-93192D. International Society for Optics and Photonics, 2015.

[12] Mostafa, Atahar, Hamed Vavadi, and Quing Zhu. "Extraction of tumor features from ultrasound images for diffused optical tomography reconstruction." In *Optical Tomography and Spectroscopy*, pp. JTu3A-14. Optical Society of America, 2016.

[13] Murad Althobaiti, Hamed Vavadi, and Quing Zhu, "Assessment of using ultrasound images as prior for diffuse optical tomography regularization matrix", In *Optical Tomography and Spectroscopy of Tissue*, SPIE photonic west pp. 10059-72 International Society for Optics and Photonics, 2017.

[14] Xu, Chen, Hai Li, Guangqian Yuan, Hamed Vavadi, and Quing Zhu. "Development of a robust and fast calibration procedure for diffuse optical tomography." In *SPIE BiOS*, pp. 93192E-93192E. International Society for Optics and Photonics, 2015.

[15] Xu, Chen, Hamed Vavadi, Jigi Chen, Mohsen Erfanzadeh, Quangqian Yuan, Yanping Gong, Hassan Salehi, Hai Li, and Quing Zhu. "Toward miniature diffuse optical tomography system for assessing neoadjuvant chemotherapy." In *Biomedical Optics*, pp. BM3A-57. Optical Society of America, 2014.